The Approach to Classical Chaos in an Anharmonic Quantum Oscillator

by

James P. Zibin

B.Sc., University of Victoria, 1989

A THESIS SUBMITTED IN PARTIAL FULFILLMENT
OF THE REQUIREMENTS FOR THE DEGREE OF
MASTER OF SCIENCE
in the Department
of
Physics

SIMON FRASER UNIVERSITY

January 1995

APPROVAL

Name: James P. Zibin

Degree: Master of Science

Title of thesis: **The Approach to Classical Chaos in an Anharmonic Quantum Oscillator**

Examining Committee: Dr. J.R. Dahn
Chair

Dr. L.E. Ballentine
Senior Supervisor

Dr. D. Loss

Dr. R.H. Enns

Dr. M. Plischke
Internal Examiner

Date Approved: 26 January 1995

PARTIAL COPYRIGHT LICENSE

I hereby grant to Simon Fraser University the right to lend my thesis, project or extended essay (the title of which is shown below) to users of the Simon Fraser University Library, and to make partial or single copies only for such users or in response to a request from the library of any other university, or other educational institution, on its own behalf or for one of its users. I further agree that permission for multiple copying of this work for scholarly purposes may be granted by me or the Dean of Graduate Studies. It is understood that copying or publication of this work for financial gain shall not be allowed without my written permission.

Title of Thesis/Project/Extended Essay

The Approach to Classical Chaos in an Anharmonic Quantum Oscillator

Author: _____
(signature)

_____
(name)

February 17, 1995
(date)

Abstract

The question of how quantum mechanics approaches classical behaviour in the classical limit has long attracted interest, with a common view being that of quantum packets becoming more and more localized until, by Ehrenfest's theorem, their centroids follow a classical trajectory. The recent activity in the field of classical chaos has led to heightened interest in new aspects of correspondence. Questions now being addressed include the following: how can non-chaotic quantum mechanics approach chaos in the classical limit, and what features distinguish quantal evolution in classically chaotic systems from that in classically non-chaotic systems? In this thesis I attempt to answer these questions for a particular physical system, a classically chaotic driven quartic oscillator (DQO), using the numerical propagation of both quantum and classical states.

Since classical chaos is most usefully visualized in phase space, an attempt is made to represent the quantal evolution of the DQO in a way that generalizes classical phase space representations. The quantal evolution is compared with both classical single trajectories and classical distributions, as the DQO approaches the classical regime. It is argued that the quantal evolution for classically chaotic systems is fundamentally different from that for classically non-chaotic systems, in that a localized quantum state will rapidly delocalize on the time scale of the inverse Lyapunov exponent, thus invalidating the single-trajectory Ehrenfest view of correspondence. This does not indicate a failure of the correspondence principle, as classical statistical mechanics is shown to accurately describe the delocalized quantum state.

An intuitive approach is introduced to examine how sensitivity to perturbations,

a defining characteristic of classical chaos, is manifested in quantal dynamics. In addition, a number of possible extensions of the definition of Lyapunov exponents to quantum mechanics are explored. In all cases, agreement with classical mechanics is found for short DQO evolution times, and the manner in which the classical results are approached in the classical limit is indicated.

To the memory of my father.

Acknowledgements

I would like to gratefully acknowledge Dr. L. E. Ballentine for continual support during my M.Sc. program, and also for careful readings of this thesis and many helpful suggestions. I also extend my appreciation to Dr. D. Loss, Dr. R. H. Enns, and Dr. M. Plischke for their assistance on the supervisory committee. In addition, many thanks to Dominic Mimnagh and Bradley Hughes for many stimulating discussions, and to my family for their support during my studies. Finally, I must acknowledge the Natural Sciences and Engineering Research Council for gracious support.

Contents

List of Tables

List of Figures

Chapter 1

Introduction

The solar system is often considered a paradigm of predictable, regular motion, having maintained its structure over billions of years. It was in the orbital motion of three interacting celestial bodies, however, that the mathematician-astronomer Henri Poincaré and his contemporaries in the late nineteenth century first realized that a form of very irregular motion was possible. This type of behaviour has come to be known as *chaos*, and it is characterized by extreme sensitivity to initial conditions: the separation between two initially close trajectories in phase space increases exponentially with time. Most startling was the revelation that chaos was possible in Hamiltonian systems of only one or two degrees of freedom.

Mathematicians continued the development of chaos theory into the twentieth century. Between the 1950s and the 1970s Kolmogorov, Arnold, and Moser (KAM) showed that when a regular Hamiltonian system is perturbed, intricate regions of chaos typically form in the phase space, intermixed with regular "island chains". Their results indicated that chaos is expected to be a typical feature of physical systems. Since the work of KAM, dramatic increases in computational power have enabled the numerical study of numerous models, opening up the field to practical investigation. Chaos theory is now important to the understanding of fluid dynamics, non-linear optics, plasma physics, celestial mechanics, and many more fields outside of physics.

The importance of these developments to classical mechanics prompts us to examine what, if any, are the implications of classical chaos for quantum mechanics (or vice versa). Quantum mechanics, being a more general theory, should include the predictions of classical mechanics (including classical chaos) as some kind of limiting case. However, it appears that quantum mechanics does not allow chaos as it is defined classically, as we will see. What then is the evolution like for a quantum mechanical system whose classical counterpart is chaotic? And how does this behaviour approach classical chaos as the systems we consider become more and more macroscopic? These are the general questions which define the new field of quantum chaos. Practical systems to which these questions are being addressed include the hydrogen atom in strong uniform magnetic or microwave fields and the helium atom, each of which can exhibit chaos when treated classically.

1.1 Approaches to Quantum Chaos

Approaches to the problems of quantum chaos fall into a few broad categories. One approach is to study energy eigenstates and eigenvalues for systems which are chaotic when treated classically. Recent studies have revealed different energy-level statistics for classically chaotic and non-chaotic systems [1], and, in eigenstates of some classically chaotic systems, distinctive "scars", or regions of high probability density localized along classical unstable periodic orbits [2]. Another approach is to study classically chaotic quantum systems using semiclassical approximation techniques. These methods have been used successfully since the early part of this century on integrable systems, although not until the 1970s has progress been made on classically chaotic systems. Results have highlighted again the importance of classical unstable periodic orbits in determining the quantum mechanical behaviour [2, 3, 4].

A third approach, which I take in this thesis, is to study the time evolution of quantum states in phase space by numerically solving the time-dependent Schrödinger equation. This approach was chosen over the others for a number of reasons. First, it

allows a direct comparison between quantum and classical dynamics in the arena of phase space, where the essential aspects of classical chaos are most readily visualized (techniques for representing quantum states in phase space will be described in detail, together with the associated problems). In addition, the dynamical (time-domain) approach enables a comparison with corresponding classical quantities more readily than an energy-domain approach. Finally, this approach can probe exactly (subject to numerical errors, of course) the full quantum regime, whereas the semiclassical techniques involve approximations valid in the short-wavelength limit.

Pioneering work in studying the quantal evolution of classically chaotic systems (although not concerned with phase space representations) was done by Casati *et al.* [5]. The model they studied was the kicked rotor: a point mass free to rotate about a pivot, frictionlessly and in a vertical plane, and subject to a periodic impulsive vertical force. They chose this system because both classically and quantum mechanically it could be reduced to simple analytic mappings giving the state just after one kick in terms of the state just after the previous kick. When treated classically this system had been known to exhibit chaos and unbounded diffusion in momentum for certain parameter values. Casati *et al.* found that for parameters that gave momentum diffusion classically, the quantal evolution showed similar diffusion but only for a limited time. This suppression of diffusion was subsequently explained as analagous to the Anderson localization mechanism for electrons in random lattices [6]. Korsch and Berry [7] studied a related system also reducible to a mapping, a kicked anharmonic oscillator, but extended the analysis to phase space representations. The quantal suppression of momentum diffusion is thought to explain some recent observations: a suppression of ionization in highly excited hydrogen atoms in strong microwave fields at certain frequencies [8].

Mappings, although computationally efficient, can only be derived for a restrictive class of systems. The increase in available computational power, however, has enabled the study of more general systems by direct numerical integration of Schrödinger's or Hamilton's equations. Christoffel and Brumer [9] studied the classical and quantal

evolution for a particle confined to a two-dimensional stadium-shaped box, a system known to be classically chaotic. Takahashi [10] examined a classically chaotic double-well potential system. The results of both these studies pointed out the usefulness of comparing quantal evolution with classical distribution dynamics (rather than single-trajectory dynamics) when the system is classically chaotic, a point that will be elaborated upon in this thesis.

The work in this thesis was intended as an extension of the work of Christoffel and Brumer and Takahashi. It involves the numerical propagation of quantum states for a classically chaotic system: the one-dimensional driven quartic oscillator, whose quasienergy states and behaviour of autocorrelation fuctions have been studied by Ben-Tal *et al.* [11, 12]. Various dynamical aspects of the quantal evolution will be compared with the results of numerical calculations for the same system treated classically. Both single trajectories and distributions will be considered classically. In addition, an attempt will be made to characterize quantitatively the quantal time evolution for the classically chaotic system in a way that generalizes the usual methods of characterizing classical chaos. Emphasis will be placed throughout on illuminating the way that quantal dynamics approaches classical chaos as a system becomes macroscopic.

1.2 Phase Space and the Classical Regime

The study of quantum chaos emphasizes the importance of various conceptual issues in quantum mechanics. Indeed, as described above, central to classical chaos is the idea of exponentially separating trajectories in phase space. But quantum mechanics does not even allow the description of precise phase space trajectories. One might argue that the uncertainty inherent in quantum mechanics suggests instead that, in order to attempt a phase space representation of quantum mechanics, we consider extended phase space densities, like the classical Liouville density. However, no "true" joint probability density for position and conjugate momentum has been constructed

in quantum mechanics, although several phase space densities can be formed which have many of the required properties, as will be described. The important point is that we expect to be able to construct a quantum mechanical quantity which, although it does not have the usual classical interpretation, nevertheless *does* reduce to a usual classical quantity in the classical limit. Studying the behaviour of this quantum mechanical quantity should help us to understand how ordinary chaos emerges in the classical limit.

A related issue is raised by the question: To *what* does our constructed quantum mechanical quantity correspond classically, a phase space trajectory or density? The issue is tied to that of the interpretation of the quantum mechanical state vector itself: Does a state vector correspond to an individual classical system or to an ensemble of systems? I will assume neither interpretation and keep to the standard formalism of quantum mechanics, although the results obtained in this work will help clarify this issue. In addition I will *not* address the issue of measurement in quantum mechanics. Although it might appear that the probabilistic or "random" nature of a quantum mechanical measurement is relevant to the topic of quantum chaos, it is sufficient for the problems considered here, as we will see, to consider only the deterministic quantal evolution governed by Schrödinger's equation (and which everyone agrees upon).

It is important when discussing the classical limit of quantum mechanics to define precisely what is meant by this limit. In the literature the expression $\hbar \to 0$ is usually used to indicate the classical limit. Of course $\hbar$ is a physical constant, and what is actually meant is that the dimensionless ratio $\hbar/S \to 0$, where S is a typical action for the system. This is the definition I will use throughout this thesis. The macroscopic world is characterized by very small, but non-zero values of $\hbar/S$, and the condition $\hbar/S \simeq 0$ will define the *classical regime*. In addition, by the *correspondence principle* I will mean that as $\hbar/S$ decreases, the predictions of quantum mechanics should agree better and better with those of classical mechanics, and in the classical regime the two theories should agree (to within experimental errors) where classical mechanics

is known to be valid.

1.3 Quantal Evolution in Classically Chaotic Systems

Another issue concerns the nature of the time evolution of a quantum mechanical state under a Hamiltonian which generates chaos when treated classically. As mentioned above it is believed that the quantal evolution is not chaotic. It is sometimes argued [13] that this is a result of the linearity of the Schrödinger equation, since a condition for classical chaos is non-linear Hamilton's equations. To help clarify this point, consider a single chaotic classical system evolving under a Hamiltonian $H(q,p)$ and tracing out a trajectory $(q(t),p(t))$ in phase space. Suppose that at initial time t_0 a perturbed trajectory is formed by adding a small perturbation $(\delta q(t_0),\delta p(t_0))$ to the original trajectory. Then, as the perturbed trajectory evolves, the perturbation $(\delta q(t),\delta p(t))$ will grow rapidly because of the sensitive dependence on initial conditions. Now consider a quantum mechanical system evolving under the corresponding quantized Hamiltonian with state vector $|\Psi(t)\rangle$. Again consider adding a perturbation $|\delta\Psi(t_0)\rangle$ of small norm at time t_0. However now, because the Schrödinger equation is linear, the perturbation $|\delta\Psi(t)\rangle$ will itself evolve according to the Schrödinger equation, so we can write

$$|\delta\Psi(t)\rangle = U(t,t_0)|\delta\Psi(t_0)\rangle \tag{1.1}$$

where $U(t,t_0)$ is the unitary time evolution operator. Thus

$$\langle\delta\Psi(t)|\delta\Psi(t)\rangle = \langle\delta\Psi(t_0)|U^\dagger(t,t_0)U(t,t_0)|\delta\Psi(t_0)\rangle = \langle\delta\Psi(t_0)|\delta\Psi(t_0)\rangle, \tag{1.2}$$

so that the norm of the perturbation does not grow, regardless of the nature of the Hamiltonian. Alternatively, we have

$$\langle\Psi(t)|\left[|\Psi(t)\rangle + |\delta\Psi(t)\rangle\right] = \langle\Psi(t_0)|\left[|\Psi(t_0)\rangle + |\delta\Psi(t_0)\rangle\right], \tag{1.3}$$

meaning that the overlap between the unperturbed and perturbed states remains constant.

Although this appears to rule out the sensitive dependence which characterizes classical chaos, a parallel situation does in fact exist in classical mechanics. We can describe a classical system by a Liouville density in phase space, $\rho_{\mathrm{L}}(q,p,t)$, which evolves according to Liouville's equation,

$$\frac{\partial \rho_{\mathrm{L}}}{\partial t} = -\frac{\partial H}{\partial p}\frac{\partial \rho_{\mathrm{L}}}{\partial q} + \frac{\partial H}{\partial q}\frac{\partial \rho_{\mathrm{L}}}{\partial p}, \tag{1.4}$$

which is linear in ρ_{L} (in the case of a single system rather than an ensemble, the density reduces to a delta function which traces out the trajectory specified by Hamilton's equations). Again we can imagine our particular state, represented by the density $\rho_{\mathrm{L}}(q,p,t)$, perturbed at t_0 to the state $\rho_{\mathrm{L}}(q,p,t_0) + \delta\rho_{\mathrm{L}}(q,p,t_0)$. The fact that Liouville's equation represents conservative probability density flow means that the overlap between the unperturbed and perturbed states, $\int \rho_{\mathrm{L}}(\rho_{\mathrm{L}} + \delta\rho_{\mathrm{L}})\, dq\, dp$, remains constant in time (a statement analagous to the quantal equation (1.3)), ruling out sensitive dependence for the quantity ρ_{L}. This is not inconsistent with the rapid growth of trajectory perturbations described above. In the Liouville picture, two initially close trajectories are represented by two delta functions, which will always have zero overlap. The point here is just that we must keep in mind what our equations are linear or non-linear *in,* especially when considering issues of quantum-classical correspondence.

Despite this lack of sensitivity to perturbations in ρ_{L}, we still have sensitivity in classical Hamiltonian mechanics, and apparently no way of expressing quantum mechanics that exhibits such sensitivity. A reconciliation of these facts will be the subject of section 4.1.

A better argument for the lack of chaos in quantum mechanics concerns the discrete nature of the energy spectrum for a bounded quantum system (classical chaos is ordinarily concerned with bounded systems to exclude systems which trivially exhibit sensitive dependence, such as an unstable quadratic potential). Consider a

state $|\Psi(t)\rangle$ evolving under a time-independent Hamiltonian H. We can write the time evolution operator as

$$U(t, t_0) = e^{-i(t-t_0)H/\hbar}, \tag{1.5}$$

and we also have a discrete set of energy eigenfunctions $|\phi_n\rangle$ with eigenvalues E_n, and which satisfy the completeness relation

$$\sum_n |\phi_n\rangle\langle\phi_n| = I, \tag{1.6}$$

where I is the identity operator. Thus we can write for the overlap between the state at time t_0 and time t

$$\begin{aligned} \langle\Psi(t_0)|\Psi(t)\rangle &= \langle\Psi(t_0)|e^{-i(t-t_0)H/\hbar}|\Psi(t_0)\rangle & (1.7)\\ &= \sum_n \langle\Psi(t_0)|e^{-i(t-t_0)H/\hbar}|\phi_n\rangle\langle\phi_n|\Psi(t_0)\rangle & (1.8)\\ &= \sum_n |\langle\phi_n|\Psi(t_0)\rangle|^2 e^{-i(t-t_0)E_n/\hbar}. & (1.9) \end{aligned}$$

This last quantity is exactly periodic as a function of t when the eigenfrequencies $E_n/\hbar$ are commensurate, as is the case for a harmonic oscillator or a particle in a box. In general, though, (1.9) will be quasiperiodic so we expect that the overlap will exhibit partial recurrences on the time scale

$$T \sim \frac{\hbar}{\Delta E} \tag{1.10}$$

where ΔE is a typical energy level spacing in the state $|\Psi\rangle$. As will be shown in section 3.4.1, these "quantum recurrences" can actually have a classical origin. Nevertheless, this crude argument can be improved: it can be shown [14] that even under an arbitrary time-periodic Hamiltonian, a bounded quantum state will always recur (to any arbitrary accuracy) periodically. This is in stark contrast to the aperiodic nature of classical chaos. Speaking loosely, it is almost as if we added some milk to a cup of tea, began stirring, and as we continued to stir noticed that the milk separated from the tea from time to time.

A number of more specific issues regarding the quantal time evolution of classically chaotic systems have been raised in the literature recently. Each of these issues will

be described briefly below and discussed later in light of the results presented in this thesis.

Fox and Lan [15, 16] have shown that there is a close link between the classical behaviour of initially close trajectories in phase space and the quantal evolution of the position and momentum widths of initially well localized wave packets. In particular, for a classically chaotic system, the position and momentum widths of a localized packet will grow exponentially with time. They claim that this contradicts the correspondence principle, in that this exponential spread for a macroscopic state will rapidly invalidate the single-trajectory classical picture. This issue will be examined in the third chapter of this thesis.

Shepelyansky [17] and Casati *et al.* [18] have performed numerical experiments to study the "practical irreversibility" in the kicked rotor and in a model of hydrogen in a microwave field. All systems governed by Schrödinger's or Hamilton's equations are of course exactly reversible in the sense that reversing the momenta of a classical system or taking the complex conjugate of a quantum state will cause the system, *ideally,* to precisely retrace its history. By "practical irreversibility" in a system these researchers refer to the inaccurate retracing of a history that occurs when such a motion reversal experiment is conducted numerically by computer. They have found that for their classically chaotic systems, the quantal evolution was far more practically reversible (*i.e.* much more accurately retraced its history) than the same system treated classically. Based on these results, Ford and Ilg [19] have suggested that it might be possible for certain experiments to test the validity of quantum mechanics in the classical regime. Calculations of this sort will be discussed in the fourth chapter.

Ford *et al.* [19, 20] also suggest that the field of "algorithmic complexity theory" has relevance to the issue of quantum-classical correspondence in classically chaotic systems. They show [19] that for the class of bounded undriven classically chaotic systems, the quantities calculated by the two theories differ in their numerical structure, quantal and classical quantities being "algorithmically compressible" and

"incompressible", respectively. This means, essentially, that if we wish to calculate a final state (at time $t = t_f$) of a classically chaotic system to some particular accuracy, then the initial state (at $t = t_0$) must be specified to a number of significant digits that grows linearly with $t_f - t_0$ for the classical system but only logarithmically for the corresponding quantum system. Thus, loosly speaking, it appears to be much "easier" to perform a quantum calculation than the corresponding classical calculation, a result Ford *et al.* claim holds even in the classical limit, and which, they state, contradicts the correspondence principle. This final issue will be resolved in the concluding chapter.

Chapter 2 of this thesis will contain a description of the numerical techniques used for both the quantum and classical calculations. In addition, for the quantum calculations, the numerical calculations will be compared with the analytical solution for a driven harmonic oscillator to examine their accuracy, and several numerical integrators will be compared for their efficiency.

Chapter 3 will contain a study of the time evolution of the driven quartic oscillator in phase space. First, the classical single-trajectory dynamics will be described, including the Poincaré section and Lyapunov exponents. Next quantal phase space representations will be introduced, and their problems discussed. Then a detailed comparison of the quantal and classical phase space dynamics will be presented, for both classically chaotic and non-chaotic parameter values, and involving both classical distributions and single trajectories.

The fourth chapter will begin with a description of a new approach to "practical irreversibility" which is more physically meaningful than the approaches of previous studies. Then four techniques for quantitatively characterizing the quantal time evolution for classically chaotic systems will be presented and compared. Each technique attempts to generalize the classical Lyapunov exponent.

The final chapter will present the conclusions of this work.

Chapter 2

Calculation Methods

In the Introduction I explained that an important part of this thesis is the comparison of quantum and corresponding classical dynamics for a classically chaotic system. Both the quantum and classical systems studied here require a non-analytic approach to solution, and this chapter will contain a description of the numerical methods used. The quantum calculations were considerably more time consuming than the classical ones, so a detailed study of the accuracy and efficiency of the quantum techniques will be presented as well.

2.1 Classical Calculations

There were two basic types of classical calculations. These were the numerical calculation of the phase space trajectory for a single particle, and the numerical propagation of a Liouville phase space distribution. The single trajectory calculations were very straightforward. The particle's position (q) and momentum (p) coordinates were specified at some initial time, and then the approximate coordinates at a later time were obtained by numerical integration of Hamilton's equations,

$$\dot{q} = \frac{\partial H}{\partial p}, \tag{2.1}$$

$$\dot{p} = -\frac{\partial H}{\partial q}, \tag{2.2}$$

where $H(q,p,t)$ is the classical Hamiltonian. A variable-order variable-time-step Adams method ordinary differential equation (ODE) integrator, routine D02CAF from the Numerical Algorithms Group (NAG) library of Fortran routines [21], was chosen to integrate (2.1) and (2.2). Reference [22] contains a detailed account of Adams methods.

For the distribution calculations, one possible approach would be to specify some initial Liouville density, $\rho_{\mathrm{L}}(q,p)$, and then integrate forward in time the partial differential Liouville's equation, (1.4), by performing a phase space discretization of the density (a technique similar to that used for the quantum calculations, as described in the next section). However, this technique would be far more time consuming than even the quantum calculations for two reasons. First, Liouville's equation contains one more independent variable than Schrödinger's equation. In addition, for system parameters that produce chaos, we will see that the size of the finest structures in the Liouville density decreases very rapidly with time, which means that we would require an extremely fine phase space discretization of the Liouville equation for even moderate propagation times.

Instead, in this work the initial Liouville density was approximated by choosing the initial q and p values for a large ensemble of particles randomly according to the required initial distribution, and then integrating each individual trajectory forward in time by the technique described above. At any particular time, the values of ρ_{L} on a phase space grid were then calculated by simply counting the number of trajectories lying within each cell of the grid, followed by appropriate normalization. The number of particles used in the ensembles depended on the purpose of the calculation, and will be stated in later sections.

The random initial q and p coordinates were chosen in two ways. Most of the calculations involved initial Liouville densities which were Gaussian in both position and momentum. In this case, the coordinates were produced by a NAG normal distribution random number generator, routine G05DDF. The algorithm used in this routine is described in reference [23]. Some calculations involved non-Gaussian initial

distributions. For these, software was obtained which used the following technique. To generate position coordinates, *e.g.*, with a particular probability distribution $P(q)$, the cumulative probability distribution

$$P_{\text{cum}}(q) = \int_{-\infty}^{q} P(q')dq' \tag{2.3}$$

was first calculated. As q increases from $-\infty$ to ∞, $P_{\text{cum}}(q)$ increases monotonically from 0 to 1. A real number R such that $1 \geq R \geq 0$ was produced by a random number generator with a uniform distribution, and the corresponding q value was obtained through inversion of $P_{\text{cum}}(q) = R$. This process was repeated many times to build up the required initial ensembles in position and momentum.

2.2 Quantum Calculations

2.2.1 The Technique

The goal of the quantum calculations was to find an approximate solution to the coordinate representation time-dependent Schrödinger equation,

$$\frac{\partial}{\partial t}\Psi(x,t) = \frac{-i}{\hbar}H\Psi(x,t), \tag{2.4}$$

given an initial state function $\Psi(x,0)$. Here H is the Hamiltonian operator. The Hamiltonians studied in this work can be written

$$H = \frac{-\hbar^2}{2m}\frac{\partial^2}{\partial x^2} + V(x,t), \tag{2.5}$$

where $V(x,t)$ is a time-dependent potential which keeps the particle of mass m bounded. The technique used was to approximate the spatial derivative in (2.4) by finite differences, yielding a large set of coupled ODEs in time which was integrated using available ODE integration packages. Techniques for representing the calculated state function in phase space will be described in the next chapter.

The finite difference approximation involves replacing the continuous spatially dependent $\Psi(x,t)$ by a state function $\Psi_j(t)$ defined only on a lattice of N discrete,

uniformly spaced grid points labeled by the index j (similarly, $V(x,t)$ is replaced by $V_j(t)$). In this approximation a spatial derivative can be written

$$\frac{\partial}{\partial x}\Psi(x,t) \simeq \frac{\Psi_{j+1}(t) - \Psi_j(t)}{\Delta x}, \tag{2.6}$$

where Δx is the grid spacing, and indices j and $j+1$ correspond to positions x and $x+\Delta x$, respectively. The second derivative becomes

$$\frac{\partial^2}{\partial x^2}\Psi(x,t) \simeq \frac{\Psi_{j+1}(t) - 2\Psi_j(t) + \Psi_{j-1}(t)}{(\Delta x)^2}. \tag{2.7}$$

Thus the Schrödinger equation can be approximated by the set of N coupled ODEs

$$\begin{aligned} \frac{d\Psi_j(t)}{dt} &= \frac{i\hbar}{2m(\Delta x)^2}\left[\Psi_{j+1}(t) - 2\Psi_j(t) + \Psi_{j-1}(t)\right] \\ &\quad -\frac{i}{\hbar}V_j(t)\Psi_j(t), \qquad \text{for } j = 1, 2, \ldots, N. \end{aligned} \tag{2.8}$$

Periodic boundary conditions were imposed, so that $\Psi_{j+N} = \Psi_j$. Many numerical ODE integrators are available to integrate (2.8). A comparison of the efficiency and accuracy of several routines will be presented in section 2.2.3.

A number of requirements must be satisfied when applying this finite difference technique to a problem [24]. First, the grid spacing Δx must be small enough not to introduce significant error into the integration. This requirement can be phrased in terms of the shortest wavelength, $\lambda_{\min}$, that contributes significantly to the state $\Psi(x,t)$. We clearly require that $\Delta x < \lambda_{\min}/2$. This can be restated using the largest momentum contributing to the state, $p_{\max} = 2\pi\hbar/\lambda_{\min}$, as

$$\Delta x < \frac{\pi\hbar}{p_{\max}}. \tag{2.9}$$

We will see that a good estimate of $p_{\max}$ can be obtained from the classical dynamics.

Another requirement is that the wave function at the boundaries ($\Psi_1(t)$ and $\Psi_N(t)$) have negligible values for the entire duration of the integration. This is relatively easy to accomplish, we will find, for the bounded systems considered here. In addition, when this requirement is satisfied, the form of the boundary conditions chosen becomes unimportant.

A final requirement concerns the time integration carried out by the ODE integrator. This integration will involve some form of temporal finite difference scheme, and hence a time step. This time discretization can introduce relative phase shifts between components of the state function. The ODE integrators used employ variable time steps which cannot be directly adjusted, although it will still be possible to determine that the time discretization does not introduce significant error.

2.2.2 The Driven Harmonic Oscillator

After the software to perform the finite difference integration of Schrödinger's equation was ready, it was tested on the driven harmonic oscillator (DHO). The DHO is similar to the anharmonic driven quartic oscillator, which will be studied in detail in the following chapters, in that it represents a one-dimensional particle bound in a smooth potential and driven sinusoidally. However, the DHO does not exhibit chaos when treated classically, and quantum mechanically analytical solutions can be found for certain initial conditions. The comparison between these exact solutions and the numerical calculations will be the subject of this section.

The Hamiltonian for the DHO in coordinate representation is

$$H = \frac{-\hbar^2}{2m}\frac{\partial^2}{\partial x^2} + \frac{1}{2}kx^2 + a\cos(\omega' t)x, \tag{2.10}$$

where k is the spring constant and ω' and a the driving frequency and amplitude, respectively. It is shown in Appendix A that if the initial state is a Gaussian centred at $x = q_0$,

$$\Psi(x,0) = \left[(2\pi)^{1/2}\sigma_x\right]^{-1/2} e^{i\phi_0 - (x-q_0)^2/(4\sigma_x^2)}, \tag{2.11}$$

with position standard deviation σ_x equal to the field-free harmonic oscillator ground state value $\left[\hbar/(4km)^{1/2}\right]^{1/2}$ and initial phase ϕ_0, then the state will evolve without spreading as a Gaussian whose mean position $q(t)$ and mean momentum $p(t)$ follow precisely the coordinates of a classical particle with initial coordinates $(q(0), p(0)) = (q_0, 0)$ evolving under the classical Hamiltonian corresponding to (2.10). This evolution is accompanied by a non-trivial time-dependent phase factor. Explicitly, it is

shown in Appendix A that the initial state (2.11) evolves according to

$$\Psi(x,t) = \left[(2\pi)^{1/2}\sigma_x\right]^{-1/2} e^{i\phi(t)} e^{-ip(t)q(t)/(2\hbar)} e^{ip(t)x/\hbar} e^{-(x-q(t))^2/(4\sigma_x^2)}, \tag{2.12}$$

where

$$\begin{aligned} q(t) &= b\cos(\omega t) + \frac{a}{m(\omega'^2 - \omega^2)}\cos(\omega' t), && (2.13)\\ p(t) &= m\dot{q}, && (2.14)\\ \phi(t) &= \phi_0 - \frac{\omega t}{2} - \frac{ab}{4\hbar}\left[\frac{\sin(\omega'-\omega)t}{\omega'-\omega} + \frac{\sin(\omega'+\omega)t}{\omega'+\omega}\right] \\ &\quad - \frac{a^2}{4m\hbar\omega'(\omega'^2-\omega^2)}\left[\omega' t + \frac{1}{2}\sin(2\omega' t)\right], && (2.15) \end{aligned}$$

and where $\omega = (k/m)^{1/2}$ is the natural frequency of the harmonic oscillator and

$$b = q_0 - \frac{a}{m(\omega'^2 - \omega^2)}. \tag{2.16}$$

The numerical propagation of DHO states required choosing specific numerical values for the various parameters described above. These were chosen so that the dynamical time scales, regions of position and momentum space accessed, and size of quantum effects (determined by the relative size of $\hbar$ and typical system actions) were similar to the corresponding properties for the driven quartic oscillator studied in later chapters. The values chosen were $\hbar = 0.02$, $m = 1$, $\sigma_x = (0.03)^{1/2}$, $\omega = 1/3$, $\omega' = 1$, $a = -8/27$, $q_0 = -1$, and $\phi_0 = 0$. With these parameter values the centroid (mean position and mean momentum) of the Gaussian wave packet followed a classical trajectory which was confined to the interval $-1 \leq x \leq 1$. The boundaries for the integration were chosen to be at $x = \pm 2.5$, which meant that the value of the normalized wave function at the boundaries was always less than 1.1×10^{-8}. The maximum momentum value that occurred "significantly" in the evolving state, *i.e.* with a momentum probability distribution value greater than 10^{-20}, was $p_{\max} \simeq 1.0$, which, by equation (2.9), meant that at least $N \simeq 80$ spatial grid points were needed to resolve the state. The time integration of (2.8) was performed by the NAG Runge-Kutta-Merson routine D02BAF, which will be described in the next section.

Figure 2.1 shows a comparison between the exact DHO state Ψ_{exact} given by equation (2.12) and the state Ψ_{calc} calculated using the numerical technique described above and with the given parameter values. Both states were calculated for the time $t = 5.25T$, where $T = 2\pi/\omega'$ is the period of the driving force. At this time the Gaussian state is centred at $x = 0$ and figure 2.1 shows only the region $-0.5 \leq x \leq 0.5$ where the probability density has non-negligible values. The upper graph in figure 2.1 displays the relative density error $|\Psi_{\text{calc}}|^2/|\Psi_{\text{exact}}|^2$ for various values of N and the lower graph gives the phase angle difference between Ψ_{calc} and Ψ_{exact} versus N. Both figures indicate a clear convergence of the numerically calculated state to the exact state as N increases.

To illustrate how the numerical errors grow with propagation time, figure 2.2 shows $|\Psi_{\text{calc}}|^2/|\Psi_{\text{exact}}|^2$ and the phase error for fixed $N = 2000$ and for the times $t = 5.25T$, $11.25T$, $17.25T$, and $23.25T$. These figures indicate a roughly linear growth of density and phase errors over the time interval studied.

The accuracy of the time integration carried out by the NAG routine is determined by a "tolerance" input parameter. The routine attempts to keep the absolute error in the calculated state proportional to the set tolerance value. The calculations presented in figures 2.1 and 2.2 used a tolerance value of 10^{-7}, although no significant difference in the density or phase errors or in the machine integration time was found for tolerances of 10^{-5} and 10^{-9}. This indicates that the time integration routine was producing a sufficiently accurate solution to the spatially discretized problem, equation (2.8), and therefore that the number of grid points N was primarily responsible for determining the accuracy of the calculations.

2.2.3 A Comparison of ODE Integrators

Four numerical ODE integration routines were obtained and compared for efficiency in performing the time integration of the spatially discretized Schrödinger equation (2.8). The routines were of the Runge-Kutta and Adams types. The Runge-Kutta routines propagate an initial state $\Psi_j(0)$ forward one time step Δt at a time using

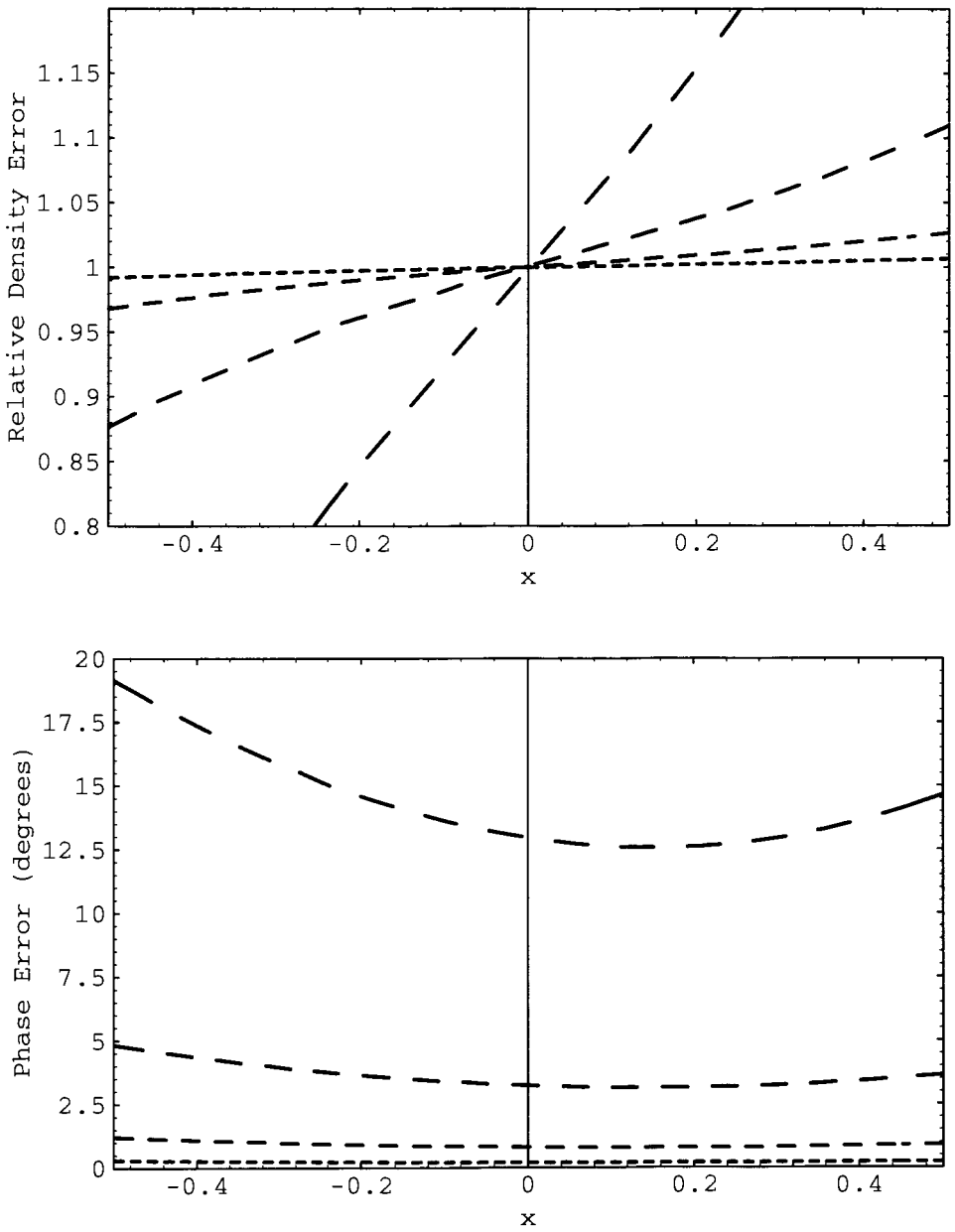

Figure 2.1: Relative density error $|\Psi_{\text{calc}}|^2/|\Psi_{\text{exact}}|^2$ (top) and phase error (bottom) for numerically calculated DHO state at $t = 5.25T$. In order of decreasing dash size, the curves are for $N = 500$, 1000, 2000, and 4000 grid points. NAG routine D02BAF was used to integrate the spatially discretized Schrödinger equation.

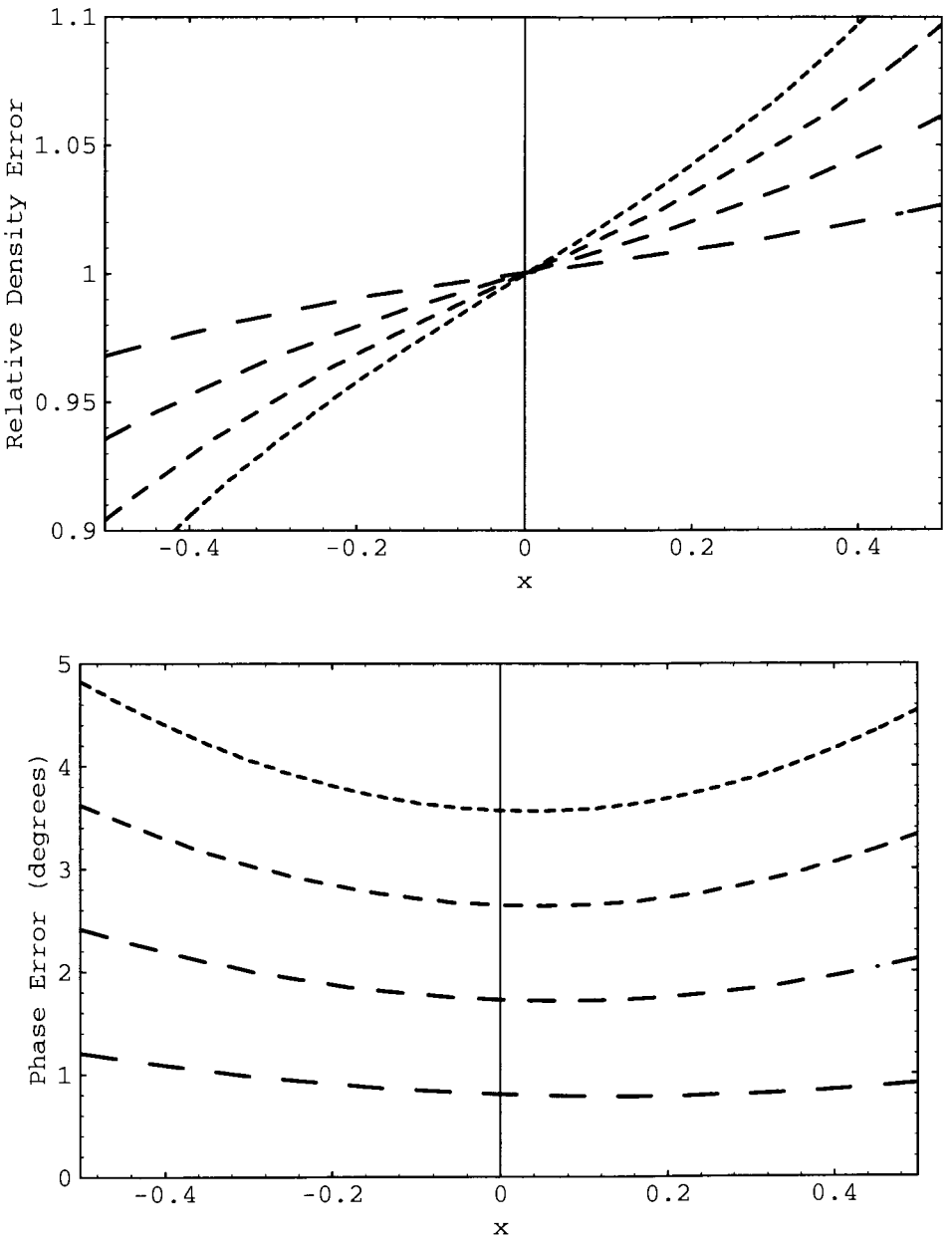

Figure 2.2: Relative density error $|\Psi_{\text{calc}}|^2/|\Psi_{\text{exact}}|^2$ (top) and phase error (bottom) for numerically calculated DHO state using $N = 2000$ spatial grid points. In order of decreasing dash size, the curves are for $t = 5.25T$, $11.25T$, $17.25T$, and $23.25T$ (T is the period of the driving force). NAG routine D02BAF was used to integrate the spatially discretized Schrödinger equation.

some finite order approximation to the Taylor expansion

$$\Psi_j(\Delta t) = \Psi_j(0) + \Delta t \left.\frac{d\Psi_j(t)}{dt}\right|_{t=0} + \frac{(\Delta t)^2}{2!} \left.\frac{d^2\Psi_j(t)}{dt^2}\right|_{t=0} + \cdots . \tag{2.17}$$

The routines evaluate the first derivative $d\Psi_j(t)/dt$ directly using equation (2.8); higher-order derivatives are matched (to the required order) to Taylor expansions of the first derivative.

The Adams methods are based upon the exact expression

$$\Psi_j(\Delta t) = \Psi_j(0) + \int_0^{\Delta t} \frac{d\Psi_j(t)}{dt} dt. \tag{2.18}$$

These methods approximate $d\Psi_j(t)/dt$ in the integrand by a polynomial fit using the calculated values of this derivative at several previous time steps. In both Adams and Runge-Kutta methods, the time step Δt is adjusted automatically at each step according to a preset tolerance value or values.

The first ODE integrator tried was the Runge-Kutta-Merson NAG routine D02BAF. Use of this routine requires setting a single absolute tolerance parameter, and the routine adjusts Δt at each step to try keep the absolute error in the calculated state proportional to the tolerance.

The NAG routine D02CAF, which uses a variable-order Adams method, was also considered. This routine also uses a single absolute tolerance parameter. A detailed description of the numerical methods used in both NAG routines is contained in reference [22].

The next ODE integrator investigated was the fifth and sixth order Runge-Kutta-Verner routine DVERK, from the International Mathematical and Statistical Library of routines [25]. This integrator also uses an absolute tolerance.

The final integrator tried was a variable-order Adams routine by L. F. Shampine and M. K. Gordon [26] (henceforth referred to as the Shampine routine). This routine requires setting both an absolute and a relative tolerance.

These four routines were compared for their efficiency in integrating equation (2.8) for the DHO Hamiltonian (2.10), using the same system parameters and initial

state given in section 2.2.2. The initial state was propagated to $t = 6T$ (six periods of the driving force), for $N = 500$ and 1000 spatial grid points, and for various tolerance values. The machine integration times are summarized in Table 2.1. For each routine, varying the tolerance(s) by a factor of 100 resulted in negligible changes in relative density and phase errors and machine integration times. In addition, there were negligible differences in errors among the various routines for fixed N. Thus, as explained at the end of the previous section, each routine produced a sufficiently accurate solution to the spatially discretized problem, and it is reasonable to compare the machine integration times for the various routines (for fixed N). The NAG routine D02BAF, being several times faster than its closest competitor, was chosen as integrator for the remainder of this work. Note that the integration times for all four routines rapidly increase with N at similar rates, so routines slow at small N will not outperform D02BAF at large N.

Table 2.1: Machine integration times for four ODE integrators. The initial DHO state was propagated to $t = 6T$, using $N = 500$ and 1000 spatial grid points. The tolerance settings used (absolute or relative) are also indicated.

Routine	Tolerance(s)	Machine integration time for	
		$N = 500$	$N = 1000$
D02BAF	1.0×10^{-7} (abs.)	94s	13m
D02CAF	1.0×10^{-7} (abs.)	580s	86m
DVERK	1.0×10^{-7} (abs.)	435s	71m
Shampine	1.0×10^{-7} (abs.) 1.0×10^{-4} (rel.)	1460s	194m

Chapter 3

The Driven Quartic Oscillator in Phase Space

Most of the results presented in this thesis stem from a study of a particular physical system, the one-dimensional driven quartic oscillator (DQO). This system can exhibit chaos when treated classically, and this chapter begins with a description of the classical single-trajectory phase space dynamics, including Poincaré sections and Lyapunov exponents.

In the Introduction I mentioned the importance of representing quantum mechanics in phase space in a way that generalizes classical phase space dynamics. The remainder of this chapter will attempt to shed light on how this should be done, and in particular whether our quantal phase space representation should reduce to classical distributions or individual trajectories in the classical limit. Section 3.2 introduces quantum phase space distributions, which attempt to generalize classical distributions, and presents a comparison of the numerically calculated quantal and classical distribution evolution for the DQO. Ehrenfest's theorem, which relates quantal expectation values to a classical trajectory, is the subject of section 3.3. The validity of this theorem will be investigated using numerical calculations on the DQO. Section 3.4 will present arguments which attempt to tie together the results of the numerical calculations and which apply to a much broader class of systems than the DQO.

3.1 Classical Single-trajectory Dynamics

3.1.1 The System

The DQO studied here has the classical Hamiltonian

$$H(q,p,t) = \frac{p^2}{2m} + bq^4 - a\cos(\omega t)q, \tag{3.1}$$

where q, p, and m are the particle's position, momentum, and mass, respectively, a and ω are the driving amplitude and frequency, and b is a constant. This Hamiltonian could model a number of physical systems. A simple mechanical example is a horizontal degree of freedom of a particle in a uniform gravitational field sliding frictionlessly on a ramp with an appropriate height profile. The driving could be provided by sinusoidally translating the entire ramp horizontally, or, for a charged particle, by applying an oscillating, spatially uniform, horizontal electric field. The DQO defined by equation (3.1) is related to the classically well-studied Duffing oscillator [27], which consists of a driven, damped particle in a double-well potential, and is known to be chaotic for certain parameter ranges.

The DQO (3.1) was chosen to study here for a number of reasons. First was its simplicity, which, for the quantum calculations, enabled a numerical exploration deeper into the classical regime and to longer propagation times than would have been possible with a higher-dimensional system or more complicated potential. Also, this DQO had been known to exhibit classical chaos for certain parameter values, with sharply defined boundaries between chaotic and regular regions in phase space [11]. Finally, although Ben-Tal *et al.* have investigated the quasienergy states [11] and behaviour of autocorrelation functions [12] for this system, the phase space quantal dynamics of this DQO do not appear to have been studied.

On first glance the Hamiltonian (3.1) may appear to have a formidable four-dimensional parameter space to explore. A simple change of units, however, can remove three parameters. To see this, consider the rescaled variables

$$t' = \omega t, \quad q' = b^{1/4}q, \quad p' = \frac{p}{(2m)^{1/2}}, \tag{3.2}$$

which correspond to a change in the units of time, length, and mass, respectively. With this rescaling the Hamiltonian becomes

$$H(q', p', t') = p'^2 + q'^4 - a' \cos(t')q', \tag{3.3}$$

where $a' = ab^{-1/4}$. Thus varying all but one parameter is equivalent to changing units, and will not produce distinct DQO systems. In all numerical calculations to follow only the Hamiltonian in the form (3.1) was used, with the parameter values $m = 1$, $b = 1/4$, $a = 1/2$, and $\omega = 1$. This choice of parameters produced interesting phase space structure, as illustrated in the next section. Note that when considering the quantal analogue of (3.1) one additional independent parameter, a scaled $\hbar$, will arise.

From a general mathematical perspective, a necessary condition for chaos in a set of first-order autonomous ODEs is that the set consist of at least three coupled ODEs, some of which contain nonlinearities [1]. To see that our DQO satisfies this condition, note that Hamilton's equations (2.1) and (2.2) become for the DQO Hamiltonian (3.1)

$$\dot{q} = \frac{p}{m}, \tag{3.4}$$

$$\dot{p} = -4bq^3 + a\cos(\omega t). \tag{3.5}$$

The explicit time dependence on the rhs of (3.5) can be removed with the definition of a new variable $\xi = \omega t$, so that (3.5) becomes

$$\dot{p} = -4bq^3 + a\cos\xi, \tag{3.6}$$

$$\dot{\xi} = \omega. \tag{3.7}$$

Equations (3.4), (3.6), and (3.7) form the required set of ODEs. Qualitative and quantitative indications that chaos does in fact occur in the classical DQO will be the topic of the next two sections.

A useful approximation to the full nonlinear DQO dynamics can be obtained by considering the time evolution of a small perturbation from a trajectory. To accomplish this, first consider a general one-dimensional system governed by the

classical Hamiltonian $H = p^2/(2m) + V(q,t)$. Note that Hamilton's equations of motion can be summarized in matrix form as

$$\frac{d\mathbf{x}}{dt} = \begin{pmatrix} p/m \\ -\partial V/\partial q \end{pmatrix} \equiv \mathbf{F}(\mathbf{x}), \tag{3.8}$$

where $\mathbf{x}$ is the column vector of coordinates $\begin{pmatrix} q \\ p \end{pmatrix}$. The evolution of a small perturbation $\delta\mathbf{x}(t)$ from a particular trajectory, which will be referred to as the *fiducial* trajectory, $\mathbf{x}_\mathrm{f}(t)$, is determined by the Taylor expansion

$$\frac{d(\delta\mathbf{x})}{dt} = \left.\frac{d\mathbf{F}(\mathbf{x})}{d\mathbf{x}}\right|_{\mathbf{x}_\mathrm{f}} \delta\mathbf{x} + \cdots, \tag{3.9}$$

where the notation $d\mathbf{F}/d\mathbf{x}$ refers to the Jacobian matrix

$$\frac{d\mathbf{F}(\mathbf{x})}{d\mathbf{x}} = \begin{pmatrix} 0 & 1/m \\ -\partial^2 V/\partial q^2 & 0 \end{pmatrix} \equiv \mathcal{L}. \tag{3.10}$$

If the term $\mathcal{L}\delta\mathbf{x}$ is much larger than the remaining terms in the expansion (3.9) (which will be the case when the perturbation's position component, δq, is much smaller than the characteristic length scale of potential variations in the system or when $\partial V/\partial q$ is a linear or constant function of q), then we can approximate the perturbation dynamics by the linear expression

$$\frac{d(\delta\mathbf{x})}{dt} = \mathcal{L}\delta\mathbf{x}. \tag{3.11}$$

For the DQO we readily find

$$\mathcal{L} = \begin{pmatrix} 0 & 1/m \\ -12bq^2 & 0 \end{pmatrix}, \tag{3.12}$$

and the linearization is valid for $\delta q \ll 1$.

3.1.2 The Poincaré Section

If we were to plot even a single numerically calculated chaotic trajectory for the DQO on the (q,p) plane the result would look something like a plate of spaghetti.

Instead, a common technique to obtain information about the various regions (chaotic or not) of the classical phase space is to plot the Poincaré surface of section. This technique can be understood in two equivalent ways for a one-dimensional time-periodic Hamiltonian such as (3.1). We can imagine numerically propagating a single trajectory and plotting its position on the (q, p) plane only once per period of the driving force T, *e.g.* at the times $t = 0, T, 2T, \ldots$ (this view leads to the name "stroboscopic plot"). Alternatively, note that because the Hamiltonian is periodic in time, we can "wrap around" the ξ coordinate of equation (3.7) and replace ξ by the angle-like $\xi' = \xi \bmod 2\pi$. We again propagate a trajectory but now plot its intersections with the "surface of section" $\xi' = 0$. Sampling the trajectory once per period of the driving force ensures that the phase space location of one plotted point depends only on the location (and not on the time) of the previous plotted point, *i.e.* it ensures that we can write

$$\mathbf{x}_{n+1} = \mathbf{M}(\mathbf{x}_n), \tag{3.13}$$

where $\mathbf{x}_n$ is the phase space coordinate vector of the trajectory at the nth flash of the "strobe" (or at the nth intersection with the surface of section) and $\mathbf{M}$ depends only on the Hamiltonian. Equation (3.13) defines a mathematical *mapping* from the phase space to itself, known as the Poincaré map. The map shares a number of important properties with the corresponding continuous time system. The map is *symplectic,* which means that the area (known as the *symplectic area*) enclosed by a contour in phase space remains constant when each point on the contour is evolved according to the map. In addition, a chaotic continuous system yields a chaotic Poincaré map: two initially close phase space points will separate exponentially with n under the action of the map $\mathbf{M}$.

Figure 3.1 displays a Poincaré section for the DQO Hamiltonian (3.1), using the parameter values listed in the previous section, and with thirteen trajectories plotted at several times $t = T, 2T, 3T, \ldots$. The trajectories began at the initial coordinates $q(0) = -2$, -1.8, -1.6, -1.4, -1.2, -1, -0.8, -0.6, -0.4, 0, 1.1, 1.2, and 1.3 and $p(0) = 0$. Twelve of the trajectories lie on separate closed curves which resemble

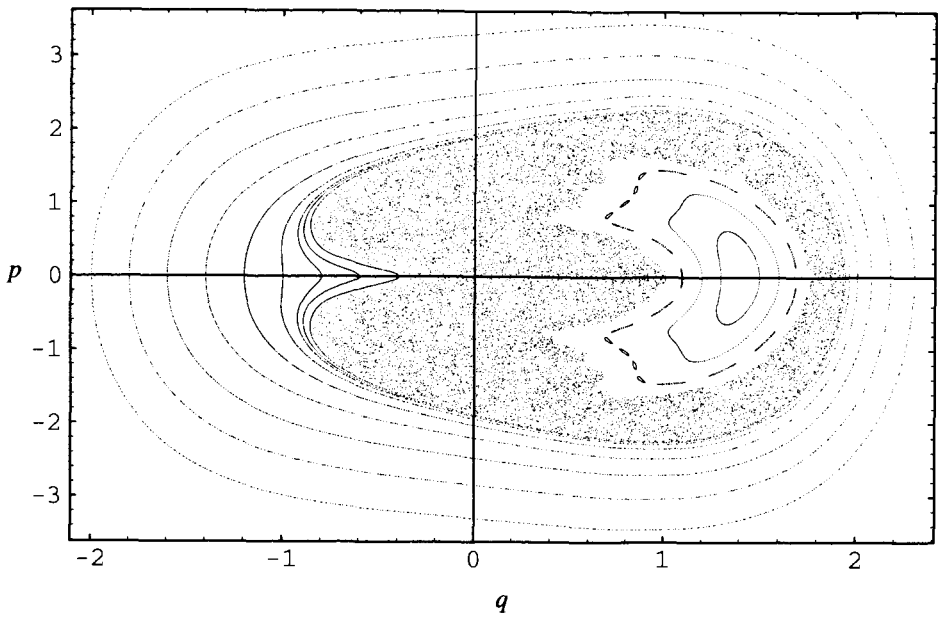

Figure 3.1: Poincaré section for thirteen trajectories of the DQO, using the parameter values given in section 3.1.1. Twelve trajectories lie on the closed regular curves, the other fills the chaotic zone uniformly. The regular and chaotic trajectories are plotted for 1000 and 10000 periods of the driving force, respectively.

the tori of integrable one-dimensional classical systems. The other trajectory, which began at $(q(0), p(0)) = (0, 0)$, fills a large region quite uniformly, a qualitative indication of chaos for trajectories within that part of phase space. Henceforth the speckled region in figure 3.1 will be referred to as the chaotic region or zone, and all other parts of phase space as non-chaotic or regular. The "regular island" is that regular region embedded within the chaotic zone. The Poincaré section indicates what appear to be quite sharply defined boundaries between chaotic and regular regions for this DQO. The well defined zones of the DQO will be an advantage when propagating classical ensembles and quantum wavepackets in that it will be possible to state that virtually all of the ensemble or packet is in either a chaotic or regular region.

Note the existence of a stable fixed point of the Poincaré map centred in the regular island at $(q, p) = (1.4, 0)$. This indicates a stable period T orbit for the continuous system. In addition, periodic orbits of various periods are expected to densely dot the chaotic zone. They are not visible in the Poincaré section because

they are all unstable and occupy a total phase space volume of zero.

3.1.3 Lyapunov Exponents

An important means for quantifying the sensitive dependence on initial conditions which characterizes chaos is the calculation of Lyapunov exponents. An intuitive way of defining the exponents is to consider one particular fiducial phase space trajectory, $\mathbf{x}_{\mathrm{f}}(t)$, and a perturbed trajectory, $\mathbf{x}_{\mathrm{p}}(t)$. If the separation between the two trajectories, $d(t)$, grows exponentially with time, *i.e.*

$$d(t) \equiv |\mathbf{x}_{\mathrm{p}}(t) - \mathbf{x}_{\mathrm{f}}(t)| = d(0)e^{\lambda t}, \tag{3.14}$$

in the limit of infinitesimal initial separation $d(0)$ and infinite final time, then the system has Lyapunov exponent λ. The exponent can be written explicitly as

$$\lambda = \lim_{t\to\infty} \lim_{d(0)\to 0} \frac{1}{t} \ln \left[\frac{d(t)}{d(0)}\right]. \tag{3.15}$$

The requirement of infinitesimal $d(0)$ is necessary to keep the perturbation within the linear regime and avoid the saturation in the growth of $d(t)$ at the system size. In a bounded system, trajectories with a positive Lyapunov exponent are, by definition, called chaotic. Note that the phase space separation (in one dimension, $d(t) = [(q_{\mathrm{p}}(t) - q_{\mathrm{f}}(t))^2 + (p_{\mathrm{p}}(t) - p_{\mathrm{f}}(t))^2]^{1/2}$) is not physically meaningful since the position and momentum coordinates have different units. However, a particular choice of units will allow the calculation of numerical values for $d(t)$, and the Lyapunov exponent calculated from (3.15) will behave like an ordinary physical quantity with units of inverse time [28].

In general for an N-dimensional phase space there will be N distinct Lyapunov exponents for each set of initial coordinates, each exponent corresponding to some particular direction for the initial perturbation vector $\mathbf{x}_{\mathrm{p}}(0) - \mathbf{x}_{\mathrm{f}}(0)$. However, if the initial perturbation is chosen randomly, it is almost certain to contain a component along the direction corresponding to the largest Lyapunov exponent. This component will eventually grow to dominate all others, so that the expression (3.15) will give

the largest exponent. The one-dimensional DQO will have a pair of exponents $\pm\lambda$ because of the area-preserving nature of Hamiltonian systems, so it will be sufficient to refer to *the* Lyapunov exponent given by (3.15) (a third trivial exponent of value zero will arise if we consider the extended autonomous phase space (q, p, ξ)). Note that the Lyapunov exponents are not to be confused with the eigenvalues of the linear perturbation evolution matrix $\mathcal{L}$ given in equation (3.12). The eigenvalues of $\mathcal{L}$ are $\pm\left[-12bq^2(t)/m\right]^{1/2}$, which are pure imaginary regardless of the phase space region in which the trajectory lies, whereas the Lyapunov exponent can be positive, as we will see below. The eigenvalues determine the *instantaneous* evolution of a perturbation, while the Lyapunov exponents determine the long time evolution. A positive Lyapunov exponent does not require a positive real part to the eigenvalues [29].

In practice, attempting to calculate the Lyapunov exponent for chaotic trajectories directly from equation (3.15) would result in very poor convergence, because starting with even the smallest initial separation $d(0)$ the machine precision allows, the perturbation will rapidly saturate at the system size. A standard technique to avoid this problem in calculating the largest exponent is the *renormalization* method. Two initial points separated by a small perturbation are chosen and the trajectories propagated for some time τ, such that at the final time the linearization of the perturbation dynamics is still valid. Then the perturbation vector is renormalized to its initial length (without altering its direction), propagated again for time τ, and the process repeated many times. The Lyapunov exponent is then given approximately by

$$\lambda_l = \frac{1}{l\tau}\sum_{j=1}^{l} \ln\left[\frac{d_j}{d(0)}\right], \tag{3.16}$$

where d_j is the length of the perturbation vector just before the jth renormalization and l is the (very large) number of renormalization steps. The idea of this technique is to take advantage of the linear perturbation dynamics and effectively start with a perturbation with the extremely small length $d(0)\prod_{j=1}^{l-1}(d(0)/d_j)$.

Figure 3.2 displays Lyapunov exponents for the DQO calculated using the renor-

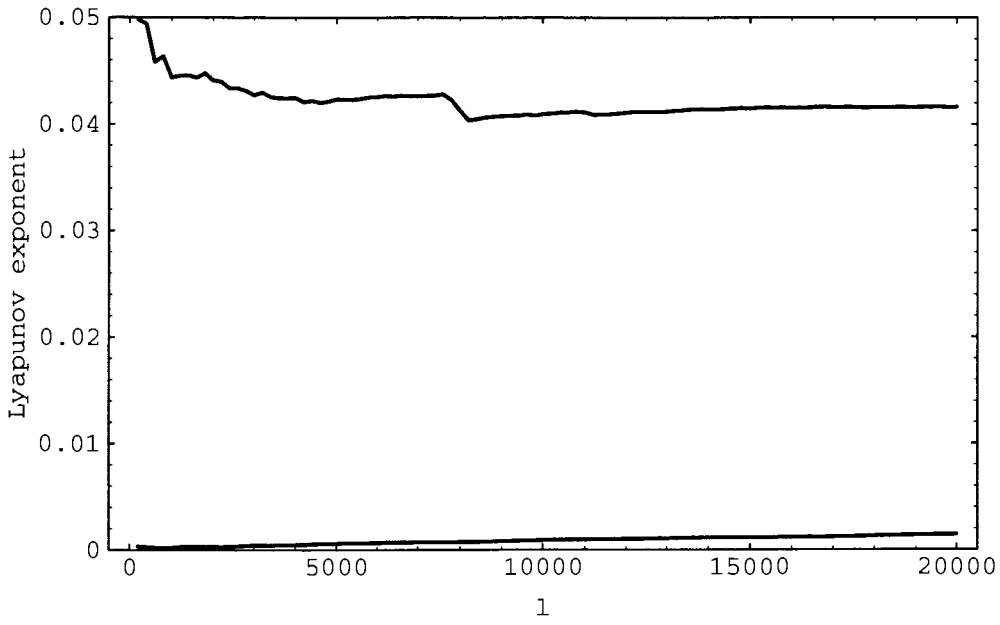

Figure 3.2: Lyapunov exponents for the DQO plotted versus renormalization step number l and using step size $\tau = 10T$. The upper and lower curves are for trajectories within the chaotic and regular regions, respectively.

malization technique and plotted versus l, with $d(0) = 1.4 \times 10^{-7}$ and $\tau = 10T$. The trajectories used for the upper curve began within the chaotic zone at $(q(0), p(0)) = (-0.7, -1)$ and the Lyapunov exponent appears to converge to a value $\lambda \simeq 0.042$. The lower curve is for trajectories beginning at $(q(0), p(0)) = (1, 1.1)$ within the regular island and indicates a value near zero for the exponent. The upper curve was typical for trajectories within the chaotic region, whereas in the regular island the exponents were found to take positive values (always much less than the chaotic zone value of 0.042) which increased as the zone boundary was approached. This is probably indicative of a small fraction of chaotic "froth" embedded in the regular island, and which becomes denser closer to the zone boundary. Nevertheless, it is still possible to make a sharp practical distinction between the behaviour in the chaotic and regular zones.

3.2 Evolution of Phase Space Distributions

3.2.1 The Distribution Functions

Wigner distribution

The phase space approach of the previous section emphasizes the usefulness of representing a quantum state function of a classically chaotic system in phase space. The most common technique for doing this is the calculation of the Wigner distribution function. To better understand the limitations of the Wigner method it will be helpful to present an attempt at a "derivation" of a quantum mechanical joint probability distribution function for position and conjugate momentum.

First, to illustrate the idea, consider a calculation of the momentum probability distribution $\rho(p)$ for a pure state $|\Psi\rangle$ [30]. For simplicity I treat a one-dimensional system with classical position and momentum q and p represented by the operators Q and P. Generalization to higher dimensions is straightforward. Consider the calculation of the expectation value in the state $|\Psi\rangle$ of the operator $e^{-iPq/\hbar}$. The distribution $\rho(p)$ must satisfy

$$\langle\Psi|e^{-iPq/\hbar}|\Psi\rangle = \int e^{-ipq/\hbar}\rho(p)\,dp. \tag{3.17}$$

Thus we can solve for $\rho(p)$ by taking the inverse Fourier transform, giving

$$\begin{aligned}
\rho(p) &= \frac{1}{2\pi\hbar}\int e^{ipq/\hbar}\langle\Psi|e^{-iPq/\hbar}|\Psi\rangle\,dq && (3.18)\\
&= \frac{1}{2\pi\hbar}\iint e^{ipq/\hbar}\langle\Psi|e^{-iPq/\hbar}|p'\rangle\langle p'|\Psi\rangle\,dq\,dp' && (3.19)\\
&= \frac{1}{2\pi\hbar}\iint e^{ipq/\hbar}e^{-ip'q/\hbar}\langle\Psi|p'\rangle\langle p'|\Psi\rangle\,dq\,dp' && (3.20)\\
&= \int \delta(p'-p)\langle\Psi|p'\rangle\langle p'|\Psi\rangle\,dp' && (3.21)\\
&= |\langle p|\Psi\rangle|^2 && (3.22)
\end{aligned}$$

as expected.

Now, by a completely analogous calculation, let us attempt to find an expression for a joint probability distribution function $\rho(q,p)$ for the state $|\Psi\rangle$. Considering the

expectation value of $e^{-iPq'/\hbar+ip'Q/\hbar}$, the distribution $\rho(q,p)$ should satisfy

$$\langle\Psi|e^{-iPq'/\hbar+ip'Q/\hbar}|\Psi\rangle = \iint e^{-ipq'/\hbar+p'q/\hbar}\rho(q,p)\,dq\,dp. \tag{3.23}$$

Taking the inverse Fourier transform and proceeding as above,

$$\begin{aligned}
\rho(q,p) &= \frac{1}{(2\pi\hbar)^2}\iint e^{ipq'/\hbar-ip'q/\hbar}\langle\Psi|e^{-iPq'/\hbar}e^{ip'Q/\hbar}e^{ip'q'/2\hbar}|\Psi\rangle\,dq'\,dp' && (3.24)\\
&= \frac{1}{(2\pi\hbar)^2}\iiint e^{ipq'/\hbar-ip'q/\hbar+ip'q'/2\hbar} \\
&\quad \times\langle\Psi|e^{-iPq'/\hbar}e^{ip'Q/\hbar}|q''\rangle\langle q''|\Psi\rangle\,dq'\,dp'\,dq'' && (3.25)\\
&= \frac{1}{(2\pi\hbar)^2}\iiint e^{ipq'/\hbar-ip'q/\hbar+ip'q'/2\hbar+ip'q''/\hbar} \\
&\quad \times\langle\Psi|e^{-iPq'/\hbar}|q''\rangle\langle q''|\Psi\rangle\,dq'\,dp'\,dq'' && (3.26)\\
&= \frac{1}{2\pi\hbar}\iint e^{ipq'/\hbar}\delta(q''-q+q'/2)\langle\Psi|q''+q'\rangle\langle q''|\Psi\rangle\,dq'\,dq'' && (3.27)\\
&= \frac{1}{2\pi\hbar}\int e^{ipq'/\hbar}\langle q-q'/2|\Psi\rangle\langle\Psi|q+q'/2\rangle\,dq'. && (3.28)
\end{aligned}$$

Here the operator identity (A.4) from Appendix A and the relation

$$e^{-iPq'/\hbar}|q\rangle = |q+q'\rangle \tag{3.29}$$

have been used. Expression (3.28) is the Wigner distribution $\rho_{\rm W}(q,p)$ which was introduced by E. Wigner in 1932 [31]. Notice that the expression can be inverted: knowing $\rho_{\rm W}(q,p)$ one can determine the state function to within an overall phase factor. The above calculation can be readily extended to systems described by a density matrix $\hat{\rho}$ with the result

$$\rho_{\rm W}(q,p) = \frac{1}{2\pi\hbar}\int e^{ipq'/\hbar}\langle q-q'/2|\hat{\rho}|q+q'/2\rangle\,dq'. \tag{3.30}$$

The difficulty in calling the Wigner distribution a true joint probability distribution is apparent from the first step, equation (3.23). There I chose the correspondence rule

$$e^{-ipq'/\hbar+p'q/\hbar} \longleftrightarrow e^{-iPq'/\hbar+ip'Q/\hbar} \tag{3.31}$$

between the classical and operator quantities, which is known as Weyl's rule. However, a very large number of other possible rules exist, for example

$$e^{-ipq'/\hbar+p'q/\hbar} \longleftrightarrow e^{-iPq'/\hbar}e^{ip'Q/\hbar}, \tag{3.32}$$

each of which are "correct" in the sense that the operator expression unambiguously gives the classical expression with the replacements $Q \to q$ and $P \to p$, but each of which result in different final expressions for $\rho(q,p)$. Clearly the difficulty is due to the non-commutativity of Q and P, and did not arise in the above calculation of $\rho(p)$. This problem of non-uniqueness, plus the fact that the Wigner distribution generally has negative-valued regions, prevents us from calling $\rho_{\rm W}(q,p)$ the joint probability density for q and p. Nevertheless, recalling the comments in the Introduction, we of course cannot *expect* $\rho_{\rm W}(q,p)$ to behave classically. The behaviour of $\rho_{\rm W}(q,p)$ in the classical regime will be examined in section 3.4.

The Wigner distribution does still share a number of useful properties with the classical joint probability density, the Liouville density $\rho_{\rm L}(q,p)$. To illustrate these we need the definition of the Wigner equivalent of an operator $A(Q,P)$,

$$A_{\rm W}(q,p) = \int e^{ipq'/\hbar} \langle q - q'/2 | A(Q,P) | q + q'/2 \rangle \, dq'. \tag{3.33}$$

This definition can be shown to be equivalent to Weyl's correspondence rule connecting the classical function $A_{\rm W}(q,p)$ with the quantal $A(Q,P)$ [32]. The following properties follow readily from the above definitions [33]. First, $\rho_{\rm W}(q,p)$ integrates out to the correct position or momentum distributions,

$$\int \rho_{\rm W}(q,p)\, dp = \langle q | \hat{\rho} | q \rangle, \tag{3.34}$$

$$\int \rho_{\rm W}(q,p)\, dq = \langle p | \hat{\rho} | p \rangle. \tag{3.35}$$

In addition, the expectation of any operator $A(Q,P)$ is given by the phase space integral

$$\int A_{\rm W}(q,p) \rho_{\rm W}(q,p)\, dq\, dp = {\rm Tr}\,(\hat{\rho} A(Q,P)). \tag{3.36}$$

Finally, note that if the density matrix can be written as

$$\hat{\rho} = \sum_i w_i |\phi_i\rangle\langle\phi_i| \tag{3.37}$$

for some vectors $|\phi_i\rangle$ and real weights w_i, then the Wigner density can be written

$$\rho_{\rm W}(q,p) = \sum_i w_i \rho_{\rm W}^{(i)}(q,p) \tag{3.38}$$

where

$$\rho_{\mathrm{W}}^{(i)}(q,p) = \frac{1}{2\pi\hbar}\int e^{ipq'/\hbar}\langle q - q'/2|\phi_i\rangle\langle\phi_i|q + q'/2\rangle\, dq'. \tag{3.39}$$

One further property will be useful in later sections. We can readily replace an overlap between two arbitrary states vectors $|\Psi\rangle$ and $|\Psi'\rangle$ with the overlap between the corresponding Wigner densities, $\rho_{\mathrm{W}}(q,p)$ and $\rho'_{\mathrm{W}}(q,p)$. That is,

$$\begin{aligned}
&\iint \rho_{\mathrm{W}}(q,p)\rho'_{\mathrm{W}}(q,p)\, dq\, dp \\
&\quad = \frac{1}{(2\pi\hbar)^2}\iiiint e^{ipx/\hbar}e^{ipx'/\hbar}\langle q - x/2|\Psi\rangle\langle\Psi|q + x/2\rangle \\
&\qquad \times\langle q - x'/2|\Psi'\rangle\langle\Psi'|q + x'/2\rangle\, dx\, dx'\, dq\, dp \qquad (3.40)\\
&\quad = \frac{1}{2\pi\hbar}\iint \langle q - x/2|\Psi\rangle\langle\Psi|q + x/2\rangle\langle q + x/2|\Psi'\rangle\langle\Psi'|q - x/2\rangle\, dx\, dq \\
&\quad = \frac{1}{2\pi\hbar}|\langle\Psi|\Psi'\rangle|^2. \qquad (3.41)
\end{aligned}$$

A few simple examples of Wigner distributions will close this introduction to the Wigner method. First, note that for a position eigenstate, $|\Psi\rangle = |q'\rangle$, the expression (3.28) readily gives

$$\rho_{\mathrm{W}}(q,p) = \frac{1}{2\pi\hbar}\delta(q - q'), \tag{3.42}$$

and similarly for a momentum eigenstate, $|\Psi\rangle = |p'\rangle$, we have

$$\rho_{\mathrm{W}}(q,p) = \frac{1}{2\pi\hbar}\delta(p - p'). \tag{3.43}$$

These are also the distributions we would expect for a classical system with precisely defined position (momentum) but completely indeterminate momentum (position). For a plane wave superposition, $|\Psi\rangle = 2^{-1/2}\left(|p'\rangle + |-p'\rangle\right)$, we find

$$\rho_{\mathrm{W}}(q,p) = \frac{1}{2^{3/2}\pi\hbar}\left[\delta(p - p') + \delta(p + p') + 2\cos(2p'q/\hbar)\delta(p)\right]. \tag{3.44}$$

This distribution consists of an oscillitory density midway between the two "classical-like" delta function terms at $p = p'$ and $p = -p'$. When $\rho_{\mathrm{W}}(q,p)$ is integrated over momentum, the oscillatory part produces the required standing-wave interference pattern in the position probability distribution.

Now consider a coherent state, $|\Psi\rangle = |q', p'\rangle$, which is a Gaussian state with mean position q' and mean momentum p', *i.e.* in coordinate representation

$$\langle x|q', p'\rangle = \frac{1}{[2\pi(\Delta q)^2]^{1/4}} e^{ip'x/\hbar - (x-q')^2/(2\Delta q)^2}, \tag{3.45}$$

where Δq is the position standard deviation. For this state expression (3.28) gives

$$\rho_{\rm W}(q,p) = \frac{1}{\pi\hbar} e^{-(q-q')^2/[2(\Delta q)^2]} e^{-(p-p')^2/[2(\Delta p)^2]} \equiv \rho_{(q',p')}(q,p), \tag{3.46}$$

where $\Delta p = \hbar/(2\Delta q)$ is the momentum standard deviation. That is, as we might have expected, the Wigner distribution $\rho_{(q',p')}(q,p)$ for a coherent state $|q', p'\rangle$ is just a product of Gaussians in position and momentum. As a final example consider a superposition of two spatially separated coherent states, $|\Psi\rangle = 2^{-1/2}\left(|a,0\rangle + i|-a,0\rangle\right)$. A straightforward calculation [33] gives

$$\begin{aligned} \rho_{\rm W}(q,p) \;=\; & \frac{1}{2\pi\hbar} e^{-p^2/[2(\Delta p)^2]} \Big[e^{-(q-a)^2/[2(\Delta q)^2]} \\ & + e^{-(q+a)^2/[2(\Delta q)^2]} + 2\cos(2pa/\hbar) e^{-q^2/[2(\Delta q)^2]} \Big]. \end{aligned} \tag{3.47}$$

Again we find two "classical-like" parts of the distribution, Gaussian in position and momentum, and centred at the points $(q,p) = (\pm a, 0)$, with a region oscillatory in p midway between them.

Husimi distribution

Another popular phase space representation of quantum mechanics was introduced by Husimi in 1940 [34]. The Husimi distribution $\rho_{\rm H}(q,p)$ can be defined as the Wigner distribution smoothed by the minimum uncertainty Gaussian function $\rho_{(q',p')}(q,p)$ defined in equation (3.46). That is,

$$\rho_{\rm H}(q,p) \;=\; \iint \rho_{\rm W}(q',p')\rho_{(q,p)}(q',p')\,dq'\,dp' \tag{3.48}$$

$$\;=\; \frac{1}{2\pi\hbar}|\langle q,p|\Psi\rangle|^2, \tag{3.49}$$

where the relation (3.41) has been used. Expression (3.49) gives us a simple alternative definition for the Husimi distribution and tells us that it is always non-negative.

The Husimi distribution shares the problem of non-uniqueness with the Wigner distribution. In the expression (3.45) for the coherent state $|q,p\rangle$, the position width Δq is free to take any positive value. In the limit $\Delta q \to 0$, we have $|q,p\rangle \to |q\rangle$ and thus $\rho_{\mathrm{H}}(q,p) \to |\langle q|\Psi\rangle|^2$, and conversely as $\Delta q \to \infty$ we have $\rho_{\mathrm{H}}(q,p) \to |\langle p|\Psi\rangle|^2$. Intermediate values of Δq thus represent a sort of "compromise" between the coordinate and momentum representations. Note also that equations analogous to (3.34) and (3.35) are not satisfied by $\rho_{\mathrm{H}}(q,p)$. Instead, the Husimi density integrates out to the Gaussian smoothed position and momentum distributions. The Husimi density does share property (3.38) with $\rho_{\mathrm{W}}(q,p)$, namely that the Husimi density of a mixture is the weighted sum of the Husimi densities of the elements of the mixture. The behaviour of $\rho_{\mathrm{H}}(q,p)$ in the classical regime will be discussed in section 3.4.

Considering the form of expression (3.49) for the Husimi density one might be tempted to interpret $\rho_{\mathrm{H}}(q,p)$ as a probability density for finding the particle in the coherent state $|q,p\rangle$, or for finding the particle within a "Gaussian-profiled region" about the phase space point (q,p). However, the coherent states are overcomplete, meaning that we cannot uniquely expand an arbitrary state in the $|q,p\rangle$, and preventing us from taking this interpretation. Nevertheless, the simplicity of expression (3.49) for $\rho_{\mathrm{H}}(q,p)$ does allow for some fairly intuitive interpretations of this density. Royer [35], in the process of describing a technique for measuring $\rho_{\mathrm{W}}(q,p)$, has presented an operational procedure for directly measuring $\rho_{\mathrm{H}}(q,p)$ for a quantum state which naturally generalizes a classical procedure to measure the Liouville density. In addition, note that we can write equation (3.49) explicitly in the coordinate representation as

$$\rho_{\mathrm{H}}(q,p) = \frac{1}{(2\pi)^{3/2}\hbar\Delta q}\left|\int e^{-ipx/\hbar-(x-q)^2/(2\Delta q)^2}\Psi(x)\,dx\right|^2. \tag{3.50}$$

Thus if we define a "reduced" wave function by

$$\Psi_q(x) \equiv \frac{1}{[2\pi(\Delta q)^2]^{1/4}}e^{-(x-q)^2/(2\Delta q)^2}\Psi(x) \tag{3.51}$$

we see that $\rho_{\mathrm{H}}(q,p)$ is just the momentum probability density of the reduced wave

function, *i.e.*

$$\rho_{\mathrm{H}}(q,p) = |\langle p|\Psi_q\rangle|^2. \tag{3.52}$$

In an experimental setup, the reduction of $|\Psi\rangle$ (not to be confused with a "collapse of the wave function") might be accomplished by some sort of filtering procedure, and once this has been done the problem of interpreting $\rho_{\mathrm{H}}(q,p)$ becomes equivalent to that of interpreting the conventional momentum probability density.

For examples of the Husimi distribution, imagine Gaussian smoothed versions of the Wigner densities presented above. The smoothing is guaranteed to be sufficient to completely remove the negative portions in the oscillatory regions.

Classical distributions

In order to illustrate their usefulness, the quantal phase space distributions introduced above will be directly compared with classical distributions in the next section, for evolving DQO states. The various mathematical properties (3.34, 3.35, 3.36, 3.38) that the Wigner density shares with the classical Liouville density $\rho_{\mathrm{L}}(q,p)$ suggest a comparison between these two distributions.

On the other hand the Husimi distribution, being a Gaussian smoothed version of $\rho_{\mathrm{W}}(q,p)$, suggests a comparison with a similarly Gaussian smoothed Liouville density,

$$\rho_{\mathrm{SL}}(q,p) \equiv \iint \rho_{\mathrm{L}}(q',p')\rho_{(q,p)}(q',p')\,dq'\,dp'. \tag{3.53}$$

It is worth emphasizing that these are only "suggested comparisons", not claims that a quantum state "is", in some sense, a classical distribution. The results of this chapter should help clarify this point.

3.2.2 Results for the DQO

In this section the results of a number of calculations of the various phase space distributions defined in the previous section will be presented for the DQO.

General remarks on the quantum calculations

The coordinate representation state function was propagated from the initial state using the technique described in section 2.2. The Hamiltonian used was the quantized version of the classical DQO Hamiltonian (3.1), namely

$$H = \frac{-\hbar^2}{2m}\frac{\partial^2}{\partial x^2} + bx^4 - a\cos(\omega t)x. \tag{3.54}$$

At several propagation times the Wigner and Husimi distributions were calculated from the state function using equations (3.28) and (3.49), respectively.

The initial quantum state for most calculations was chosen to be a coherent state, explicitly given by expression (3.45) in coordinate representation or (3.46) in Wigner representation. This initial state, being of minimum uncertainty, allowed the wave packet to be maximally localized in either the chaotic or regular regions of the classical phase space of figure 3.1. The system parameters m, b, a, and ω were always given the values presented for the classical calculations in section 3.1.1. The quantization of the DQO Hamiltonian introduced a new parameter, the size of $\hbar$ relative to typical actions. To vary the "classicality" of the system various numerical values of $\hbar$ were used (recalling that $\hbar$ is a physical constant, this amounted to changing units of position and momentum). A formula due to Weyl [3] (to be discussed in section 3.4.1) tells us that semiclassically we can "fit" one energy eigenstate into each phase space volume of $2\pi\hbar$, for a one-dimensional system. Thus the ratio of the volume of the accessible region (which is on the order of typical actions) to $2\pi\hbar$ gives an intuitive characterization of the degree of classicality.

A certain set of initial state and integration parameters was used frequently; these values will be referred to as the *standard* parameter values and are as follows. The initial state (at $t = 0$) was a Gaussian state with centroid $(\langle q\rangle, \langle p\rangle) = (0.2, 0)$ (for the *chaotic standard values*) or $(\langle q\rangle, \langle p\rangle) = (1, 1)$ (for the *non-chaotic standard values*) and deviations $\Delta q = \Delta p = 0.1$. Thus, referring to the Poincaré section (figure 3.1), the initial state was almost completely confined to the chaotic zone or regular island. The value $\hbar = 0.02$ was used, and with the chaotic zone and regular island together

occupying a phase space volume of $V_C = 10.1$, we obtain the ratio $V_C/(2\pi\hbar) = 80.4$, a quantitative indication of the degree of localization of the initial state. The standard calculations used $N = 4000$ spatial grid points.

The standard parameter calculations had the most stringent accuracy requirements, so this subsection will close with a discussion of the accuracy of these calculations. For the calculation of the state function the spatial boundaries were placed at $q = \pm 2.5$, and the values of the norm of the wave function at the boundaries did not exceed 1.0×10^{-7} during the propagation. The classical phase space plots to follow indicate a value for the largest momentum contributing to the state of $p_{\max} \simeq 2$, so that according to relation (2.9) at least $N \simeq 160$ spatial grid points were needed for the calculation of the wave function. This criterion is of course crude, and the calculated results were found to vary significantly with N until $N \simeq 2000$, prompting the choice of $N = 4000$ for the standard parameters. For the time integration an absolute tolerance value of 10^{-7} was used. The behaviour of the calculated values upon varying the tolerance was similar to that of the DHO test calculations of section 2.2.2, so that the time integration was considered sufficiently accurate, and the number of spatial grid points primarily controlled the accuracy. The normalization of the state was monitored; $\langle\Psi|\Psi\rangle$ remained within 1 part in 10^9 of unity during the calculations.

General remarks on the classical calculations

For the classical calculations, the classical Liouville density $\rho_L(q,p)$ was propagated from the initial state using the technique of section 2.1. The smoothed Liouville density $\rho_{SL}(q,p)$ was calculated from $\rho_L(q,p)$ at several propagation times using equation (3.53). The initial classical q and p distributions were chosen equal to the initial quantal q and p distributions, and no correlations between q and p were assumed. For an initial coherent state $|q',p'\rangle$ this meant choosing

$$\rho_L(q,p,t=0) = \rho_{(q',p')}(q,p). \tag{3.55}$$

Standard parameter values for the classical calculations will also be referred to; these constitute precisely the same initial state values as for the quantal standard values.

Wigner and Liouville distributions

Figure 3.3 presents grey scale plots of the Liouville density $\rho_{\mathrm{L}}(q,p)$ and the Wigner density $\rho_{\mathrm{W}}(q,p)$ at the times $t = T$, $2T$, $4T$, $6T$, $8T$, $12T$, $20T$, and $40T$, where T is the period of the driving force. The chaotic standard parameter values were used. For the classical plots, black corresponds to $\rho_{\mathrm{L}} = 0$ and white to some maximum value of ρ_{L}. Because the Wigner density can become negative, a neutral grey was chosen for $\rho_{\mathrm{W}} = 0$, with black and white indicating extreme negative and positive values, respectively. The classical calculations used 200000 particles to simulate the Liouville density, sufficient to define even extremely fine structure.

The classical evolution in figure 3.3 clearly displays the stretching and folding of $\rho_{\mathrm{L}}(q,p)$ which is characteristic of chaotic dynamics. By $t = 20T$ the distribution begins to visibly approach a steady state, filling quite uniformly the chaotic zone (compare with figure 3.1). The quantal evolution appears to closely resemble the classical, but supplemented by patterns of oscillating fringes, which tend to dominate at longer times.

Husimi and smoothed Liouville distributions

Figure 3.4 presents a comparison of Husimi and smoothed Liouville distributions for the DQO at the times $t = T$, $2T$, $4T$, $6T$, $8T$, $12T$, $20T$, and $40T$. The calculations used the chaotic standard parameters. Here both the quantum and classical plots use the same grey scale, with black indicating a zero density value and white some maximum value. The Gaussian smoothing function used to generate these plots had standard deviations $\Delta q = \Delta p = 0.1$. Noting that both positions and momenta are confined to roughly the same range of numerical values, the smoothing function chosen would appear to produce a good "compromise" between displaying position and momentum information. It was sufficient to use only 50000 particles for the

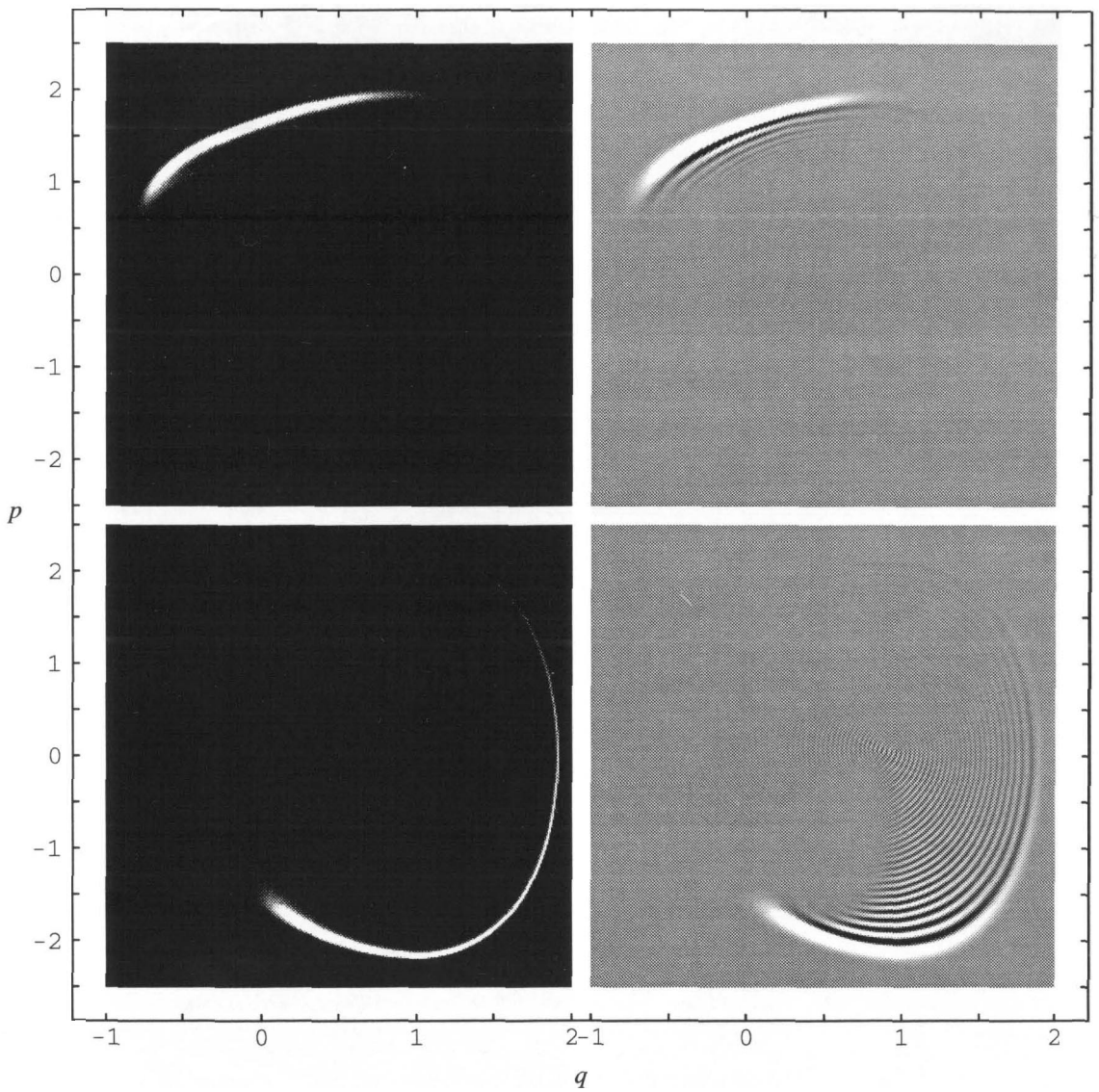

Figure 3.3: Liouville density (left column) and Wigner density (right column) for the DQO with the chaotic standard parameters (Gaussian initial states at $(\langle q\rangle, \langle p\rangle) = (0.2, 0)$). On this page the states at $t = T$ (top) and $t = 2T$ (bottom) are displayed. For the classical plots, black and white correspond to zero and a maximum density value, whereas for the quantum plots black, neutral grey, and white correspond to extreme negative, zero, and extreme positive values, respectively.

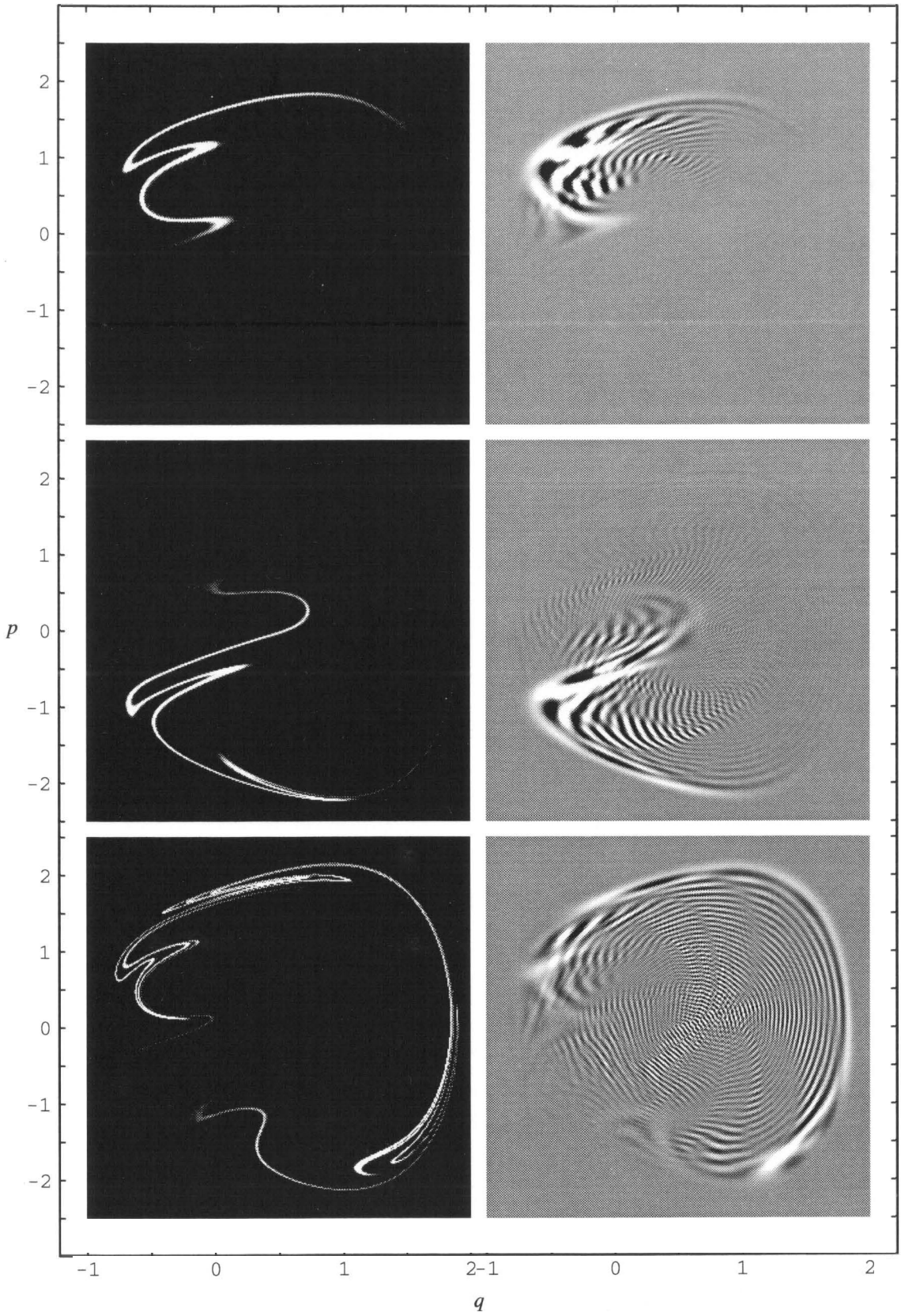

Figure 3.3: (continued) ρ_{L} (left) and ρ_{W} (right) at $t = 4T$, $6T$, and $8T$, top to bottom.

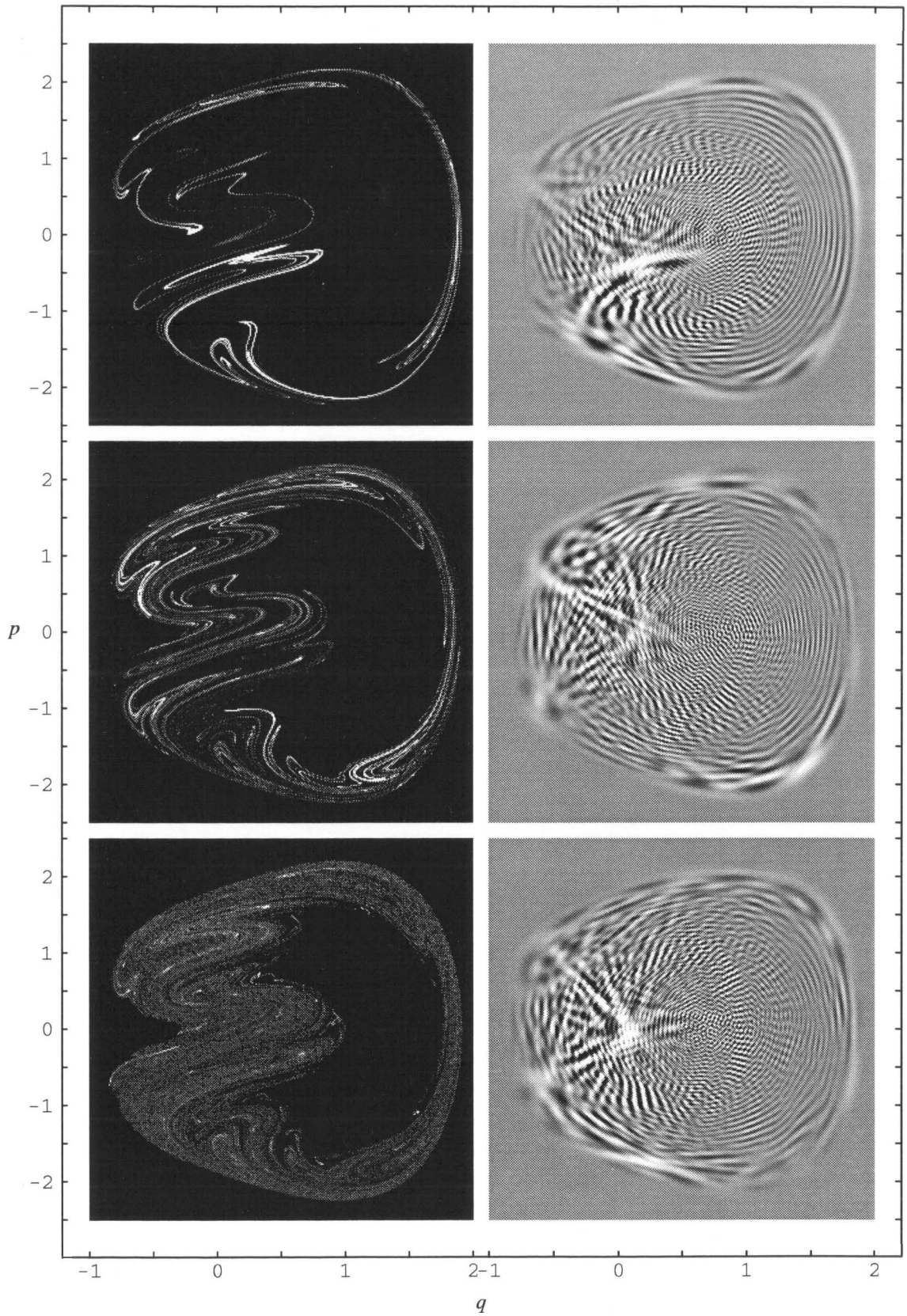

Figure 3.3: (continued) ρ_{L} (left) and ρ_{W} (right) at $t = 12T$, $20T$, and $40T$, top to bottom.

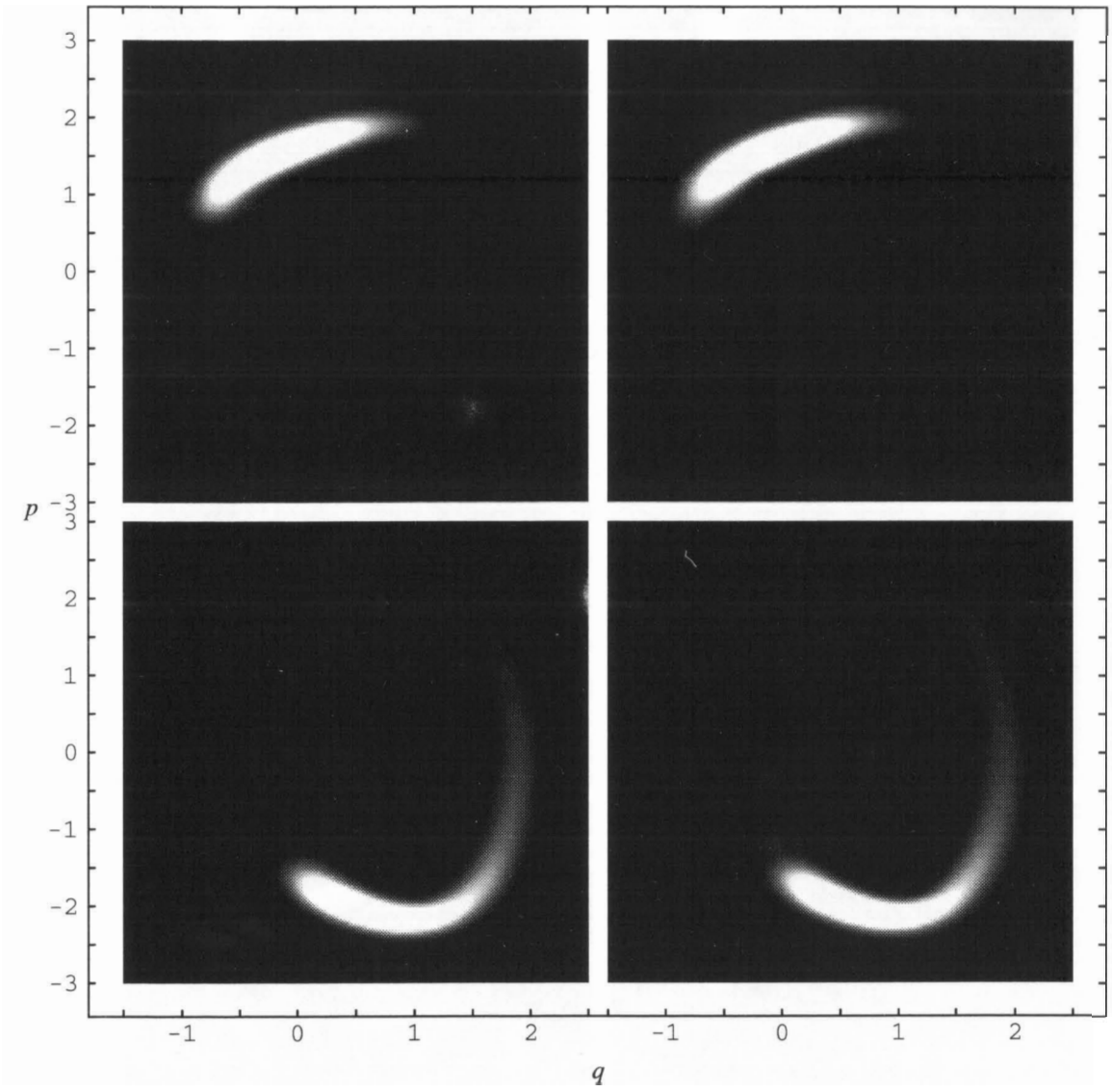

Figure 3.4: Smoothed Liouville density (left column) and Husimi density (right column) for the DQO with the chaotic standard parameters. On this page the states at $t = T$ (top) and $t = 2T$ (bottom) are displayed. Both classical and quantum plots share the same grey scale, black and white corresponding to zero and a maximum density value, respectively.

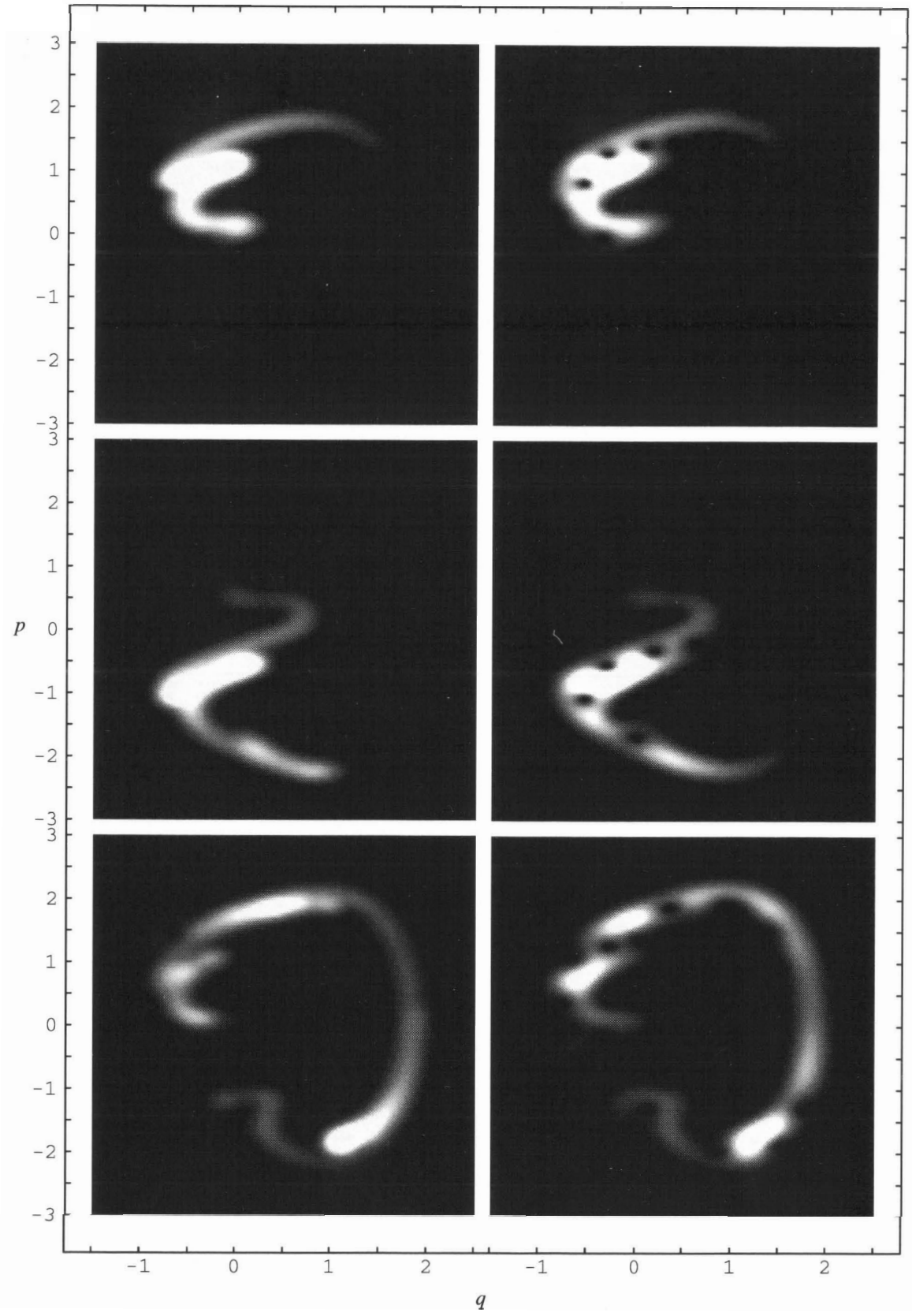

Figure 3.4: (continued) ρ_{SL} (left) and ρ_{H} (right) at $t = 4T$, $6T$, and $8T$, top to bottom.

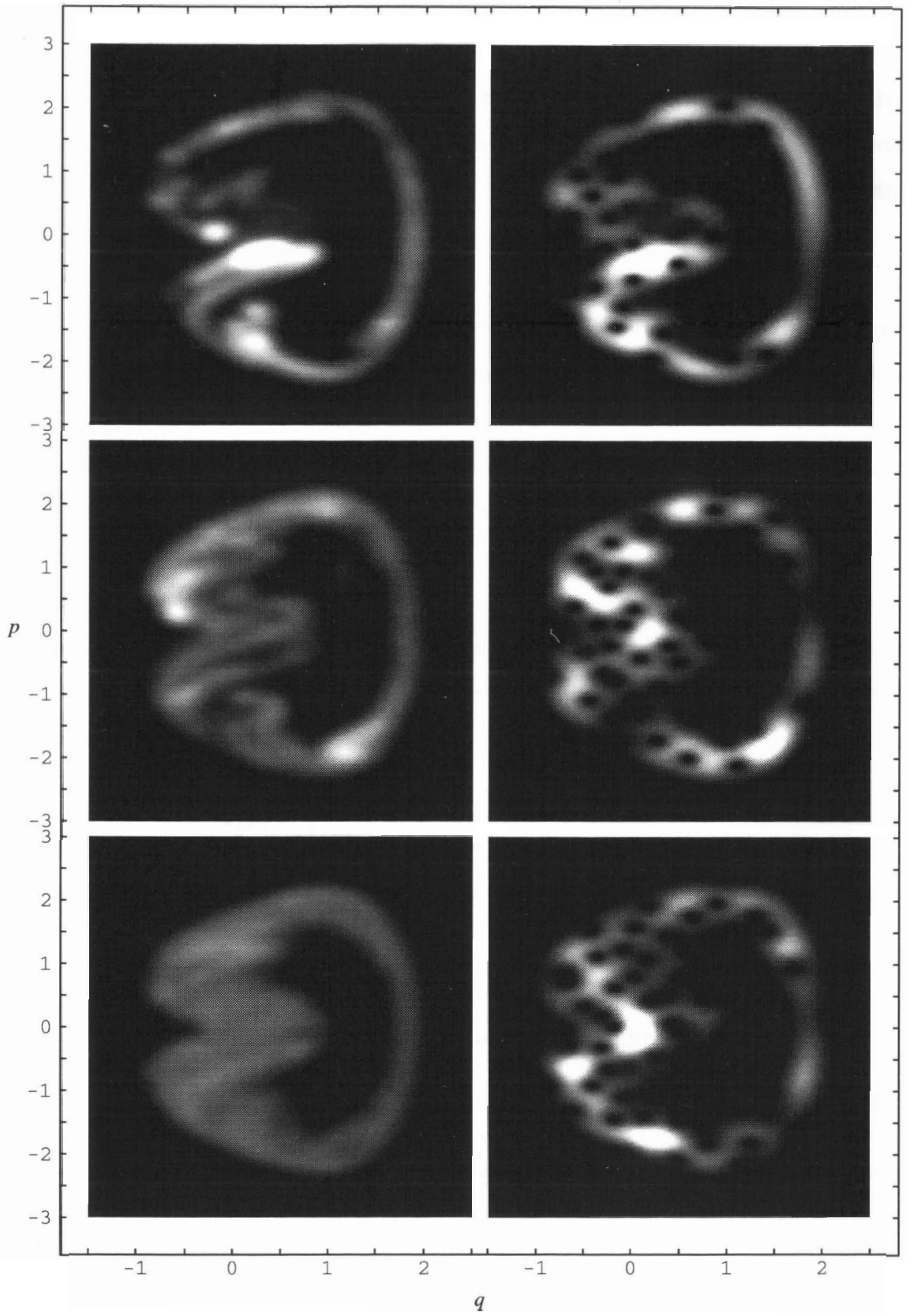

Figure 3.4: (continued) ρ_{SL} (left) and ρ_{H} (right) at $t = 12T$, $20T$, and $40T$, top to bottom.

classical calculations here.

The smoothed Liouville plots appear to be just that: smoothed versions of the classical plots in figure 3.3. However, the Husimi plots are remarkably different from the Wigner plots. The oscillating fringes have almost completely disappeared, leaving a density that very closely resembles the smoothed Liouville density.

Figure 3.5 presents Husimi and smoothed Liouville distributions for the non-chaotic standard parameters at the times $t = T$, $2T$, $6T$, $18T$, and $40T$. Both quantum and classical plots use the same grey scale, and the smoothing function had $\Delta q = \Delta p = 0.1$. The classical calculations used 50000 particles. It appears that the state remains confined to the regular island and spreads only very slowly. The quantal and classical densities appear very similar until at least $t = 40T$, with an almost complete lack of interference in $\rho_{\mathrm{H}}(q,p)$.

One might suspect that the close agreement between $\rho_{\mathrm{SL}}(q,p)$ and $\rho_{\mathrm{H}}(q,p)$ in figures 3.4 and 3.5 is due to the special nature of the initial Gaussian states. To test this, the above calculations were repeated for an initial quantum state which was a box in momentum space,

$$\Psi(p) = \begin{cases} (2p_{\mathrm{m}})^{-1/2} e^{-ipx_0/\hbar} & \text{for } |p| \leq p_{\mathrm{m}} \\ 0 & \text{for } |p| > p_{\mathrm{m}}, \end{cases} \tag{3.56}$$

and therefore in coordinate representation

$$\Psi(x) = \left(\frac{\hbar}{\pi p_{\mathrm{m}}}\right)^{1/2} \frac{\sin\left[p_{\mathrm{m}}(x - x_0)/\hbar\right]}{x - x_0}. \tag{3.57}$$

The initial classical distribution was chosen to be the uncorrelated product

$$\rho_{\mathrm{L}}(q,p,t=0) = |\Psi(x)|^2 |\Psi(p)|^2. \tag{3.58}$$

The values $x_0 = 0.2$ and $p_{\mathrm{m}} = 0.5$ were used. The quantum calculations used $N = 2000$ grid points and the classical calculations 50000 particles. Figure 3.6 presents the smoothed Liouville and Husimi distributions at the times $t = T$ and $t = 4T$, using the box momentum initial state. Comparing with figure 3.4 for the Gaussian initial states, we see new structure in these plots, although the new structure

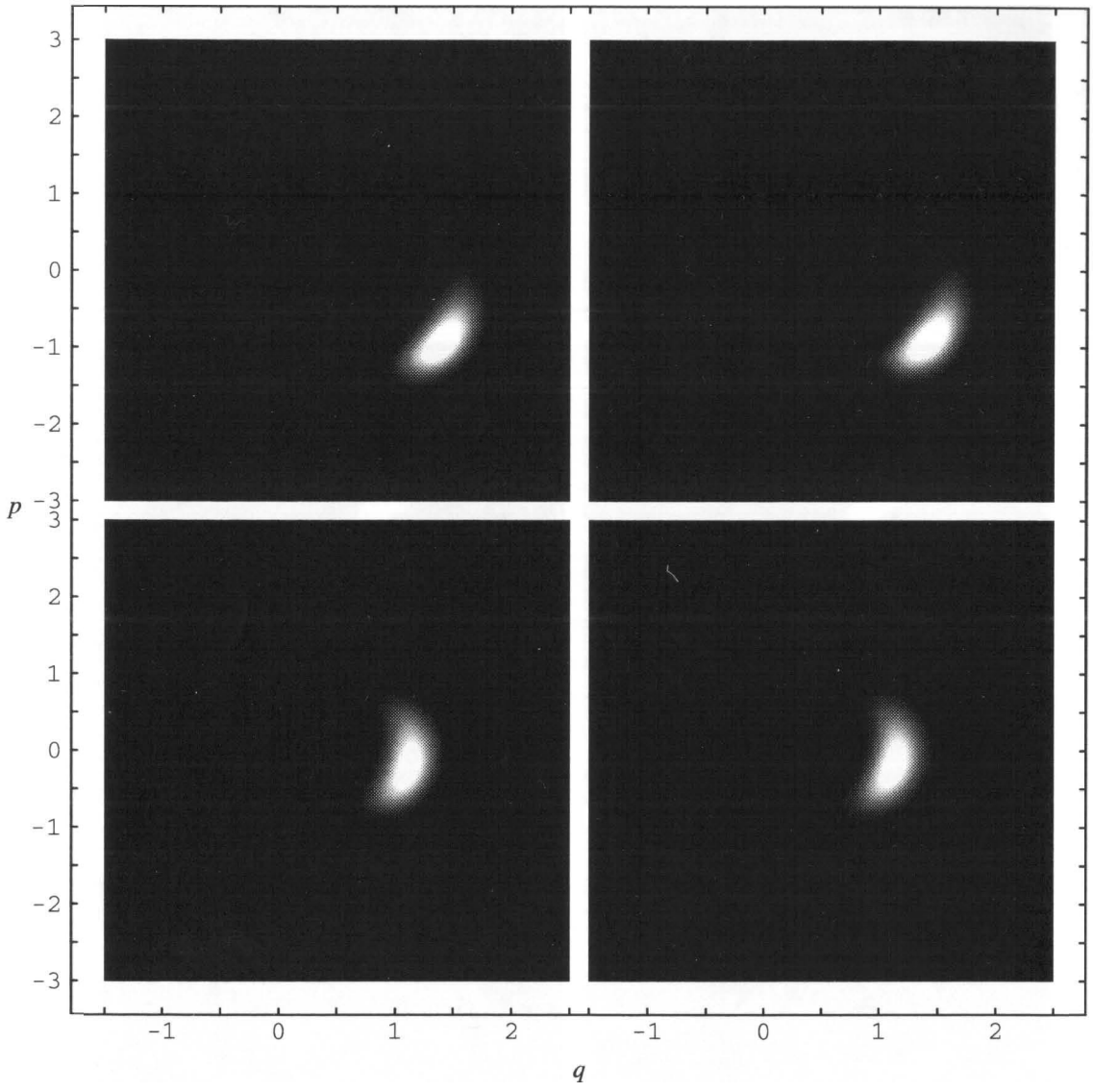

Figure 3.5: Smoothed Liouville density (left column) and Husimi density (right column) for the DQO with the non-chaotic standard parameters. On this page the states at $t = T$ (top) and $t = 2T$ (bottom) are displayed. Both classical and quantum plots share the same grey scale, black and white corresponding to zero and a maximum density value, respectively.

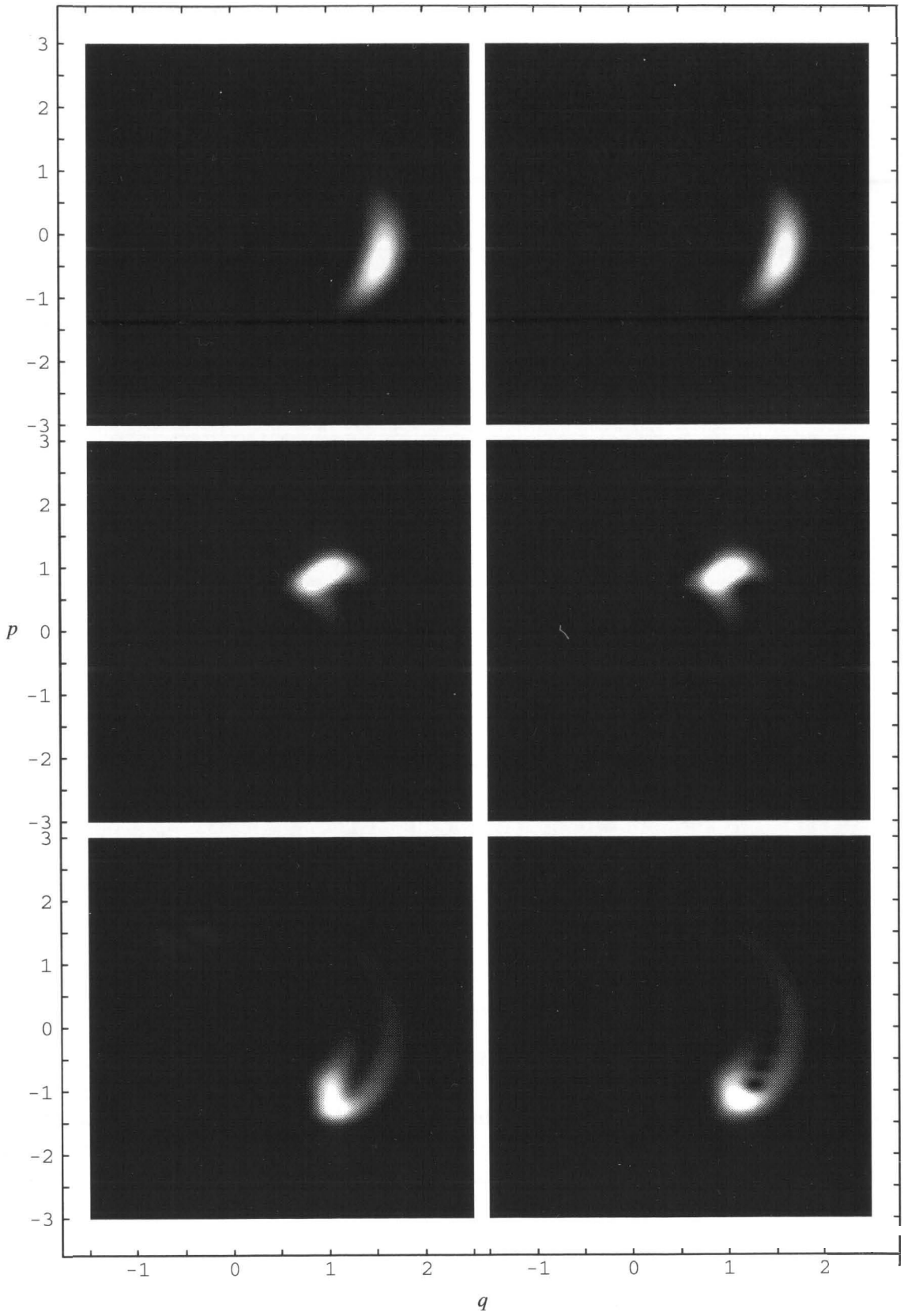

Figure 3.5: (continued) ρ_{SL} (left) and ρ_{H} (right) at $t = 6T$, $18T$, and $40T$, top to bottom.

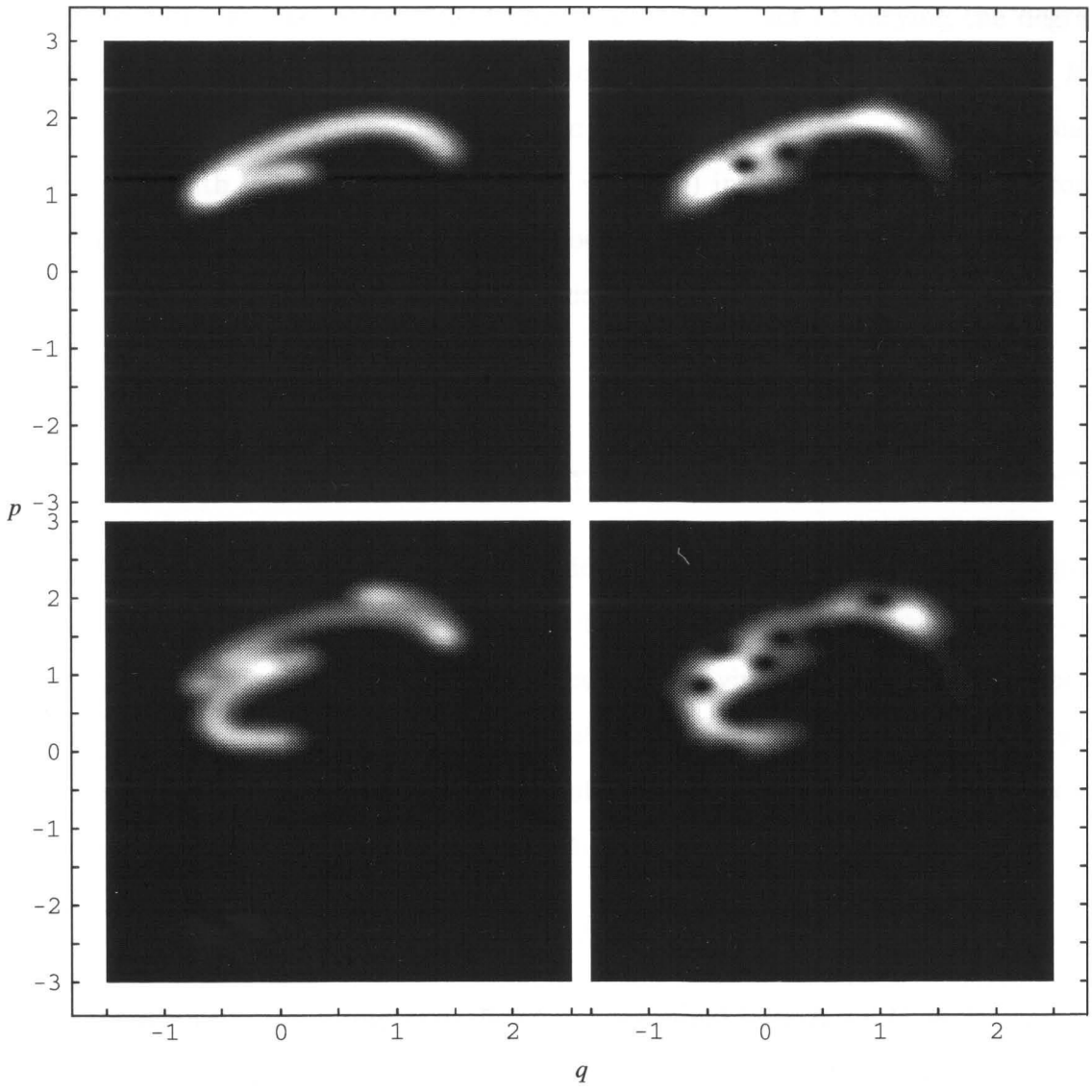

Figure 3.6: Smoothed Liouville density (left column) and Husimi density (right column) for the DQO with the box momentum initial state. The states at $t = T$ (top) and $t = 4T$ (bottom) are displayed. Both classical and quantum plots share the same grey scale, black and white corresponding to zero and a maximum density value, respectively.

is apparent in both $\rho_{\mathrm{SL}}(q,p)$ and $\rho_{\mathrm{H}}(q,p)$, and the degree of agreement between $\rho_{\mathrm{SL}}(q,p)$ and $\rho_{\mathrm{H}}(q,p)$ is comparable for the two initial states.

To close this study of phase space distributions, a number of quantum calculations were made with various values of $\hbar$, to investigate the effect of varying the degree of classicality of the system. Figure 3.7 presents Husimi distributions at $t = 8T$ for calculations using $\hbar = 0.16$, 0.08, 0.04, and 0.02. All calculations used Gaussian initial states, with initial centroid $(\langle q\rangle, \langle p\rangle) = (0.2, 0)$ in the chaotic zone. In order of decreasing $\hbar$, the initial states and the smoothing functions both used $\Delta q = \Delta p = 0.2\cdot 2^{1/2}$, 0.2, $0.1\cdot 2^{1/2}$, and 0.1. The plots indicate a convergence towards the classical result of figure 3.3 as $\hbar$ is decreased.

3.3 Expectation Values and Ehrenfest's Theorem

Ehrenfest's theorem provides a route by which a quantum state can be represented in phase space (by taking the expectations $(\langle q\rangle, \langle p\rangle)$), and this approach can, under certain circumstances, yield single trajectories evolving according to Hamilton's equations (2.1) and (2.2) in the classical limit. The theorem may be readily derived beginning with the expression for the time rate of change of the expectation value of any time-independent observable R in an arbitrary quantum state [36],

$$\frac{d\langle R\rangle}{dt} = \frac{i}{\hbar}\langle [H, R]\rangle. \tag{3.59}$$

Taking the quantum Hamiltonian in the one-dimensional form $H(Q,P) = P^2/(2m) + V(Q)$ gives

$$\frac{d\langle Q\rangle}{dt} = \frac{\langle P\rangle}{m}, \tag{3.60}$$

$$\frac{d\langle P\rangle}{dt} = \left\langle \frac{-\partial V(Q)}{\partial Q} \right\rangle. \tag{3.61}$$

The last equation can be approximated by

$$\frac{d\langle P\rangle}{dt} = \frac{-\partial V(\langle Q\rangle)}{\partial \langle Q\rangle} \tag{3.62}$$

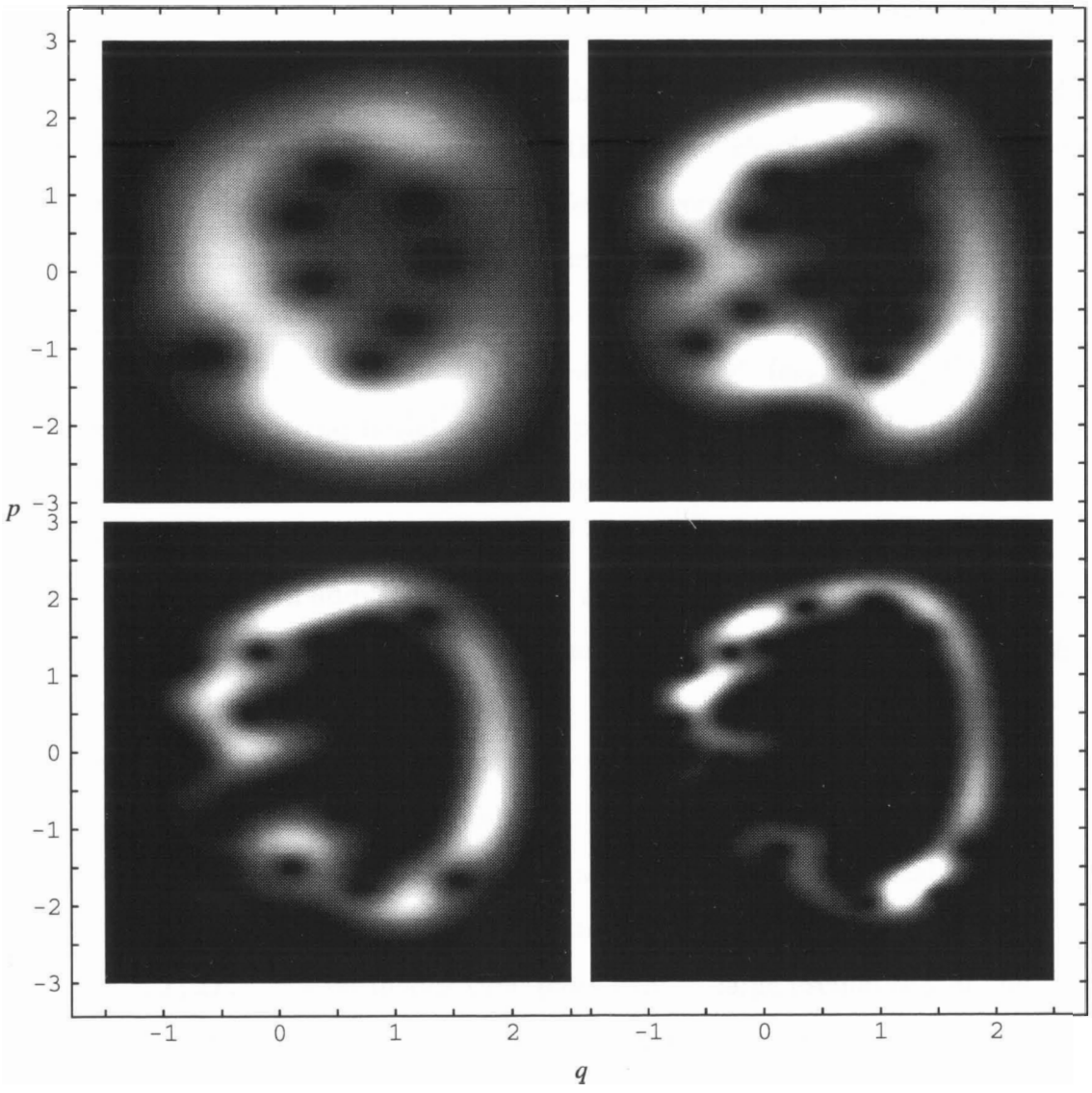

Figure 3.7: Husimi density for the DQO at $t = 8T$ but at various degrees of classicality. Left to right and top to bottom, the plots are for $\hbar = 0.16$, 0.08, 0.04, and 0.02.

if the position standard deviation Δq is much smaller than the length scale of potential variations ((3.62) is exact if $\partial V/\partial Q$ is a linear (or constant) function of Q). Thus if it were always the case that Δq is negligibly small for quantum states in the classical limit, then, in this limit, the states' centroids would follow Hamilton's equations.

The results of the previous section, which indicate a much more rapid spread of DQO states in the classically chaotic case than in the classically non-chaotic case, suggest that the regime of validity of Ehrenfest's theorem may be considerably more restricted in the classically chaotic case. To investigate this possibility, the means $\langle q \rangle$ and $\langle p \rangle$ and the deviations Δq and Δp were calculated for evolving DQO quantum states. For each initial state the "Ehrenfest trajectory" $(q_{\rm Ehr}(t), p_{\rm Ehr}(t))$ was also calculated by evolving the initial centroid position according to Hamilton's equations, using the numerical technique described in section 2.1. Thus the validity of Ehrenfest's theorem would be indicated by the true centroid following closely the Ehrenfest trajectory. In addition, the means and deviations of evolving Liouville distributions were also calculated. Some of these results have been previously published by Ballentine, Yang, and Zibin [37].

Figure 3.8 presents a comparison of the quantal and classical centroids and deviations with the Ehrenfest trajectory, for initial states specified by the chaotic standard parameter values (quantal and classical) of section 3.2.2. The classical calculations used 200000 particles. Data points are plotted only in Poincaré section, *i.e.* at the times $t = 0, T, 2T, \ldots$. Continuous time plots exhibit large oscillations at the driving frequency, which distract from the essential features. The graphs indicate that Ehrenfest's theorem is valid until roughly $t = 5T$. After this time the centroids relax towards steady state values and the widths approach saturated maximum values, in agreement with the rapid approach to a uniform coverage of the chaotic zone indicated in the phase space distributions of figures 3.3 and 3.4. Note that the means and widths calculated from the classical Liouville distribution agree well with those calculated from the quantum state even long after Ehrenfest's theorem becomes in-

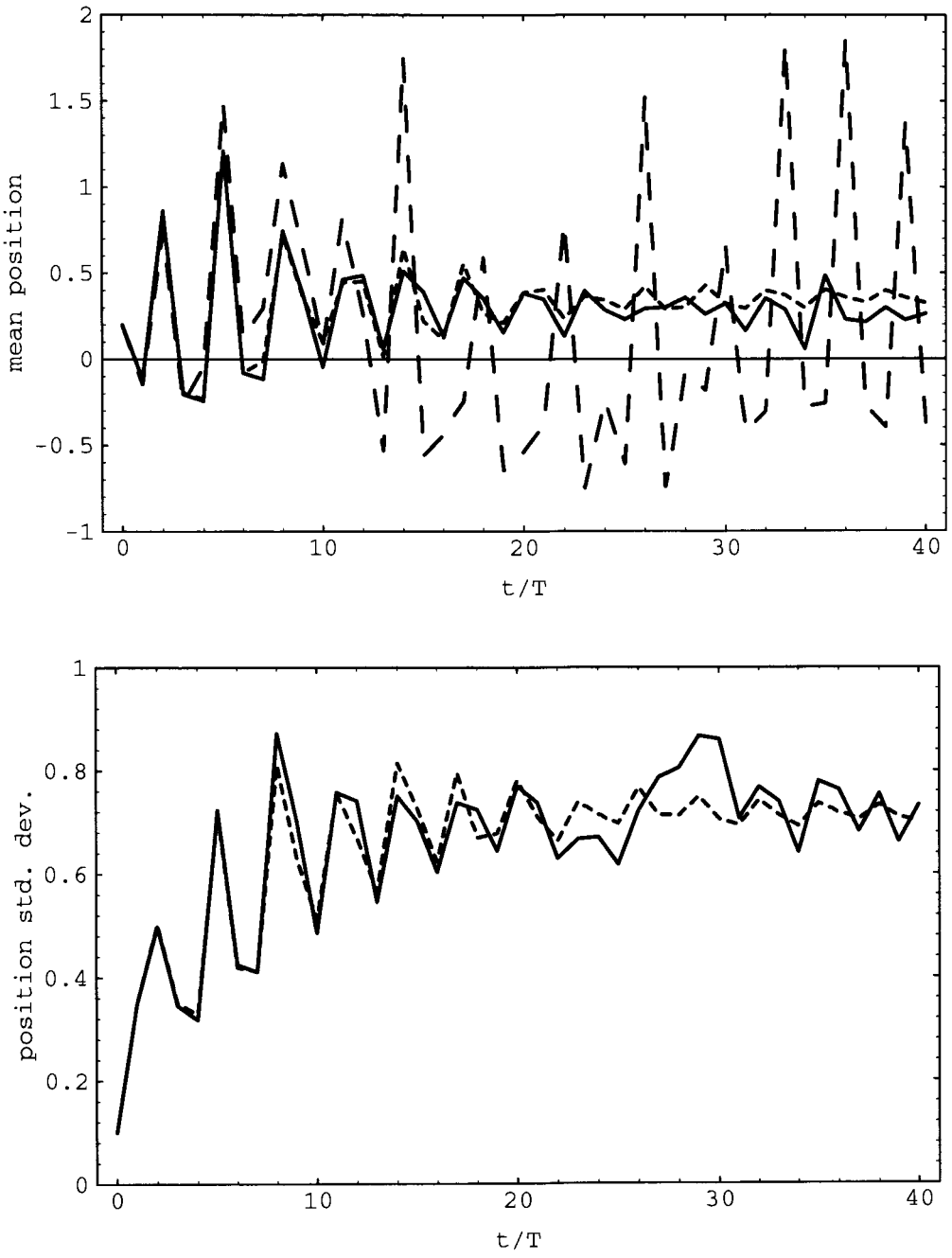

Figure 3.8: Mean position (top) and standard deviation in position (bottom) for DQO quantum state (solid line) and classical distribution (finely dashed line), plotted versus time in periods of the driving force, and using the chaotic standard parameters. The Ehrenfest trajectory (coarsely dashed line) is also indicated on the top graph.

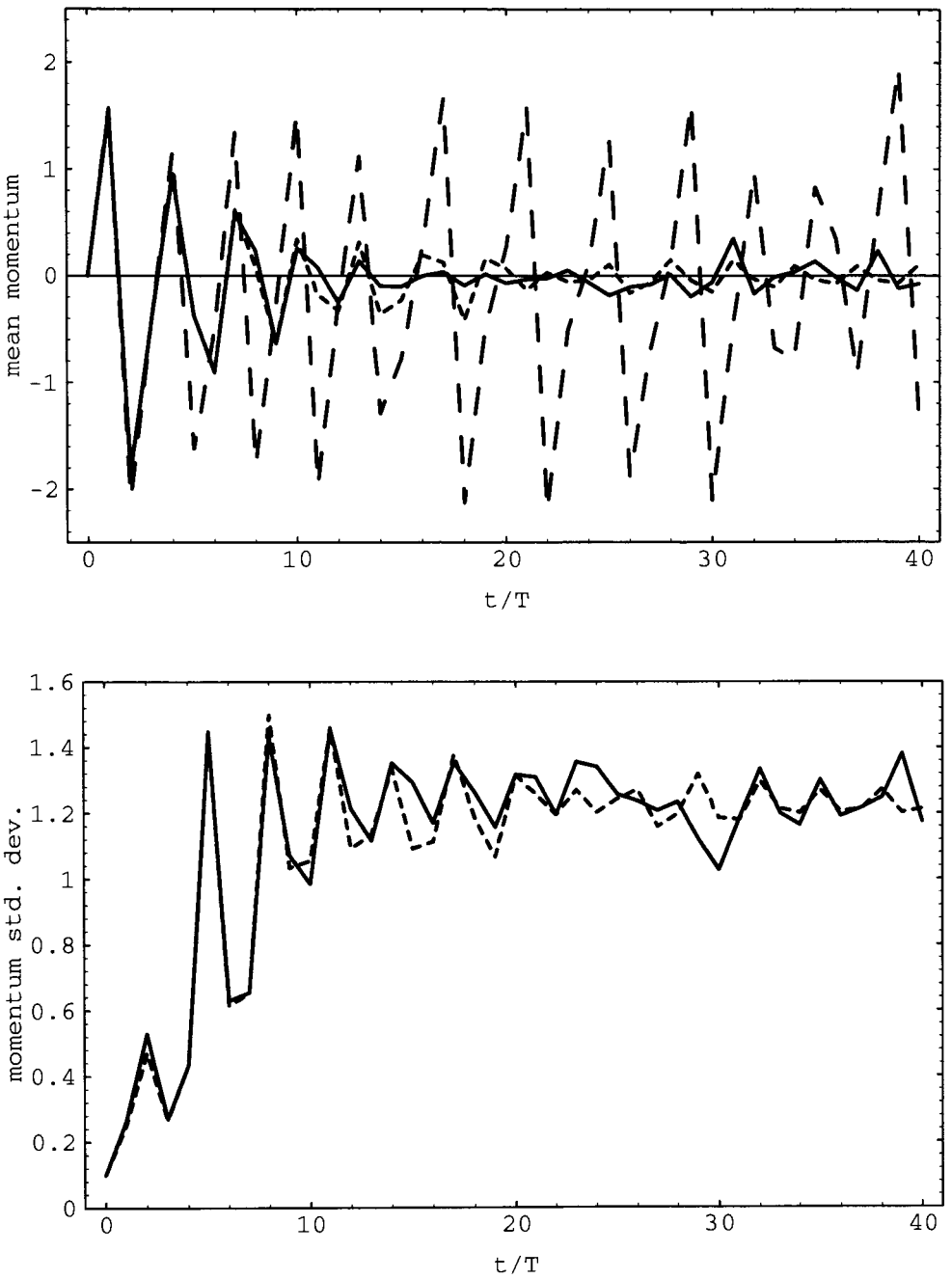

Figure 3.8: (continued) Same as previous page, but for momentum.

valid.

Figure 3.9 presents the results for similar calculations, but using the non-chaotic standard parameters (recall that these parameters differ from the chaotic standard values only in the location of the initial state). Here the Ehrenfest trajectory closely follows the centroids for a much longer time than in the chaotic case. In addition the widths grow much more slowly and the means exhibit large oscillations longer than in the chaotic case. These features are all consistent with the very slow delocalization observed in the phase space distributions for the regular case (figure 3.5). Finally, noting the different scales between these plots and those of figure 3.8, it is apparent that the classical means and widths agree more closely with the corresponding quantum values in the non-chaotic case than in the chaotic case.

To illustrate how these results depend on the degree of classicality of the quantum system, figure 3.10 presents a comparison of quantal and classical means and deviations for an initial gaussian state with centroid $(\langle q\rangle, \langle p\rangle) = (0.2, 0)$ in the chaotic zone, and widths $\Delta q = \Delta p = 0.2 \cdot 2^{1/2}$. The quantum calculations used $\hbar = 0.16$. Compared with the case of $\hbar = 0.02$ in figure 3.8, the quantum values here do not approach as well defined steady states, instead exhibiting larger fluctuations. Note also from figure 3.10 that at longer times the quantum position width appears to average below the classical width, suggesting that the quantum state is weakly localized at large $\hbar$.

3.4 Discussion of Results

The results of the previous two sections may be summarized as follows. In the chaotic case, the initially well localized state rapidly spreads to fill the chaotic zone. For very short times Ehrenfest's theorem is valid and the quantum and classical phase space distributions resemble each other closely. At longer times interference dominates the quantum distributions, although the Husimi density (and lower distribution moments) resemble more and more closely the classical distribution (and

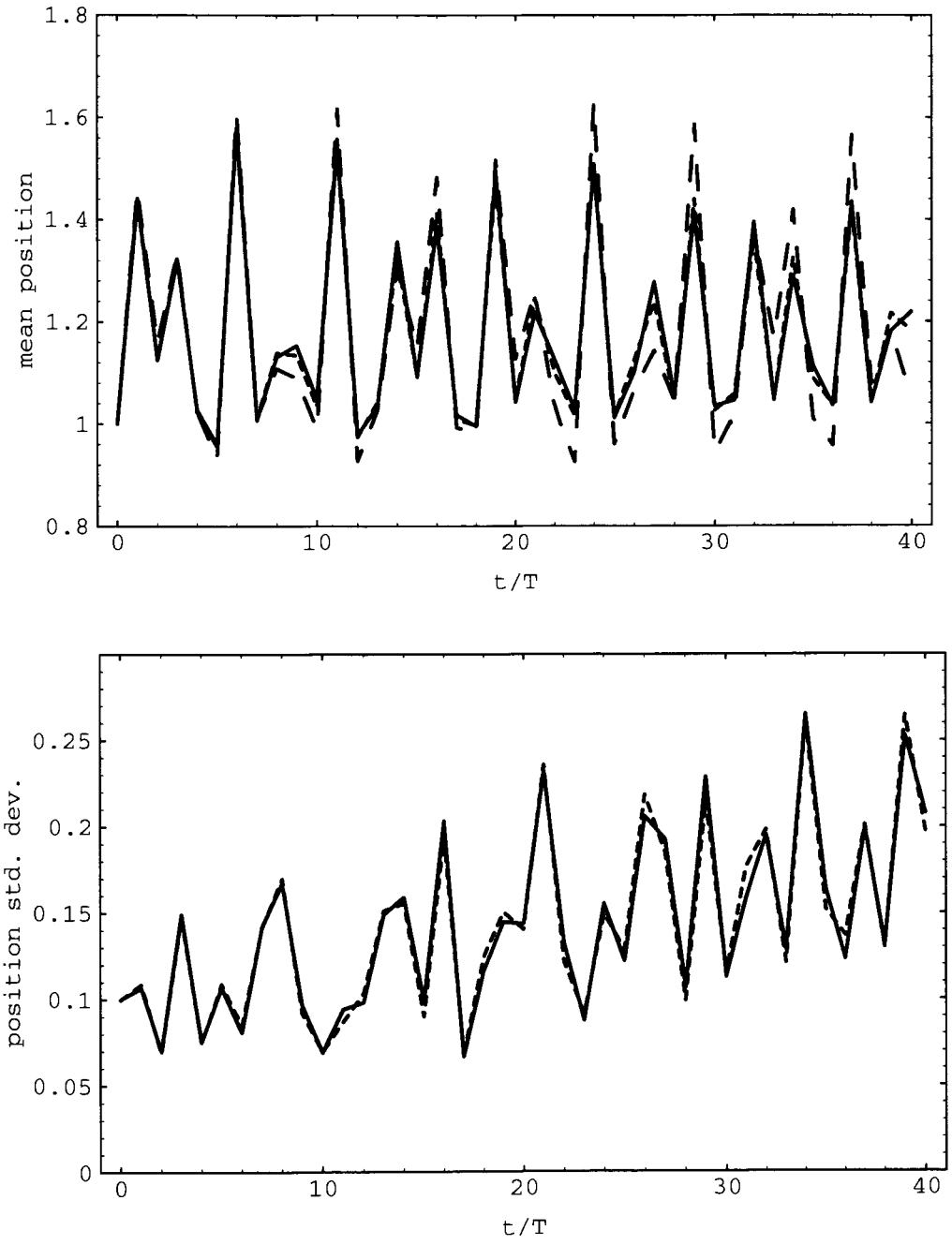

Figure 3.9: Mean position (top) and standard deviation in position (bottom) for DQO quantum state (solid line) and classical distribution (finely dashed line), using the non-chaotic standard parameters. The Ehrenfest trajectory (coarsely dashed line) is also indicated on the top graph.

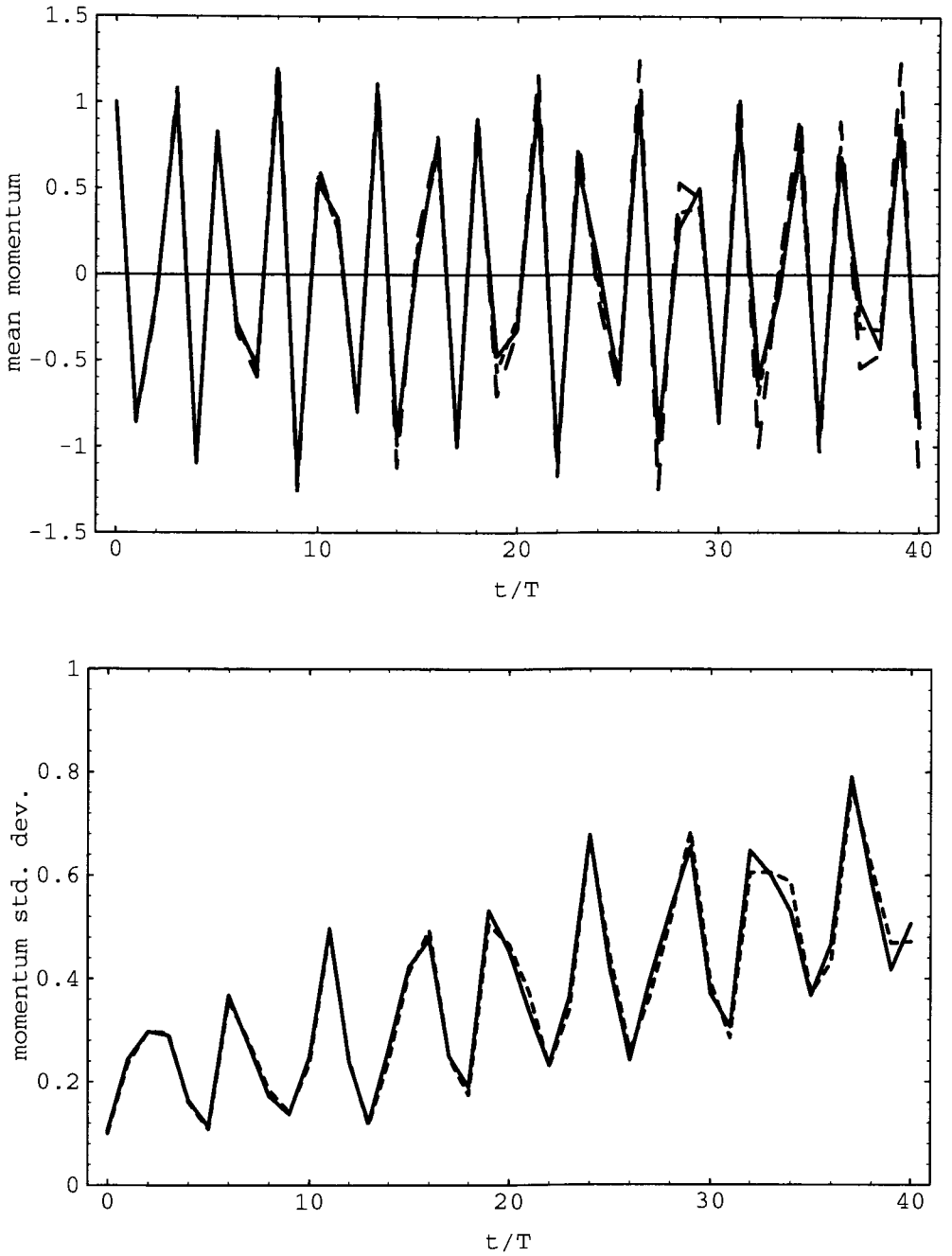

Figure 3.9: (continued) Same as previous page, but for momentum.

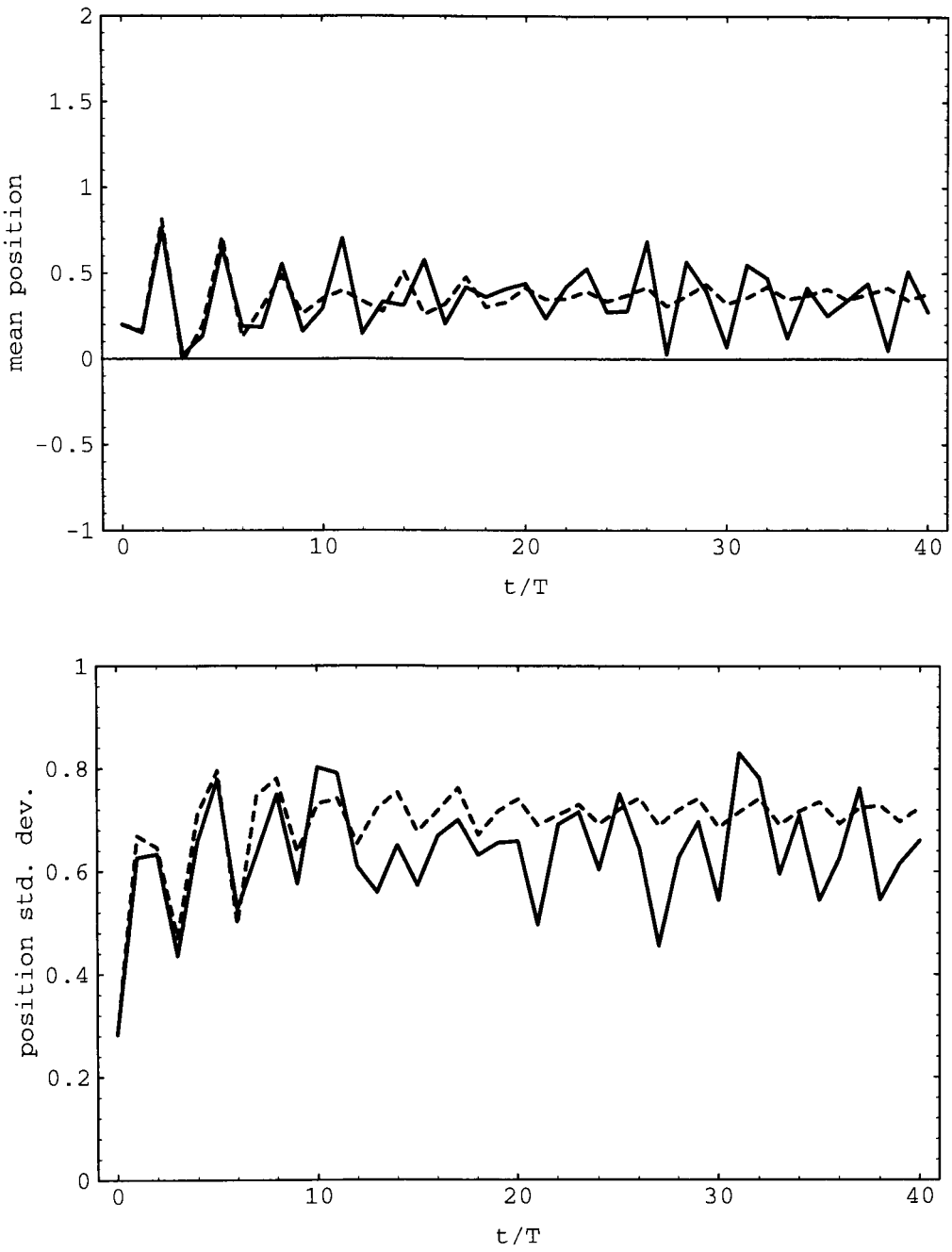

Figure 3.10: Mean position (top) and standard deviation in position (bottom) for DQO quantum state (solid line) and classical distribution (dashed line), for a state launched in the chaotic zone using $\hbar = 0.16$.

lower moments) as $\hbar$ is decreased. Also, at small $\hbar$, quantum and classical means and widths agree reasonably well long after Ehrenfest's theorem becomes invalid. In the regular case, Ehrenfest's theorem is valid for much longer times, and quantal and classical distributions (and lower moments) agree better, compared with the chaotic case.

This section will present arguments which attempt to explain these various results and provide a picture of the evolution in more general systems.

3.4.1 Time Scales

It is sometimes suggested [5] that for times less than roughly $t_{\rm r} = \hbar/\Delta E$, where ΔE is a typical energy level spacing, a quantum state will evolve essentially classically, since after $t_{\rm r}$ it will be possible to resolve the discrete nature of the spectrum, and, recalling the discussion in the Introduction, quantum recurrences should begin. However, this argument cannot hold in general. Clearly some states, *e.g.* a coherent state in a harmonic oscillator, behave classically much longer than $t_{\rm r}$. Also, one would not expect that a general, non-localized quantum state exhibiting interference would evolve classically for even short times.

Indeed, it is straightforward to show that in general for one-dimensional bounded undriven semiclassical systems the time $2\pi t_{\rm r}$ is actually a *classical* time, namely the classical period of motion. First note that the classical action $I(E)$ of an orbit of energy E is defined as

$$I(E) = \frac{1}{2\pi} \oint p\, dq, \tag{3.63}$$

where the integral is taken along the closed orbit. The phase space integral can be related to the number of energy eigenstates $N(E)$ below energy E in the semiclassical limit by Weyl's formula [1],

$$N(E) = \frac{1}{2\pi\hbar} \oint p\, dq, \tag{3.64}$$

which gives

$$I(E) = \hbar N(E). \tag{3.65}$$

Thus the mean energy level spacing is

$$\Delta E = \frac{dE(N)}{dN} \tag{3.66}$$

$$= \frac{dE(I)}{dI}\frac{dI}{dN}$$

$$= \omega(I)\hbar \tag{3.67}$$

$$= \frac{2\pi\hbar}{T}, \tag{3.68}$$

where $T = 2\pi/\omega(I)$ is the classical orbital period. Thus the recurrences of period $2\pi\hbar/\Delta E$ are of essentially classical origin. Distinctly quantum recurrences are related to other aspects of the spectrum.

One further time scale discussed in the literature is the Ehrenfest time $t_{\rm Ehr}$. This is the time during which a quantum state satisfies the conditions for Ehrenfest's theorem, and hence the state's centroid evolves classically. Clearly $t_{\rm Ehr}$ shares with $t_{\rm r}$ the problem of being initial-state dependent. However, for initial Gaussian (or near-Gaussian) states, it is possible to distinguish between the $\hbar$ dependence of $t_{\rm Ehr}$ in the classically chaotic and non-chaotic cases.

Consider first the chaotic case. We can choose the initial width of the state to be of order $\Delta q(0) \sim \hbar^{1/2}$ (this is a numerical estimate only, as the units are not correct). Suppose $\Delta q(0) \ll L_V$, where L_V is the length scale of potential variations. Then, as we will see in the next section, $\Delta q(t)$ will grow as $e^{\lambda t}$ for long enough t, where λ is the largest Lyapunov exponent. Thus, taking $\Delta q(t_{\rm Ehr}) = L_V$, we find

$$t_{\rm Ehr} \sim \frac{1}{\lambda}\ln\left(\frac{L_V}{\hbar^{1/2}}\right), \tag{3.69}$$

or $t_{\rm Ehr} \sim -\ln\hbar$ for the $\hbar$ dependence. In the non-chaotic case, $\Delta q(t)$ will grow only as some power of t, so we expect $t_{\rm Ehr} \sim \hbar^a$, for $a < 0$.

3.4.2 The Linear (or Ehrenfest) Regime

A more fruitful approach to understand the observed short time agreement between quantal and classical evolution is to examine the quantal evolution of well localized states. Ehrenfest's theorem already tells us that for states with $\Delta q \ll L_V$ the

centroids evolve classically, but can we say more about the entire probability distributions?

To answer this question, consider the time evolution of the Wigner distribution. It can be shown [31] that for a quantum state evolving under the Hamiltonian $H(Q,P) = P^2/(2m) + V(Q)$, this distribution satisfies

$$\frac{\partial}{\partial t}\rho_{\rm W}(q,p,t) = -\frac{p}{m}\frac{\partial \rho_{\rm W}}{\partial q} + \sum_{\lambda}\frac{1}{\lambda!}\left(\frac{\hbar}{2i}\right)^{\lambda-1}\frac{\partial^{\lambda}V(q)}{\partial q^{\lambda}}\frac{\partial^{\lambda}\rho_{\rm W}}{\partial p^{\lambda}}, \tag{3.70}$$

where the sum is over positive odd λ. Let us now estimate the size of the terms in the above series under the Ehrenfest conditions. It can be seen directly from the definition of the Wigner distribution (3.28) that the momentum dependence of $\rho_{\rm W}(q,p)$ consists of a superposition of oscillations, the most rapidly varying significant component of which goes roughly as $\exp(ip\Delta q/\hbar)$. Thus we can place a rough upper limit on the size of the momentum derivatives appearing in (3.70), namely

$$\frac{\partial^{\lambda}\rho_{\rm W}}{\partial p^{\lambda}} \lesssim \left(\frac{\Delta q}{\hbar}\right)^{\lambda}\rho_{\rm W}. \tag{3.71}$$

This implies that the term labelled by λ in the sum in (3.70) is no larger than the order of

$$\frac{(\Delta q)^{\lambda}}{\hbar}\frac{\partial^{\lambda}V(q)}{\partial q^{\lambda}}\rho_{\rm W}. \tag{3.72}$$

Now if the conditions for the validity of Ehrenfest's theorem are satisfied (namely $\Delta q \ll L_V$ or $\partial V/\partial q$ is a linear or constant function of q), then we immediately see that we can ignore all but the first term in the sum and write

$$\frac{\partial \rho_{\rm W}}{\partial t} = -\frac{p}{m}\frac{\partial \rho_{\rm W}}{\partial q} + \frac{\partial V(q)}{\partial q}\frac{\partial \rho_{\rm W}}{\partial p}, \tag{3.73}$$

which is identical in form to Liouville's equation, (1.4).

This result means that if Ehrenfest's conditions are satisfied, we can propagate $\rho_{\rm W}(q,p)$, and hence *the entire state function* (to within an overall phase factor), using completely classical techniques. This suggests referring to the quantal evolution in this case as *practically* classical. I emphasize that this is a purely mathematical result, and one cannot conclude that a practically classical quantum state "is" a

classical distribution. Indeed, $\rho_{\mathrm{W}}(q,p)$ can, in general, exhibit interference and have negative valued regions even when $\Delta q \ll L_V$ (as long as the initial state exhibits such interference). Note in addition that the conditions for practically classical behaviour are distinct from those for the classical regime. A macroscopic quantum state with $\Delta q > L_V$ will not behave practically classically, whereas a microscopic state with $\Delta q \ll L_V$ will.

The importance of practically classical behaviour to quantum chaos is readily apparent. Note that the conditions for the linear evolution of a classical trajectory perturbation discussed in section 3.1.1 are identical to those for practically classical behaviour (thus we can interchangeably refer to the linear, Ehrenfest, or practically classical regimes). Recall that by definition a classical trajectory perturbation in a chaotic system will grow exponentially with time on average if the perturbation remains linear. A linear-regime classical Liouville density will exponentially stretch and shrink along directions corresponding to positive and negative Lyapunov exponents, respectively. Thus a practically-classical Wigner density in a classically chaotic system will do the same, and so any quantum state initially localized in the linear regime will exponentially delocalize on the inverse Lyapunov exponent time scale. Once Δq has exceeded L_V the above approximations of course break down, and the state may or may not continue to spread. This result was derived in a very different way by Fox [15].

These arguments explain the close agreement at short times between the DQO calculations of the Wigner and Liouville distributions, and hence also between their smoothed counterparts ρ_{H} and ρ_{SL} and between their means and deviations. Close agreement lasts longer in the classically non-chaotic case because the state does not exhibit exponential stretching. The DQO calculations suggest that while ρ_{W} and ρ_{L} differ markedly outside the Ehrenfest regime because of the development of interference in ρ_{W}, the smoothed densities and low distribution moments can still agree quite well, with the degree of agreement improving with decreasing $\hbar$. The explanation of this aspect of the calculations will be the subject of the next section.

3.4.3 The Classical Regime

It is sometimes claimed [16] that the validity of Ehrenfest's theorem characterizes the classical regime. However, as pointed out above, we cannot expect $\Delta q \ll L_V$ for all states in the classical regime (as defined in the Introduction). Indeed, we now know that localized quantum states of classically chaotic systems will grow to beyond the Ehrenfest regime at a rate determined by the Lyapunov exponent, which certainly does not generally vanish for macroscopic systems. What then can we say about the quantal evolution in the classical regime?

First note that, as Yang [33] and Ballentine, Yang, and Zibin [37] have pointed out, for a general quantum state we cannot choose a classical distribution such that the q and p distributions evolve the same classically and quantum mechanically for all time, a result that can be traced to the non-commutativity of Q and P in quantum mechanics. Yang suggested that in the classical regime this non-commutativity will be irrelevant and the quantum probability densities will evolve essentially classically.

To see explicitly how this can come about, consider the time evolution of the two quantum phase space distributions studied here. First, for the Wigner density, recall its time evolution equation (3.70) presented above. It is sometimes argued that this equation always reduces to the Liouville equation in the classical limit, since each successive term in the sum in (3.70) appears to be of order $\hbar^2$ smaller than the previous term. However, as shown above, unless the conditions for Ehrenfest's theorem are satisfied this will not be the case, because each derivative $\partial/\partial p$ in (3.70) brings down a factor of $\hbar$ (recall (3.71)). The fact that equation (3.70) does not typically reduce to the Liouville equation in the classical limit has been noted by Heller [38] and Takahashi [10].

For the Husimi distribution, it can be shown [39] that the time derivative of ρ_{H} under the Hamiltonian $H(Q,P) = P^2/(2m) + V(Q)$ can be written conveniently as the sum of potential independent and dependent parts, namely

$$\frac{\partial}{\partial t}\rho_{\mathrm{H}}(q,p,t) = \frac{\partial_k \rho_{\mathrm{H}}}{\partial t} + \frac{\partial_v \rho_{\mathrm{H}}}{\partial t} \tag{3.74}$$

where

$$\frac{\partial_k \rho_{\mathrm{H}}}{\partial t} = -\frac{p}{m}\frac{\partial \rho_{\mathrm{H}}}{\partial q} - \frac{(\Delta_{\mathrm{s}} p)^2}{m}\frac{\partial^2 \rho_{\mathrm{H}}}{\partial p \partial q} \tag{3.75}$$

and

$$\frac{\partial_v \rho_{\mathrm{H}}}{\partial t} = \sum_{\lambda,\mu,k} \frac{(i\hbar)^{\lambda-1}(\Delta_{\mathrm{s}} q)^{2\mu-2k}}{2^{\lambda+k-1}\lambda! k! (\mu-2k)!} \frac{\partial^{\lambda+\mu} V(q)}{\partial q^{\lambda+\mu}} \frac{\partial^{\lambda}}{\partial p^{\lambda}} \frac{\partial^{\mu-2k} \rho_{\mathrm{H}}}{\partial q^{\mu-2k}}. \tag{3.76}$$

Here $\Delta_{\mathrm{s}} q = \hbar/(2\Delta_{\mathrm{s}} p)$ is the position standard deviation of the Gaussian smoothing function used to define ρ_{H}, and the triple sum in (3.76) is taken over odd positive λ, all nonnegative integers μ, and all nonnegative integers k such that $\mu - 2k \geq 0$. It must be stressed that $\Delta_{\mathrm{s}} q$ and $\Delta_{\mathrm{s}} p$ characterize only the smoothing function, whereas Δq and Δp are the widths of the (unsmoothed) state itself.

Now, to determine the limiting behaviour of ρ_{H}, we can take an approach similar to that taken for the Wigner density above. Note first that because ρ_{H} can be defined through (3.48) as a Gaussian smoothing of ρ_{W}, with $\Delta_{\mathrm{s}} q$ and $\Delta_{\mathrm{s}} p$ being the scale of the smoothing in q and p, we can place rough upper limits on the size of the partial derivatives of ρ_{H}, namely

$$\frac{\partial^{\lambda} \rho_{\mathrm{H}}}{\partial q^{\lambda}} \lesssim \frac{\rho_{\mathrm{H}}}{(\Delta_{\mathrm{s}} q)^{\lambda}}, \tag{3.77}$$

$$\frac{\partial^{\lambda} \rho_{\mathrm{H}}}{\partial p^{\lambda}} \lesssim \frac{\rho_{\mathrm{H}}}{(\Delta_{\mathrm{s}} p)^{\lambda}}. \tag{3.78}$$

Thus the second term in the potential-independent part (3.75) is no larger than the order of $\Delta_{\mathrm{s}} p / p_{\mathrm{typ}}$ relative to the first term, where p_{typ} is a typical momentum value in the state. Similarly, the terms in the sum (3.76) labelled by λ and μ will be no larger than roughly

$$\frac{(\Delta_{\mathrm{s}} q)^{\lambda+\mu}}{\hbar} \frac{\partial^{\lambda+\mu} V(q)}{\partial q^{\lambda+\mu}} \rho_{\mathrm{H}}. \tag{3.79}$$

Here the relation $\Delta_{\mathrm{s}} q = \hbar/(2\Delta_{\mathrm{s}} p)$ has been used, and the k dependence has fallen out in this approximation. Therefore we finally see that if $\Delta_{\mathrm{s}} p \ll p_{\mathrm{typ}}$ and $\Delta_{\mathrm{s}} q \ll L_V$ (or $\partial V/\partial q$ is a linear or constant function of q), then the smallest term in the sum (3.76) will be that for $\lambda = 1$ and $\mu = k = 0$ and we can make the approximation

$$\frac{\partial \rho_{\mathrm{H}}}{\partial t} = -\frac{p}{m}\frac{\partial \rho_{\mathrm{H}}}{\partial q} + \frac{\partial V(q)}{\partial q}\frac{\partial \rho_{\mathrm{H}}}{\partial p}, \tag{3.80}$$

so that ρ_{H} satisfies the familiar Liouville equation.

Many of the comments of section 3.4.2 on practically classical behaviour apply here. Equation (3.80) is a mathematical result; it states that under certain conditions a suitably coarse grained Wigner density evolves essentially like the classical Liouville distribution. Recalling that $\Delta_{\mathrm{s}}q$ and $\Delta_{\mathrm{s}}p$ characterize not the state but our degree of smoothing of the state, the interference patterns may still exist (in ρ_{W}) when (3.80) is satisfied. It is only when we do not "look more closely" than the scales $\Delta_{\mathrm{s}}q$ and $\Delta_{\mathrm{s}}p$ (*i.e.* when we examine the Husimi density) that interference is not noticeable and the evolution is essentially classical. Although $\Delta_{\mathrm{s}}q$ and $\Delta_{\mathrm{s}}p$ can be extremely small relative to macroscopic scales, the scales of typical interference patterns can be far smaller still.

Note in addition that, because of the property given in section 3.2.1 that the Husimi density of a mixed state is the weighted sum of the Husimi densities of the elements of the mixture, the result (3.80) applies equally well to mixed states as to pure states. A similar comment holds for the practically classical evolution of the Wigner density in section 3.4.2.

Whereas the Ehrenfest condition $\Delta q \ll L_V$ does not, as discussed above, characterize the classical regime of quantum mechanics, the conditions $\Delta_{\mathrm{s}}p \ll p_{\mathrm{typ}}$ and $\Delta_{\mathrm{s}}q \ll L_V$ in fact do. To see this, note that the product of these last two inequalities can be written $\hbar \ll L_V p_{\mathrm{typ}}$. Since the product $L_V p_{\mathrm{typ}}$ will be a typical system action S, we can instead write $\hbar \ll S$, which defines the classical regime.

It is important to stress that the behaviour of a quantum state in the classical regime is given by Liouville's equation rather than Hamilton's equations. For a classically regular system and in the classical regime, we can construct a Gaussian initial quantum state (essentially a δ-function in phase space) which remains well localized for extremely long times (since t_{Ehr} grows algebraically with reciprocal $\hbar$), and therefore essentially follows Hamilton's equations. However, we now see that for a classically chaotic system we *cannot do this.* Any initial width will grow on the inverse Lyapunov time scale until ρ_{H} fills the accessible region of phase space. The

undergraduate example of a quantum wave packet for a free bullet remaining well localized over the age of the universe can no longer reassure us.

Fox's results on the growth of states in the linear regime (which were mentioned in the Introduction) have prompted him to claim that quantum-classical correspondence breaks down for classically chaotic systems, and to state that "to properly describe classical mechanical chaos, one must do quantum mechanics" [15]. However, equation (3.80) tells us that we are in fact able to calculate state evolution in the classical regime using classical (albeit statistical) mechanics. Predictions of classical and quantum mechanics will never differ significantly because the classical description will always include some initial state uncertainties, which will be much larger than the minimum quantum state uncertainties, and which, evolving under the Liouville equation, will rapidly fill the accessible chaotic region. For classically chaotic systems we are not able to escape the probabilistic nature of quantum mechanics, although in the classical regime the probabilities behave essentially classically.

Chapter 4

The Characterization of Quantum Chaos

This chapter applies the ideas presented so far towards generalizing some common characteristics of classical chaos to quantum mechanics. Section 4.1 describes an approach to reconcile the stability of quantal evolution with the instability and practical irreversibility of classical chaos. Section 4.2 presents a number of techniques for generalizing the classical Lyapunov exponent to quantum systems.

4.1 Sensitivity to Perturbations and Irreversibility

4.1.1 Classical Background

When discussing the relationship between classical chaos and irreversibility, it is important to distinguish between two separate aspects of irreversible behaviour requiring explanation. The first is the fact that phenomena in the macroscopic world are asymmetric with respect to time, whereas the relevant fundamental physical laws are invariant under time reversal. Time-symmetric laws themselves cannot resolve this discrepancy, and explanations have involved cosmological arguments [40]. I will

not pursue this aspect further.

The second problem is that *given* the asymmetry described above, how can we explain, in terms of the fundamental laws, the irreversible behaviour which is observed (and described, for example, by the second law of thermodynamics and Boltzmann's equation). A simple illustrative example of this type of problem is the following. Given that we are able to prepare initial states rather than "final" states, why do we observe ice cubes melting in glasses of water but never the reverse process?

Classical chaos can be relevant to questions of this latter sort. Consider the effect of sensitive dependence on initial conditions in the following thought experiment. Imagine a chaotic classical system in some initial state at time $t = 0$. Allow the system to evolve until some time $t = t_{\rm mr}$. Now perform a motion reversal, changing the signs of all momenta, and let the system evolve until $t = 2t_{\rm mr}$. If the motion reversal was exact and the Hamiltonian unchanged on the two legs of the evolution, then the system would of course return precisely to its initial state (with momenta reversed). Any small perturbation to the system's trajectory, however, would become exponentially magnified with time, making it practically impossible to perform such an experiment for evolution times exceeding the order of the inverse Lyapunov exponent time scale. If we could readily prepare the initial state, the forward evolution would be observable while the reverse evolution could be exceedingly unlikely.

4.1.2 Quantum Approaches

As shown in the Introduction, quantum states are always stable to perturbations in the state vector. Workers have taken a number of approaches to try to reconcile this fact with the observed presence of chaos in the classical regime, and thereby maintain the sort of explanation of irreversibility outlined above. Peres [41] has studied the effect of perturbations of the quantum Hamiltonian rather than of the state vector. He examined, for a particular coupled rotator model, the overlap

$$S(t) = \left| \langle \Psi | e^{itH/\hbar} e^{-itH'/\hbar} | \Psi \rangle \right|^2 \tag{4.1}$$

between the states evolving under the unperturbed and perturbed Hamiltonians H and H'. Here $|\Psi\rangle$ is the initial state. He found that $S(t)$ approaches smaller values when the system is classically chaotic than when it is classically non-chaotic. Benet *et al.* [42] have examined the influence of perturbations of the Hamiltonian on the energy eigenfunctions for classically chaotic and non-chaotic cases. Schack *et al.* [43] have studied the Hilbert space evolution of state vectors under a stochastically perturbed Hamiltonian for a kicked top model, under classically chaotic and non-chaotic conditions.

Blümel [44] presents a quantum system which, he suggests, exhibits exponential sensitivity and chaos. The system consists of a neutral spin-1/2 particle travelling through a collinear sequence of identical homogeneous magnetic field sections. Each field section precesses the spin by a fixed angle β about the same axis. Although the author conceptually partitions the field sections into a Fibonacci sequence, the same conclusions follow for a simple geometric sequence partition. We consider the state of the particle, $|\Psi_n\rangle$, after passing through 2^n field sections, for $n = 0, 1, 2, \ldots$. Consider the states $|\Psi_n\rangle$ and $|\Psi'_n\rangle$ which result from separate runs in which all field sections advance the spins by β and $\beta' = \beta + \delta\beta$, respectively, where $\delta\beta \ll \beta$. Clearly the difference in the spin's magnetic moment direction between the unprimed and primed runs will grow exponentially with n. Blümel claims that this indicates chaos in the spin. However, in order for the perturbation to grow exponentially with time, the field sections would have to be spaced more and more closely down the sequence. More importantly, the state of the spin is *not* sensitive to its initial state, only to the value β if all sections are identical.

A number of authors have performed numerical calculations that indicate a sharp distinction in the "computational reversibility" behaviour of classical and quantum systems. In these studies, quantum and corresponding classical states were propagated from $t = 0$ to some time $t = t_{\mathrm{mr}}$, a motion reversal performed, and the states propagated to $t = 2t_{\mathrm{mr}}$ to try to recover the initial states. For classically chaotic systems, the classical states returned poorly or not at all to the initial state, whereas

the quantum states retured extremely accurately. Shepelyansky [17] performed these calculations on a kicked rotator model, and Casati *et al.* [18] used a model of a hydrogen atom in a microwave field. Haeri [45] also studied the kicked rotator in this context.

To illustrate this type of result, computational reversibility calculations were performed for the DQO. Initial Gaussian Liouville distributions and quantum states were chosen according to the chaotic standard parameters of section 3.2.2. The classical and quantum calculations used 20000 particles and 2000 grid points, respectively. The states were first propagated until $t = 60T$, where T is the period of the driving force. At this time, the momentum of each classical particle was reversed and the quantum state was complex conjugated. Then the states were propagated to $t = 120T$. Figure 4.1 shows the position standard deviation Δq for the classical and quantum cases, plotted at integral multiples of the driving period. The classical evolution between $t = 60T$ and $t \simeq 90T$ mirrors the evolution before motion reversal, but the state does not return to its initial state. The quantum evolution, however, displays near perfect symmetry about $t = t_{\rm mr} = 60T$, and in fact the values of Δq at the times t and $120T - t$ differ by no more than 10^{-6} in absolute units.

It must be stressed that these results reflect computational rather than physical irreversibility. Departures from perfect reversibility are due to numerical approximations and round-off errors, and different numerical techniques were used for the classical and quantum calculations. Assigning an integrator tolerance value of 10^{-7} for the quantum calculations is not physically equivalent to assigning the same tolerance value for the classical calculations, nor is it apparently physically equivalent to *anything*. Indeed we expect quantum dynamical calculations to be numerically "easy" deep in the quantum regime where only a few eigenstates are excited. A more physically meaningful approach to this problem will be the subject of the next section.

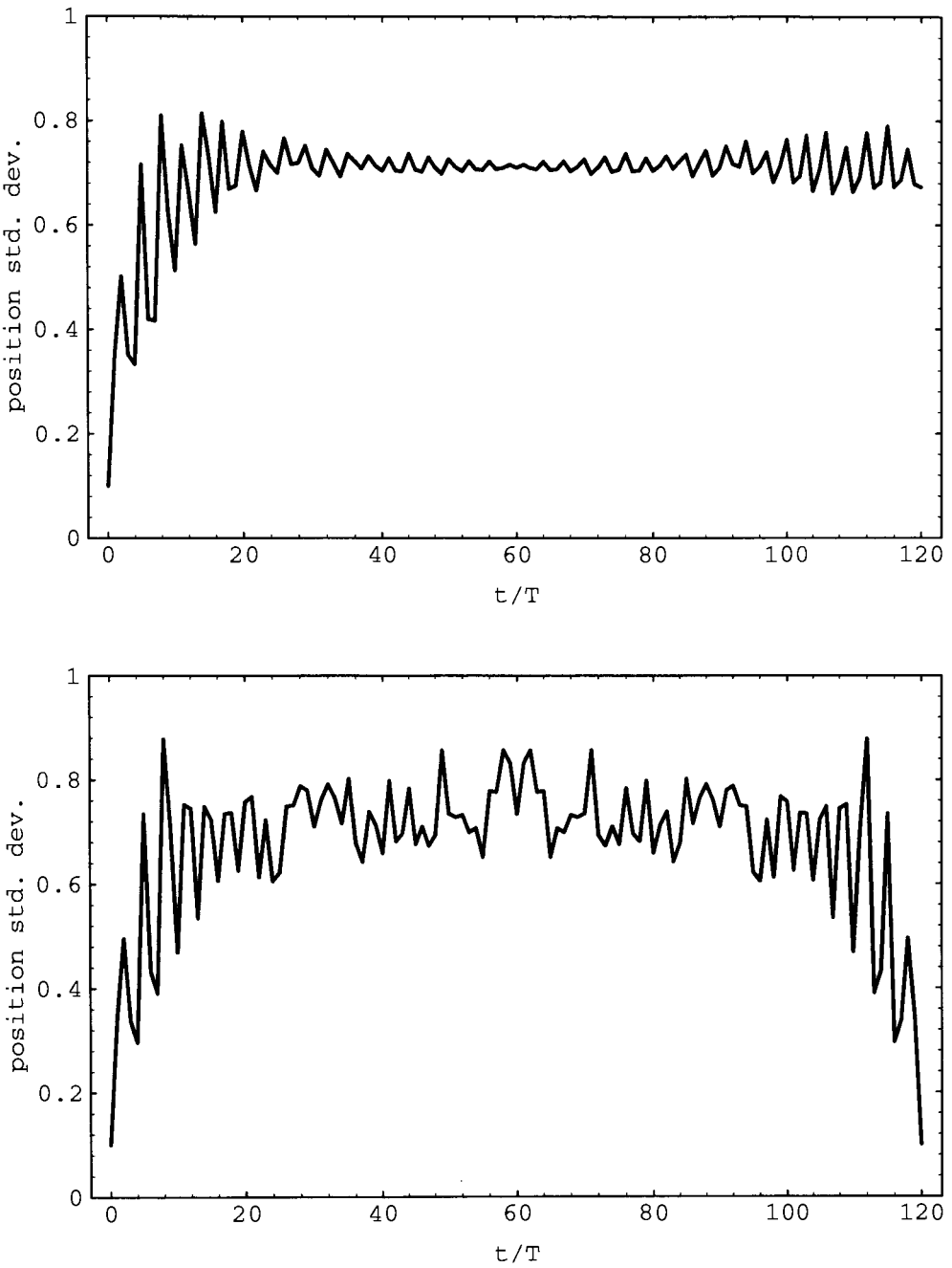

Figure 4.1: Standard deviation in position for DQO classical distribution (top) and quantum state (bottom), plotted versus time in periods of the driving force, and using the chaotic standard parameters. In both cases a motion reversal was performed at $t = 60T$.

4.1.3 Displaced Motion Reversal

Recalling the result of section 3.4.3 that the Husimi density evolves essentially according to the Liouville equation in the classical regime, quantal evolution in this regime must exhibit essentially the same sensitive dependence (as well as the statistical properties such as mixing and ergodicity) that the Liouville density can exhibit. However, it is useful to see *how* this behaviour arises as the classical regime is approached. To accomplish this, consider the following type of motion reversal calculation. An initial state is propagated from $t = 0$ to $t = t_{\mathrm{mr}}$ ensuring that numerical errors are negligible. Then a motion reversal is performed, followed immediately by a displacement of the entire state in position space by an amount δq. Finally the state is evolved to $t = 2t_{\mathrm{mr}}$, again ensuring negligible numerical errors. This type of calculation, which will be referred to as a *displaced motion reversal* calculation, can be applied to either a classical distribution or a quantum state, and in both cases the applied perturbations δq are physically equivalent. Any inability to recover the initial classical or quantum state is due solely to the displacement δq. The idea behind this approach is just that, although one may look for sensitivity to perturbations in quantum mechanics by other means, the correspondence principle tells us that studying perturbations of this type should reveal how classical sensitivity to perturbations arises as the classical regime is approached.

Qualitative results

Figure 4.2 presents smoothed Liouville densities ρ_{SL} and Husimi densities ρ_{H} for a series of displaced motion reversal calculations for the DQO. The initial Liouville distribution and quantum state were chosen according to the chaotic standard parameter values, both being Gaussian states with centroid $(\langle q \rangle, \langle p \rangle) = (0.2, 0)$. The total propagation time was $2t_{\mathrm{mr}}$, with $t_{\mathrm{mr}} = T$, the period of the driving force. The plots show the final states at $t = 2t_{\mathrm{mr}}$ using perturbations of $\delta q = 0.04$, 0.08, 0.16, 0.32, and 0.64 after the motion reversals. As expected, a sufficiently small perturbation

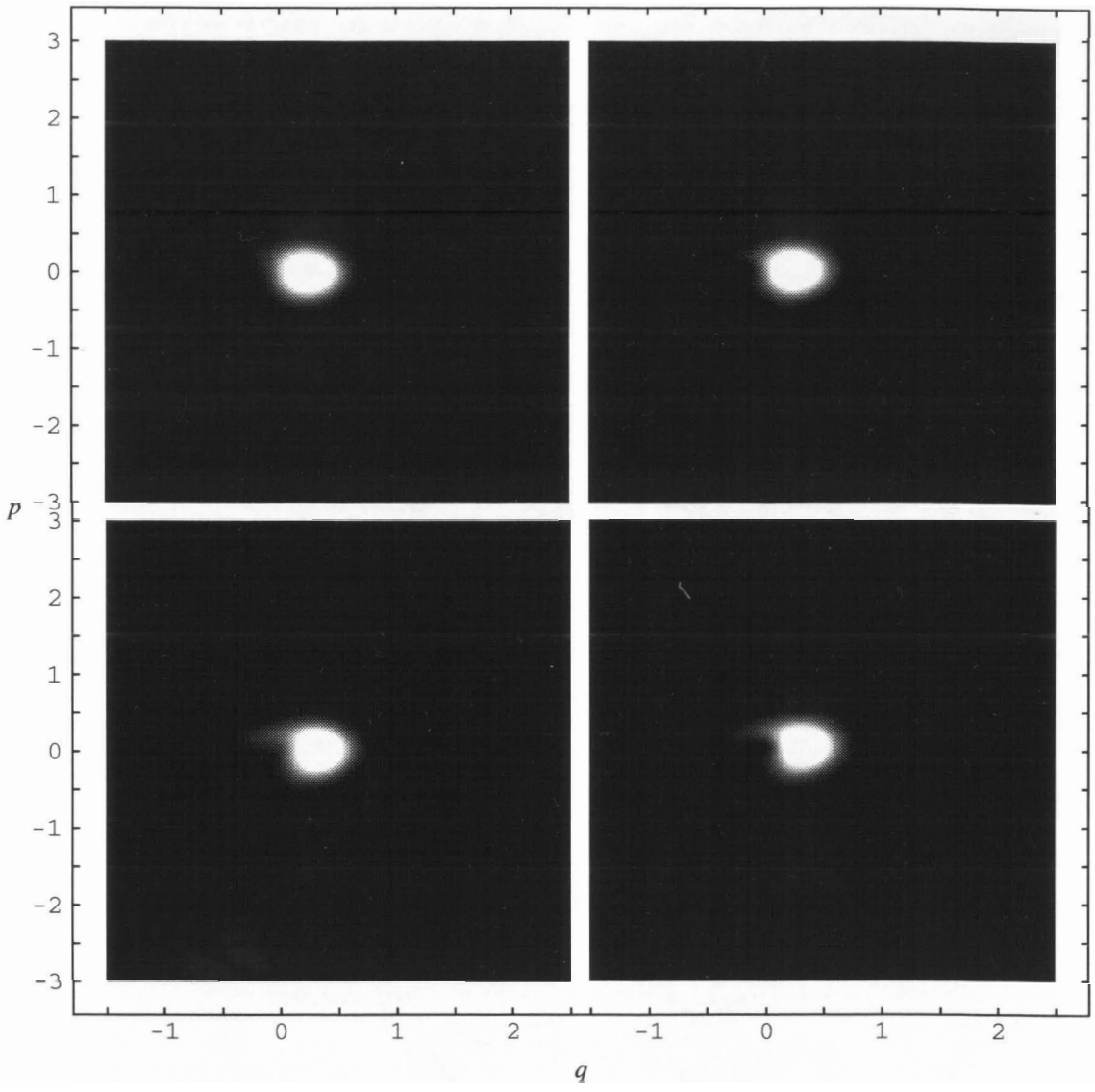

Figure 4.2: Final smoothed Liouville density (left column) and Husimi density (right column) for displaced motion reversal calculations for the DQO with the chaotic standard parameters. The states are shown at the final time $t = 2t_{\mathrm{mr}}$, with $t_{\mathrm{mr}} = 1T$, and on this page the displacements $\delta q = 0.04$ (top) and $\delta q = 0.08$ (bottom) were used. Both classical and quantum plots share the same grey scale, black and white corresponding to zero and a maximum density value, respectively.

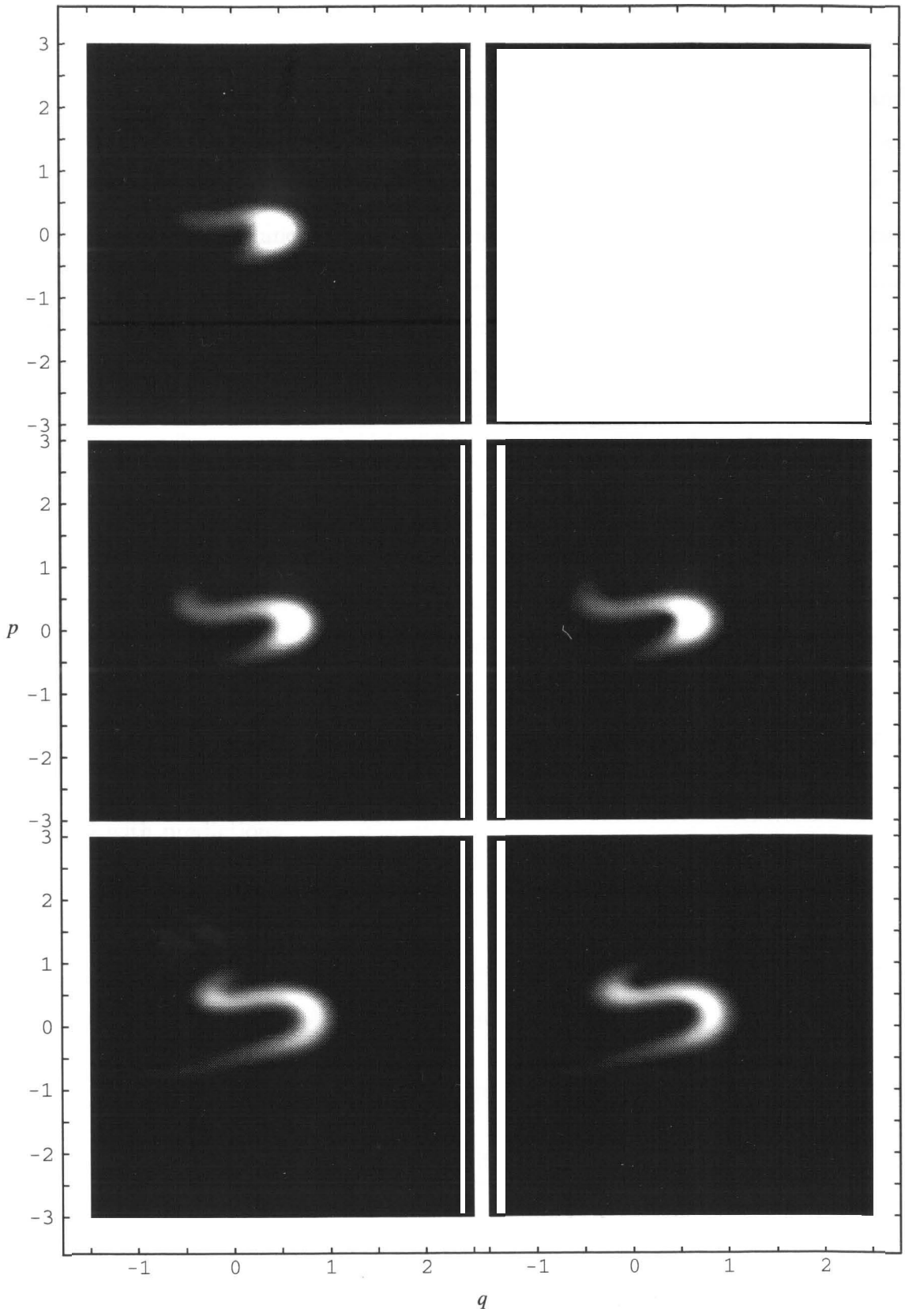

Figure 4.2: (cont.) ρ_{SL} (left) and ρ_{H} (right) for $\delta q = 0.16$, 0.32, and 0.64, top to bottom.

has negligble effect on the evolution: for $\delta q = 0.04$ both classical and quantum states return well to their initial Gaussian form. As δq increases, the states return less and less accurately to the initial state. However, for this value of $t_{\rm mr}$, *both* $\rho_{\rm SL}$ and $\rho_{\rm H}$ exhibit the same dependence on the perturbation δq.

Clearly this result cannot hold for arbitrary states. A classical distribution can be sensitive to arbitrarily small displacements δq, whereas a (bounded) quantum state cannot be sensitive to spatial displacements much smaller than the shortest de Broglie wavelength significantly present in the state. To illustrate this, figures 4.3 and 4.4 display the results of displaced motion reversal calculations at the final times $t = 2t_{\rm mr}$, with $t_{\rm mr} = 7T$ and $13T$, respectively. The chaotic standard parameters were used, and the applied values of δq are indicated in the figure captions. As $t_{\rm mr}$ increases, the size of the finest features in the (unsmoothed) classical state at the time of motion reversal decreases (recall figure 3.3), and the final classical states presented in figures 4.3 and 4.4 exhibit sensitivity to smaller and smaller δq. The final quantum states show essentially the same dependence on the perturbations as the classical states for $\delta q \gtrsim 0.04$, but return quite accurately to their initial states for $\delta q \lesssim 0.005$. These results will be made more quantitative below, and will be compared with predictions.

Quantitative results

In the classical case, a quantitative indication of the degree to which a state returns to its initial form after a displaced motion reversal is the overlap

$$S_{\rm cl}(\delta q, t_{\rm mr}) = 2\pi\hbar \iint \rho_{\rm L}(q,p,0)\rho'_{\rm L}(q,p,2t_{\rm mr})\, dq\, dp. \tag{4.2}$$

Here $\rho_{\rm L}(q,p,0)$ is the initial Liouville density, and $\rho'_{\rm L}(q,p,2t_{\rm mr})$ is the density at $t = 2t_{\rm mr}$, after a motion reversal and displacement δq at $t = t_{\rm mr}$, and a final motion reversal at $t = 2t_{\rm mr}$. The factor $2\pi\hbar$ ensures (for the particular initial states studied here) that $S_{\rm cl} = 1$ when the two densities are equal. As mentioned in the Introduction, the overlap between any two Liouville densities is constant in time. Thus we can

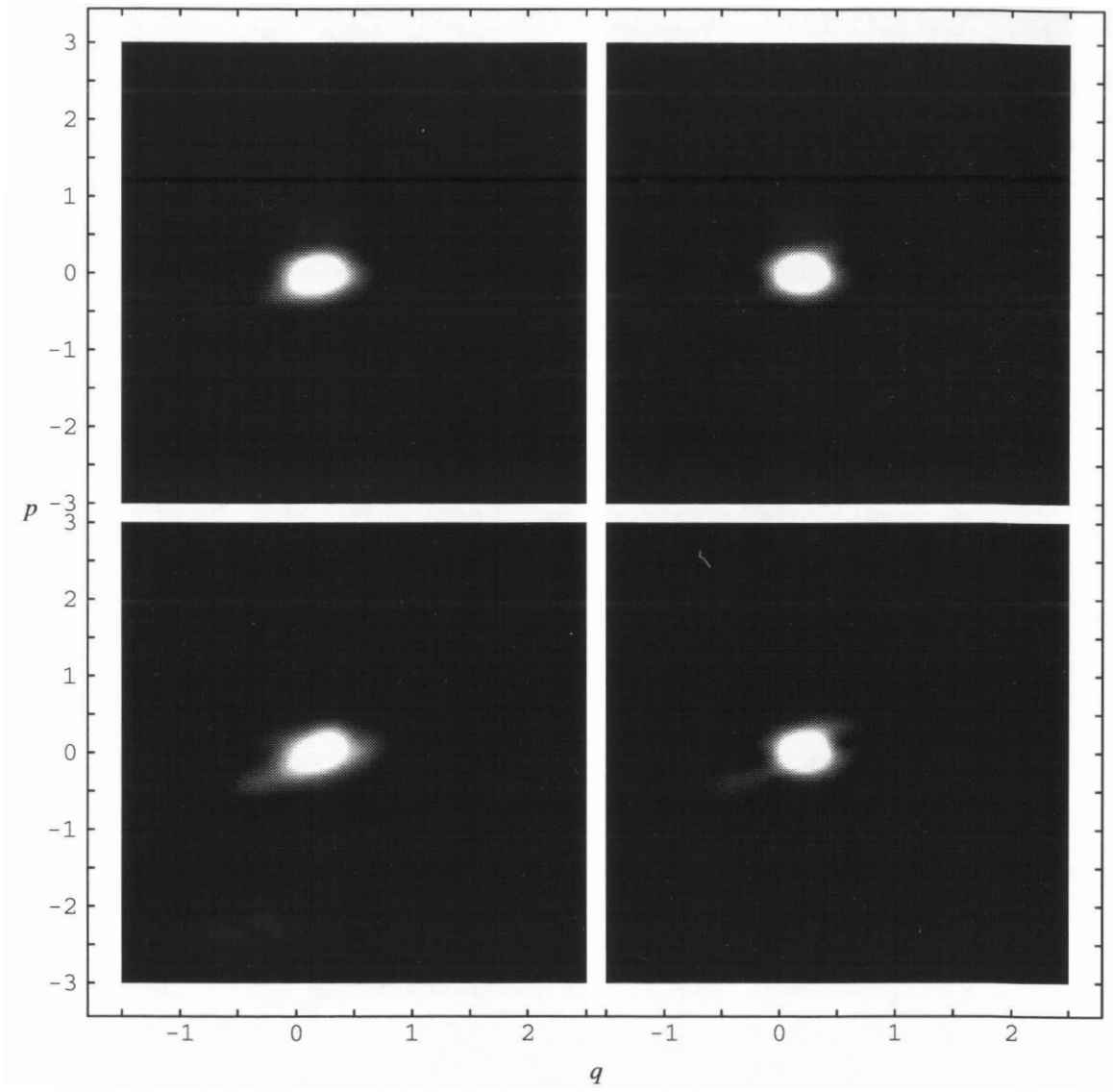

Figure 4.3: Final smoothed Liouville density (left column) and Husimi density (right column) for displaced motion reversal calculations for the DQO with the chaotic standard parameters. These calculations used $t_{\mathrm{mr}} = 7T$, and on this page the displacements $\delta q = 0.005$ (top) and $\delta q = 0.01$ (bottom) were used.

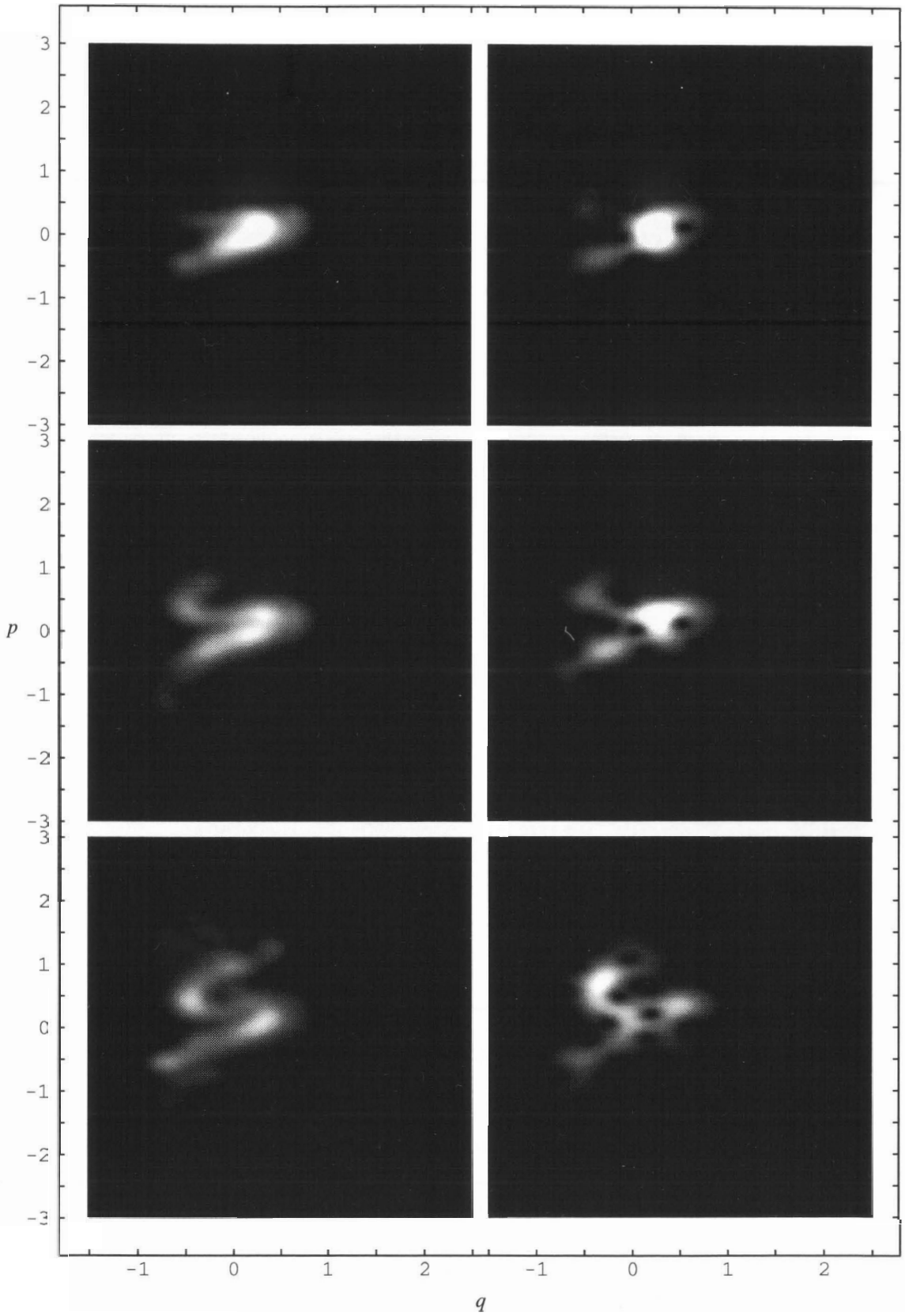

Figure 4.3: (cont.) ρ_{SL} (left) and ρ_{H} (right) for $\delta q = 0.02$, 0.04, and 0.08, top to bottom.

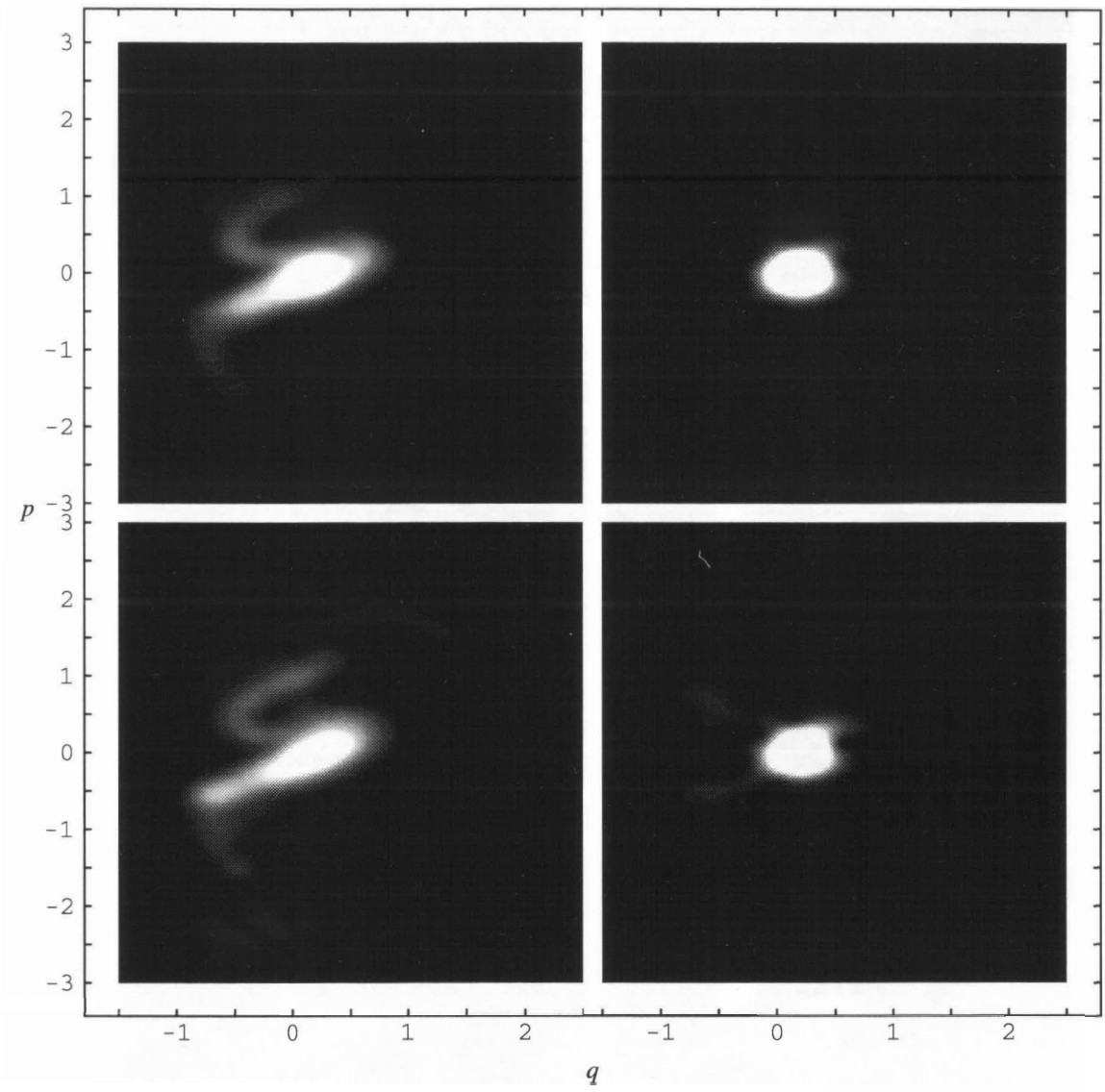

Figure 4.4: Final smoothed Liouville density (left column) and Husimi density (right column) for displaced motion reversal calculations for the DQO with the chaotic standard parameters. These calculations used $t_{\mathrm{mr}} = 13T$, and on this page the displacements $\delta q = 0.0025$ (top) and $\delta q = 0.005$ (bottom) were used.

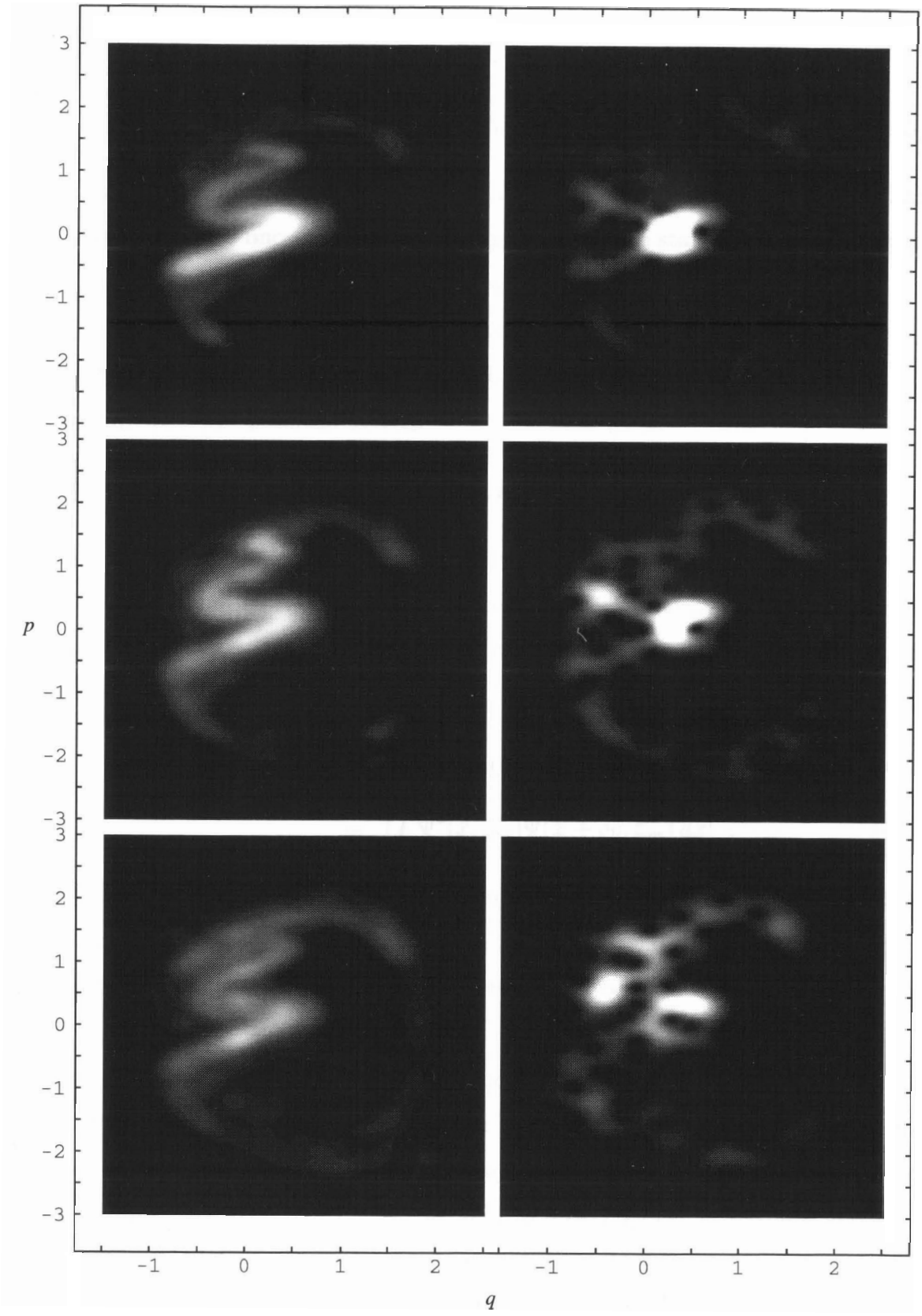

Figure 4.4: (cont.) ρ_{SL} (left) and ρ_{H} (right) for $\delta q = 0.01$, 0.02, and 0.04, top to bottom.

instead write

$$S_{\rm cl}(\delta q, t_{\rm mr}) = 2\pi\hbar \int\!\!\int \rho_{\rm L}(q,p,t_{\rm mr})\rho_{\rm L}(q+\delta q,p,t_{\rm mr})\,dq\,dp. \tag{4.3}$$

This form for $S_{\rm cl}$ is much easier to calculate than expression (4.2), since here the state need only be evolved once to $t = t_{\rm mr}$, whereas for (4.2) the state must be evolved to $t = 2t_{\rm mr}$ for each value of the perturbation δq.

In the quantum case, the mathematical properties of the Wigner density presented in section 3.2.1, which parallel those of the Liouville density, suggest comparing the classical $S_{\rm cl}$ with the quantum overlap

$$S_{\rm qm}(\delta q, t_{\rm mr}) = 2\pi\hbar \int\!\!\int \rho_{\rm W}(q,p,0)\rho'_{\rm W}(q,p,2t_{\rm mr})\,dq\,dp. \tag{4.4}$$

Here $\rho_{\rm W}(q,p,0)$ is the initial Wigner density, and $\rho'_{\rm W}(q,p,2t_{\rm mr})$ is the density at $t = 2t_{\rm mr}$, after a motion reversal and displacement δq at $t = t_{\rm mr}$, and a final motion reversal at $t = 2t_{\rm mr}$. Using relation (3.41) of section 3.2.1, we can rewrite $S_{\rm qm}$ in terms of an overlap between state functions, namely in coordinate representation

$$S_{\rm qm}(\delta q, t_{\rm mr}) = \left| \int \Psi^*(x,0)\Psi'(x,2t_{\rm mr})\,dx \right|^2 \tag{4.5}$$

$$= \left| \int \Psi^*(x,t_{\rm mr})\Psi(x+\delta q,t_{\rm mr})\,dx \right|^2. \tag{4.6}$$

Here $\Psi(x,0)$ is the initial state function, and $\Psi'(x,2t_{\rm mr})$ is the state at $t = 2t_{\rm mr}$, after a motion reversal and displacement δq at $t = t_{\rm mr}$, and a final motion reversal at $t = 2t_{\rm mr}$. The constancy of quantum overlaps has been used to again obtain an easier expression to calculate.

Figure 4.5 presents plots of $S_{\rm cl}(\delta q, t_{\rm mr})$ and $S_{\rm qm}(\delta q, t_{\rm mr})$ for motion reversal times $t_{\rm mr} = 1T$, $7T$, and $13T$. A quantum curve for $t_{\rm mr} = 40T$ is also included. The chaotic standard parameters were used, and the overlaps were calculated using equations (4.3) and (4.6). As expected, the curves approach overlap values of unity and near zero for small and large δq, respectively. The classical and quantum curves agree very well when the state is evolved for the shortest time, with $t_{\rm mr} = 1T$. This is consistent with figure 4.2, where the classical and quantum plots exhibit the same

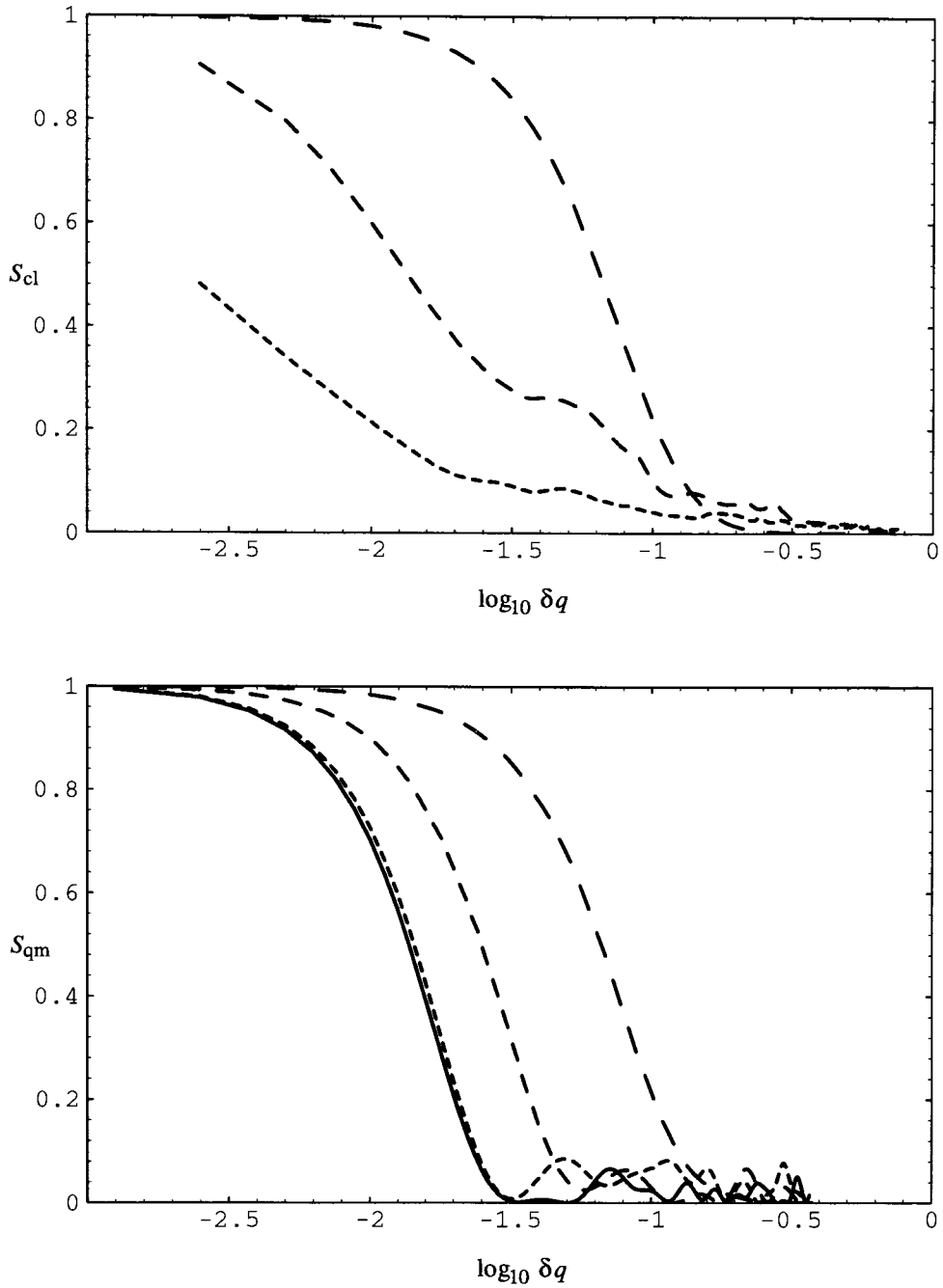

Figure 4.5: Classical overlap $S_{\rm cl}(\delta q, t_{\rm mr})$ (top) and quantum overlap $S_{\rm qm}(\delta q, t_{\rm mr})$ (bottom) plotted against $\log_{10}(\delta q)$. The chaotic standard parameters of the DQO were used. In order of decreasing dash size, the plots are for $t_{\rm mr} = 1T$, $7T$, and $13T$. The quantum result for $t_{\rm mr} = 40T$ (solid line) is also shown.

dependence on δq. As $t_{\rm mr}$ increases, $S_{\rm cl}$ becomes sensitive to smaller and smaller δq, which indicates that the classical state returns less and less accurately to the initial state after the displaced motion reversal. However, the behaviour of the quantum overlap, $S_{\rm qm}$, saturates by $t \simeq 13T$, so that the quantum state returns accurately to the initial state for $\delta q \lesssim 0.005$ no matter how large the motion reversal time $t_{\rm mr}$.

The information contained in the $S_{\rm cl}(\delta q, t_{\rm mr})$ and $S_{\rm qm}(\delta q, t_{\rm mr})$ curves can be usefully reduced in the following way. Define a quantity $\delta q_{50}(t_{\rm mr})$ such that $S_{\rm cl}(\delta q_{50}, t_{\rm mr}) = 1/2$ in the classical case or $S_{\rm qm}(\delta q_{50}, t_{\rm mr}) = 1/2$ in the quantum case. The value $\delta q = \delta q_{50}(t_{\rm mr})$ is the size of the displacement needed for a state to return after a displaced motion reversal and make an overlap of $1/2$ with the initial state. Thus $\delta q_{50}(t_{\rm mr})$ gives a (somewhat arbitrary) indication of the smallest displacement that the state will be sensitive to. Because the curves of figure 4.5 were found to be typical, this definition of δq_{50} is reasonable and will not lead to multiple-valued ambiguities.

Figure 4.6 presents $\delta q_{50}(t_{\rm mr})$ in the chaotic case. The bottom two curves show the classical and quantum values using the chaotic standard parameters (initial states with $\Delta q = \Delta p = 0.1$, and $\hbar = 0.02$ in the quantum case). To illustrate the effect of varying the value of $\hbar$, the top three curves show quantum results for initial Gaussian states centred at $(\langle q \rangle, \langle p \rangle) = (0.2, 0)$ in the chaotic zone and using the values $\hbar = 0.04$, 0.08, and 0.16 and initial widths $\Delta q = \Delta p = 0.1 \cdot 2^{1/2}$, 0.2, $0.2 \cdot 2^{1/2}$, respectively. In the classical case, $\delta q_{50}(t_{\rm mr})$ decreases (with fluctuations) until $\delta q_{50} \simeq 0.003$, the smallest value that could be determined in reasonable computing time. For the quantum curve with $\hbar = 0.02$, $\delta q_{50}(t_{\rm mr})$ approximates the classical curve for small $t_{\rm mr}$, but saturates at a value $\delta q_{50} \simeq 0.0130$ for large $t_{\rm mr}$. As $\hbar$ increases, the quantum curves saturate at larger and larger values of δq_{50}, respectively $\delta q_{50} \simeq 0.0280$, 0.0569, and 0.104 for $\hbar = 0.04$, 0.08, and 0.16. (These saturated values were calculated by taking the average of $\delta q_{50}(t_{\rm mr})$ for $t_{\rm mr} \geq 15T$.)

Figure 4.7 shows the classical and quantum values of $\delta q_{50}(t_{\rm mr})$ for the non-chaotic standard values (recall that these values differ from the chaotic parameters only in the location of the initial state). Here the classical $\delta q_{50}(t_{\rm mr})$ decreases on average

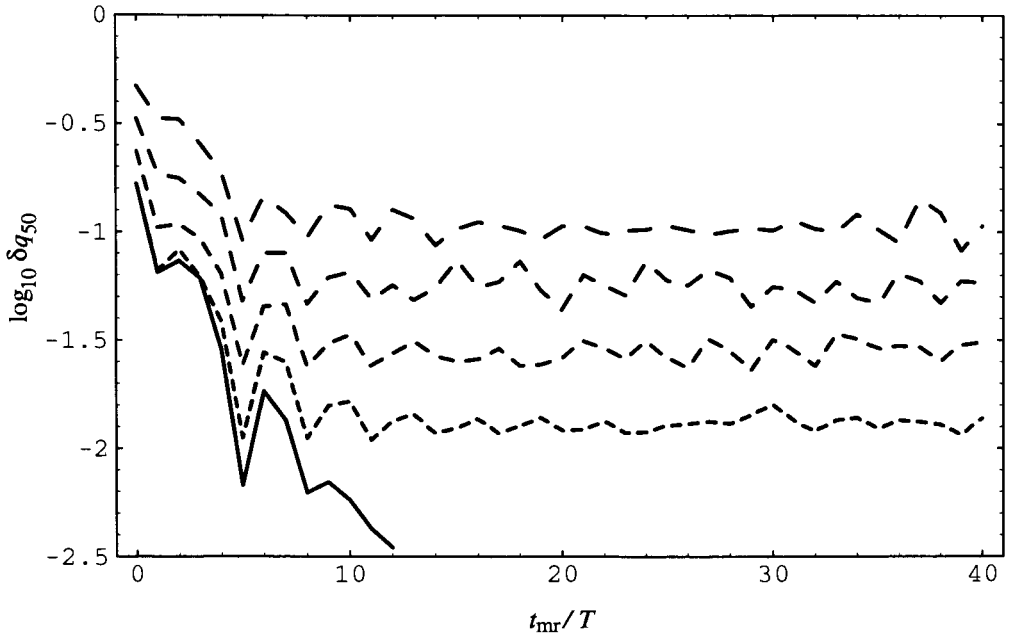

Figure 4.6: Plots of $\log_{10} \delta q_{50}(t_{mr})$ versus t_{mr} for the classical (solid line) and quantum (dashed lines) cases. The classical calculations used the standard chaotic parameters. In order of decreasing dash size, the quantum curves used $\hbar = 0.16$, 0.08, 0.04, and 0.02, and all states were launched at the same location in the chaotic zone.

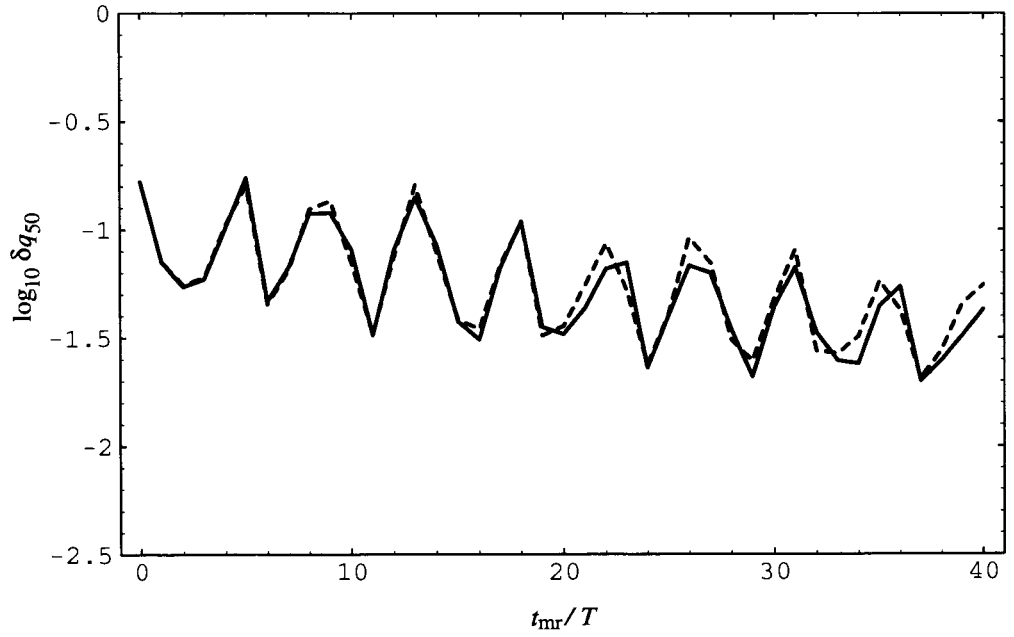

Figure 4.7: Same as figure 4.6, but showing the classical (solid line) and quantum (dashed line) results using the non-chaotic standard parameters.

much more slowly than in the chaotic case, and the quantum values agree quite well with the classical ones for all $t_{\rm mr}$ considered.

The results presented in figure 4.6 indicate that whereas the classical state is sensitive to smaller and smaller displacements as $t_{\rm mr}$ increases, the quantum states' sensitivities saturate at values of δq_{50} which increase as $\hbar$ increases. This was anticipated above on the basis of a simple de Broglie wavelength argument. For a more careful argument, note that we can write the quantum overlap of equation (4.6) as

$$S_{\rm qm}(\delta q, t_{\rm mr}) = \left|\langle\Psi(t_{\rm mr})|e^{-iP\delta q/\hbar}|\Psi(t_{\rm mr})\rangle\right|^2 \tag{4.7}$$

$$= \left|\int |\Psi(p, t_{\rm mr})|^2 e^{-ip\delta q/\hbar}\, dp\right|^2 . \tag{4.8}$$

In words, $S_{\rm qm}(\delta q, t_{\rm mr})$ is just the squared modulus of the Fourier transform of the momentum probability density. Thus there must exist an uncertainty-type relation between the width of $S_{\rm qm}$, which will be of order $\delta q_{50}(t_{\rm mr})$, and the width of $|\Psi(p, t_{\rm mr})|^4$, which will be of order $\Delta p(t_{\rm mr})$, the momentum standard deviation of the state at $t = t_{\rm mr}$ (which was calculated in section 3.3). We can therefore estimate

$$\delta q_{50}(t_{\rm mr}) \simeq \frac{\hbar}{2\Delta p(t_{\rm mr})}. \tag{4.9}$$

Note that this relation applies at each moment as the state evolves. In particular, from figure 3.8 we can estimate $\Delta p \simeq 1.25$ for $t \geq 15T$. This is the saturation period for δq_{50}, and is also the period when the state fills the chaotic zone more or less uniformly. This value of Δp is essentially independent of $\hbar$ for the values of $\hbar$ examined. For $\hbar = 0.02$, 0.04, 0.08, and 0.16, equation (4.9) thus gives $\delta q_{50} \simeq 0.008$, 0.016, 0.032, and 0.064, respectively, in reasonable agreement with the saturated values found above, considering the order of magnitude nature of estimate (4.9). Most significantly, the mean spacing between the saturated values of $\log_{10} \delta q_{50}$ is approximately 0.302, compared with the value of $\log_{10}(2) \simeq 0.301$ expected from equation (4.9) for values of $\hbar$ differing by factors of two. In other words, the saturated δq_{50} values are found to be very nearly proportional to $\hbar$, as expected.

Summary

Although quantum evolution is not sensitive to perturbations of the form $|\Psi\rangle \rightarrow |\Psi\rangle + |\delta\Psi\rangle$, this of course does not contradict sensitivity in classical chaos because perturbations in the state function are not physically equivalent to perturbations in a position or momentum coordinate. Indeed, for a state in the classical regime, a displacement δq can be "small", in the sense that δq is much less than system scales, while the corresponding overlap $S_{\rm qm}(\delta q)$ (or $S_{\rm cl}(\delta q)$) is near zero, so that the state does not return well to its initial state after a displaced motion reversal. This is how the quantum stability to perturbations in the state vector is circumvented in a displaced motion reversal.

Figures 4.2 to 4.6 demonstrate that both classical and quantum states exhibit essentially the *same* dependence on displacements δq, for displacements larger than the saturation value given by equation (4.9). As illustrated in figure 4.6, this value becomes smaller in proportion to $\hbar$ as the classical regime is approached, holding $\Delta p(t_{\rm mr})$ constant. Thus, for classically chaotic systems, typical quantum states in the classical regime are expected to display essentially the same sensitivity to perturbations and effective irreversibility as the Liouville density does.

4.2 Measures of Chaos

The results presented so far indicate a distinct difference in the quantal behaviour of classically chaotic and non-chaotic systems. It would be useful to quantitatively characterize this quantal behaviour in a way that generalizes the classical Lyapunov exponent. One apparent method to try to do this is simply to replace the classical trajectory (q, p) in the definition of the Lyapunov exponent with the quantal expectations $(\langle q\rangle, \langle p\rangle)$. This approach has been taken by Haake *et al.* [46]. Clearly, given a classical Hamiltonian with largest Lyapunov exponent λ and given any final time $t_{\rm f}$, it is always possible to choose a scaled $\hbar$ such that an initial Gaussian wavepacket, evolving under the corresponding quantized Hamiltonian, will remain

localized within the Ehrenfest regime (to any required accuracy) until $t_{\rm f}$. Thus a classical trajectory can be approximated by quantal expectations to any required accuracy until any particular final time $t_{\rm f}$, and so it must be possible *in principle* to obtain λ as accurately as one wishes using only quantum mechanics. However, the results of the previous chapter indicate that for realistic initial conditions and values of the Lyapunov exponent, a quantum state remains in the Ehrenfest regime for only very short times (this is due to the logarithmic dependence on $\hbar$ that $t_{\rm Ehr}$ exhibits; recall equation (3.69)). Thus instead, this section will present a number of alternative approaches, each of which relates properties of classical *distributions* to those of quantum states.

4.2.1 Contour Lengths

Consider a classical Liouville density $\rho_{\rm L}(q,p,t)$ evolving in, for simplicity, a two-dimensional phase space. Consider the contour $\Sigma(t)$ defined by the relation $\rho_{\rm L}(q,p,t) = C$, for some constant C. For a bounded system, $\Sigma(t)$ will consist of one or more closed curves in the phase space. Because the distance between each pair (aside from a set of measure zero) of infinitesimally separated points on $\Sigma(t)$ will grow as $e^{\lambda t}$ for long enough time t, the length $L_\Sigma(t)$ of the contour must itself grow like $e^{\lambda t}$ for long times. Thus we expect

$$\lambda = \lim_{t\to\infty} \frac{1}{t} \ln\left[\frac{L_\Sigma(t)}{L_\Sigma(0)}\right], \tag{4.10}$$

and there is no need to restrict the entire contour to lie within the regime of validity of the linearized dynamics. Given the result of section 3.4.3 that the Husimi density evolves essentially according to the Liouville equation in the classical regime, it would appear reasonable to adopt equation (4.10) as a *definition* of a quantal Lyapunov exponent, with the contour now defined by $\rho_{\rm H}(q,p,t) = C$. For fixed scaled $\hbar$, such a quantal contour cannot grow in length indefinitely due to the smoothing inherent in $\rho_{\rm H}$. Thus, rather than take the limit of infinite time as in (4.10), it will be necessary to restrict such a calculation to finite times and define the *finite-time* Lyapunov

exponent for the contour by

$$\lambda(t) = \frac{1}{t} \ln \left[\frac{L_\Sigma(t)}{L_\Sigma(0)} \right]. \tag{4.11}$$

A finite-time exponent will in general depend on the initial position and shape of the contour. Essentially this approach was adopted by Toda and Ikeda [47].

Classical results

To examine the feasibility of a quantal calculation of this sort, a classical contour length calculation was first carried out for the DQO. In the classical case, because of the incompressible nature of the Liouville flow, it is sufficient to propagate a large number of trajectories originating on the required initial contour, rather than to evolve an entire distribution. The length of the contour at some time can be approximated by summing the distances between consecutive trajectories at the required time.

Figure 4.8 presents two logarithmic plots of contour length versus time for the classical DQO, with one contour confined within the chaotic and the other within the regular zone. In both cases the trajectories began as uniform distributions of 100000 points lying on circles of radius 0.15 (of course a circle in phase space can only be spoken of once units have been fixed). The circles' centres were at $(q, p) = (0.2, 0)$ and $(1, 1)$ for the chaotic and non-chaotic case, respectively.

The logarithm of the contour length in the chaotic case exhibits a quite well defined linear increase with time for $t \leq 20T$. At later times the curve levels off as the number of trajectories becomes insufficient to define the ever increasing intricacy of the contour. A least-squares fit to the curve in the linear region $t \leq 20T$ gives a finite-time Lyapunov exponent of $\lambda(20T) \simeq 0.064$, clearly different from the long-time value of $\lambda \simeq 0.042$ found in section 3.1.3 using the renormalization method. The initial growth rate for this chaotic contour was typical of several contours launched in the chaotic zone.

To understand the source of the discrepancy between the exponents calculated by

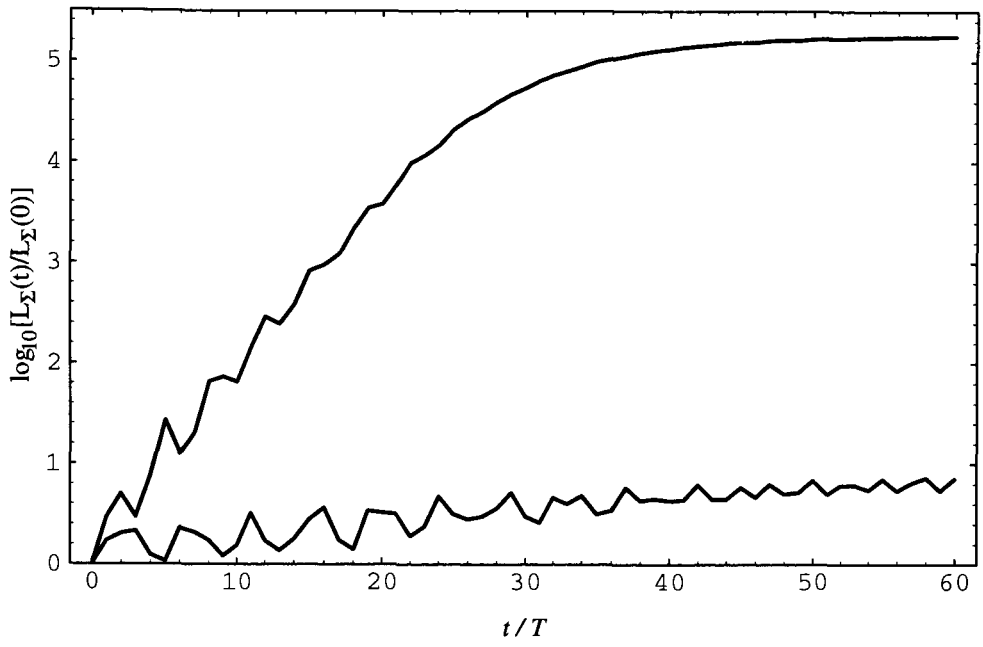

Figure 4.8: Classical contour length $L_\Sigma(t)$ on a logarithmic scale for contours confined to the chaotic (top curve) and non-chaotic (bottom curve) regions of the DQO.

the contour and renormalization methods, 10000 Lyapunov exponents were calculated using the renormalization method software, but with only a single time step ($l = 1$) of length $\tau = 20T$ for each. The initial coordinates were uniformly distributed on the same circle as was used for the chaotic contour calculations. The initial displacements were all $d(0) = 1 \times 10^{-7}$ and were oriented along the circle. Figure 4.9 plots the normalized probability density $P(\lambda)$ for finding the particular (finite-time) Lyapunov exponent λ within this set of 10000 calculations. Clearly the distribution of finite-time exponents is dominated by values larger than the long-time value of $\lambda = 0.042$. Indeed for this distribution the "exponential average" of the finite-time Lyapunov exponents, which is relevant to a contour length calculation, takes the value

$$\frac{1}{t} \ln \left[\frac{\sum_{i=1}^{N} e^{\lambda_i t}}{N} \right] \simeq 0.066, \tag{4.12}$$

very close to the contour length value. Here the λ_i are the $N = 10000$ finite-time exponents and the value $t = 20T$ was used.

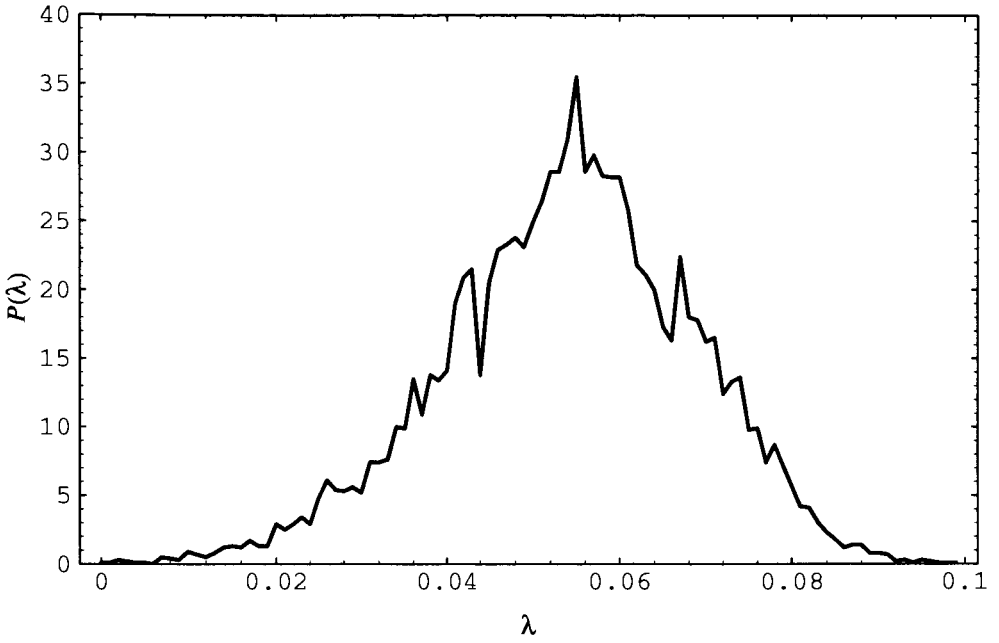

Figure 4.9: Normalized probability density $P(\lambda)$ versus finite-time Lyapunov exponent λ for the set of 10000 chaotic initial conditions described in the text. These calculations used $l = 1$ time step of length $\tau = 20T$. The long-time value is $\lambda \simeq 0.042$.

Quantum results

A straightforward algorithm was developed to determine and approximate the lengths of contours in the Husimi density. Figure 4.10 presents logarithmic plots of contour length versus time for initial Gaussian states in the quantum DQO using the chaotic and non-chaotic standard parameter values. The chaotic case classical contour length is also plotted for reference. Both quantum curves are for the contour value $\rho_{\mathrm{H}}(q, p, t) = 0.025$. Whereas in the classical case the arguments leading to equation (4.10) are independent of which contour is chosen, the behaviour of Husimi contours will in general depend on the contour value (the maximum value of ρ_{H}, *e.g.*, need not be constant). Nevertheless, the results of figure 4.10 were found to be typical for contour values small relative to the maximum of ρ_{H} (which was of order unity here). While the Husimi contour in the classically chaotic case does grow initially much more rapidly than in the classically non-chaotic case, the contour length quickly levels off and a well defined exponential growth period does not exist.

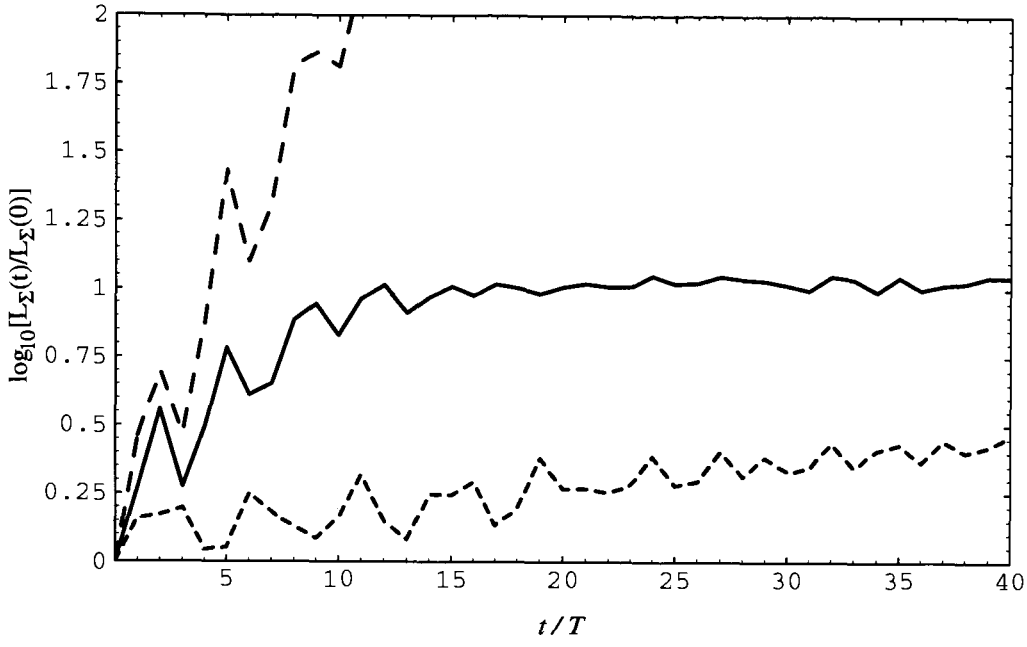

Figure 4.10: Husimi contour length $L_\Sigma(t)$ on a logarithmic scale for the chaotic (solid curve) and non-chaotic (finely dashed curve) standard parameters of the DQO and contour value $\rho_H = 0.025$. The chaotic classical contour length is also shown (coarsely dashed curve).

4.2.2 Distribution Widths

Consider again a classical Liouville density contour $\Sigma(t)$. In the chaotic case, this contour will rapidly stretch into a long thin thread whose length will grow as $e^{\lambda t}$ for large enough t. If the entire contour is confined to within the region of validity of the linearized dynamics, then for any Liouville distribution confined within $\Sigma(t)$ no folding can occur and the standard deviations $\Delta q(t)$ and $\Delta p(t)$ must also grow as $e^{\lambda t}$ for long times. Thus by observing the rate of growth of the distribution widths, one could estimate λ. The growth of *quantum mechanical* distribution widths could similarly be used to calculate a quantal Lyapunov exponent. This approach has been used by Frahm and Mikeska [48] in the study of a spin system.

Calculations of this sort have already been carried out for the DQO in section 3.3. Figures 3.8 and 3.9 illustrate the growth of the classical and quantal Δq and Δp for the chaotic and non-chaotic standard parameters. Although the initial growth

rates in the chaotic case far exceed those in the non-chaotic case, there certainly are no exponential growth stages visible. This is due to the rapid growth which quickly invalidates the linearized (or Ehrenfest) dynamics, and the consequent folding visible in the phase space distributions. This method would appear to be severely restricted by the simultaneous requirements of linearity and large times needed to obtain an approximation to λ, as was the method of expectation values discussed above.

4.2.3 Size of Finest Details

Picture again the classical contour $\Sigma(t)$ in the chaotic case evolving into essentially a long thin thread whose length grows exponentially with time. Because phase space volumes are conserved classically, we expect that a characteristic measure of the width of the thread will *decrease* as $e^{-\lambda t}$ for large enough t. Thus we also expect that for an evolving Liouville density, some characteristic measure of the size of the finest details present in the state will decrease as $e^{-\lambda t}$. The quantity $\delta q_{50}(t)$, defined in section 4.1.3 as the displacement needed to make the overlap between the states $\rho_{\mathrm{L}}(q,p,t)$ and $\rho_{\mathrm{L}}(q+\delta q_{50},p,t)$ equal to $1/2$, provides such a characteristic measure. As described in section 4.1.3, a quantal analog can readily be constructed.

Figures 4.6 and 4.7 of section 4.1.3 present the evolution of the classical and quantal $\delta q_{50}(t)$. Again there is a distinct difference in behaviour between the chaotic and non-chaotic cases. However, the chaotic case classical curve of figure 4.6 could not be calculated to long enough times to accurately define a slope in the logarithmic plot, from which a Lyapunov exponent might be estimated. The quantum curves, as discussed previously, saturate at values of δq_{50} proportional to $\hbar$ (and given approximately by equation (4.9)). Thus, for this method to provide a useful characterization of the quantal dynamics, it is expected that the saturation level given by equation (4.9) would need to be at least a couple of orders of magnitude smaller than the initial value $\delta q_{50}(t=0)$.

4.2.4 Coarse-grained Entropy

The entropy of a classical Liouville distribution $\rho_{\rm L}(q,p,t)$ is defined by

$$S_{\rm L} = -k \iint \rho_{\rm L}(q,p,t) \ln[A\rho_{\rm L}(q,p,t)]\, dq\, dp, \tag{4.13}$$

where k is Boltzmann's constant and A is an arbitrary constant which makes the argument of the logarithm dimensionless and sets the zero of entropy. This Liouville entropy is constant in time (for an isolated system), and so is not useful in characterizing dynamics. However, a coarse-grained entropy will exhibit non-trivial behaviour. Consider, for example, a rectangular grid partition of phase space into cells labeled by the index i. Let

$$p_i(t) = \iint\limits_{i\text{'th cell}} \rho_{\rm L}(q,p,t)\, dq\, dp \tag{4.14}$$

and define the coarse-grained entropy by

$$S_{\rm c}(t) = -k \sum_i p_i(t) \ln p_i(t). \tag{4.15}$$

Then, if an initial Liouville density is confined to one cell, we have $S_{\rm c}(0) = 0$. If the system is chaotic, we expect that at sufficiently long times the density will form a thin thread of exponentially growing length, as described above. During the time interval that the thread width is narrower than the cell width and yet the thread passes through any cell no more than once, we can estimate the coarse-grained entropy by $S_{\rm c}(t) = k \ln N(t)$, where $N(t)$ is the number of cells the thread passes through. Since $N(t)$ is expected to increase as $e^{\lambda t}$ for large enough t, we expect $S_{\rm c}(t)/k$ to increase linearly in time with slope λ. Eventually, when all cells that cover the accessible chaotic zone are occupied, the coarse-grained entropy will saturate. For a fine enough grid, these arguments are not expected to depend significantly on the shape of the cells, nor on whether, instead of a partition into cells, a *smoothed* Liouville density $\rho_{\rm SL}(q,p,t)$ is used to define the coarse-grained entropy through

$$S_{\rm c}(t) = -k \iint \rho_{\rm SL}(q,p,t) \ln[A\rho_{\rm SL}(q,p,t)]\, dq\, dp. \tag{4.16}$$

Note that this notion of a coarse-grained entropy is not to be confused with the Kolmogorov-Sinai (KS) entropy (also known as the metric entropy). The calculation of the KS entropy involves propagating a phase space partition itself, and determining the rate at which subsequent intersections of the evolving partition with the initial partition proliferate with time [1]. It can be shown that the KS entropy for Hamiltonian systems is just the sum of the positive Lyapunov exponents [1], and this is how the KS entropy is normally determined.

In quantum mechanics the von Neumann entropy is defined as

$$S_{\mathrm{vN}} = -k\mathrm{Tr}\,(\hat{\rho}\ln\hat{\rho}), \tag{4.17}$$

for a system described by density matrix $\hat{\rho}$. In the case of a pure state, as the DQO calculations have involved, we have $S_{\mathrm{vN}} = 0$ for all time, a situation that parallels the constancy of the classical Liouville entropy. Recalling the close similarity in behaviour between the smoothed Liouville and Husimi densities found in chapter 3, it would appear reasonable to define a quantal coarse-grained or Husimi entropy in analogy with expression (4.16) by

$$S_{\mathrm{H}}(t) = -k\iint \rho_{\mathrm{H}}(q,p,t)\ln[A\rho_{\mathrm{H}}(q,p,t)]\,dq\,dp, \tag{4.18}$$

and to define a quantal Lyapunov exponent by the growth rate of S_{H}/k. Takahashi [10] studied the behaviour of the Husimi entropy S_{H} for a double-well potential system, but did not attempt to relate the growth rate of S_{H} to a quantal Lyapunov exponent.

Figure 4.11 presents plots of the Husimi entropy $S_{\mathrm{H}}(t)$ calculated using equation (4.18) and using both the chaotic and non-chaotic standard parameters for the DQO (base 10 rather than natural logarithms were used here to allow comparison with the previous figures). The arbitrary constant was given the value $A = 2\pi\hbar e$ so that $S_{\mathrm{H}}(0) = 0$ for the initial Gaussian states. The chaotic case classical contour length of section 4.2.1 is included in figure 4.11 for comparison. The results are now familiar: whereas $S_{\mathrm{H}}(t)$ grows initially much more rapidly in the chaotic than in the non-chaotic case, no well-defined region of linear increase in $S_{\mathrm{H}}(t)$ exists.

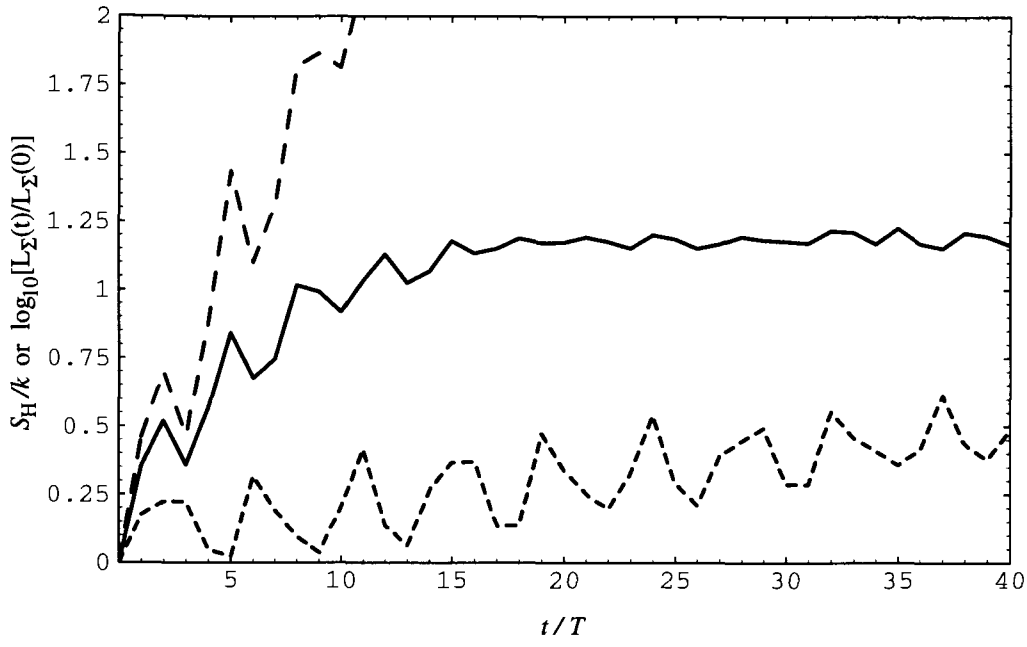

Figure 4.11: Husimi entropy $S_H(t)/k$ for the chaotic (solid curve) and non-chaotic (finely dashed curve) standard parameters of the DQO. The chaotic classical contour length is also shown (coarsely dashed curve).

4.2.5 Summary

None of the methods to characterize quantal dynamics examined here provided sufficiently well defined quantal analogs of the Lyapunov exponent. This is due to the value of $\hbar = 0.02$ used in the standard parameter calculations not being "classical enough", so that the initial Gaussian state reaches an effective steady state too quickly. This point is exemplified by figure 4.6, which illustrates the approach of the behaviour of the quantal $\delta q_{50}(t)$ to that of the classical version as $\hbar$ is decreased. Were it possible to perform calculations at much smaller $\hbar$, it is expected that the chaotic case quantal curves of figures 4.10 and 4.11 would approach the classical contour length curve, and hence provide similar *finite-time* dynamical information.

Each technique considered here did distinguish sharply between quantal evolution in the classically chaotic and non-chaotic cases, and this is probably the most useful aspect of these methods for systems as "non-classical" as the DQO. The methods of sections 4.2.2 and 4.2.3, namely studying the growth or decay rates of $\Delta q(t)$ and $\Delta p(t)$

and $\delta q_{50}(t)$, are in fact closely related through relation (4.9), and are thus expected to share the disadvantage, discussed at the end of section 4.2.2, of being sensitive to the nonlinear regime. The contour length and entropy methods of sections 4.2.1 and 4.2.4 are not expected to be as sensitive to the non-linear regime. Despite the apparent arbitrariness in choosing a Husimi contour value, the quantum curves of figures 4.10 and 4.11 exhibit remarkable similarity, an indication of the consistency of the arguments of sections 4.2.1 and 4.2.4.

Chapter 5

Conclusions

An attempt has been made throughout this thesis to employ the correspondence principle in the following way. While many classical quantities and properties appear strictly to have no quantal analog, we do expect to be able to construct *some* quantities or consider *some* properties in quantum mechanics which nevertheless *do* approach the required classical behaviour in the classical regime. Studying these quantum mechanical quantities and properties should help reveal how classicality emerges and can also provide useful ways of characterizing purely quantal dynamics. The DQO model has demonstrated the usefulness of this approach in the construction of quantal phase space distributions, in the study of displaced motion reversals, and in the examination of (finite-time) quantal measures of chaos.

In chapter 3 the evolution of phase space densities and distribution means and widths was studied, for initially well-localized quantal and classical states in both chaotic and regular zones of the DQO. For short times in the chaotic case, and for all examined times in the non-chaotic case, Ehrenfest's theorem was found to be valid and very good agreement was observed between classical and quantal distributions (and hence their lower moments). This result was explained by the mathematical notion of *practically classical* behaviour: the Wigner density evolves essentially according to the Liouville equation when the state is localized within the linear (or Ehrenfest) regime. In the chaotic case the states remain so localized for a much

briefer time than in the regular case.

In the chaotic case after Ehrenfest's theorem becomes invalid, classical and quantal smoothed phase space densities and lower distribution moments agree reasonably well, with the degree of agreement improving as the scaled $\hbar$ decreases. This aspect of the results was explained by showing that the Husimi density evolves essentially according to the Liouville equation in the classical regime, where typical system actions are much greater than $\hbar$.

The *practical* importance of these two limiting cases of quantal evolution must be stressed. The conditions of validity for these two cases, carefully stated in sections 3.4.2 and 3.4.3, tell us when we can substitute quantal calculations with less time-consuming classical ones.

In chapter 4 the DQO also proved useful in examining quantal analogs for various means of characterizing classical chaos. It was shown, using the idea of a displaced motion reversal, how quantum states in the classical regime can exhibit essentially the same sensitivity to perturbations and effective irreversibility that classical systems can, despite the well-known quantal stability to perturbations in the state vector. In addition, a number of techniques for quantitatively characterizing quantal dynamics in a way that generalizes the classical Lyapunov exponent were presented. Although such quantal exponents could not be sufficiently well defined for the DQO, it was possible to distinguish sharply between the quantal dynamics in the classically chaotic and non-chaotic cases. The method of examining the growth of the Husimi entropy was perhaps most free of arbitrariness and sensitivity to the nonlinear regime.

One issue raised in the Introduction has yet to be addressed: that of the algorithmic incompressibility of classical trajectories versus the compressibility of quantum mechanics which Ford *et al.* [20, 19] have described. Recall from the Introduction that an apparent paradox arises when one notes that, as Ford *et al.* have shown, the number of initial state significant digits required to to calculate a final state to some particular accuracy grows linearly with propagation time classically, but

only logarithmically quantum mechanically, for classically chaotic systems. Hence it might appear that one could exploit the correspondence principle and circumvent the difficulty of performing accurate classical calculations in chaotic systems by doing numerically easier quantum mechanical calculations sufficiently deep into the classical regime. Recalling the discussion of motion reversal in section 4.1, the resolution should now be readily apparent: calculating a *wave function* (or any quantity derived from it) to some number of significant digits is *by no means* physically equivalent to calculating a classical *trajectory* to the same number of digits.

It is worth illustrating how a quantum mechanical calculation will indeed be just as "difficult" as a classical one if we demand from both theories the *same* physical information. Consider first the classical case, and for convenience, choose units so that accessible position and momentum coordinates are of order unity. Specifying a trajectory (at some time) to n significant digits is then equivalent to describing the system by a Liouville density whose width is of order $10^{-(n+1)}$. Now, as explained in section 4.2.2, the width of this density grows exponentially with time for a chaotic system, for long enough times and if the Liouville density lies within the linear regime. Therefore, the width of such a density at the initial time $t = 0$ must be decreased exponentially with propagation time t_f if the final width (at $t = t_f$) is to have some particular fixed value. Because of the above connection between distribution widths and trajectory accuracy, Ford's statement of incompressibility in classical mechanics follows immediately; namely, that the number of digits needed to specify an initial trajectory must grow linearly with t_f, for fixed final accuracy.

In the quantal case, rather than ask how fast accuracy diminishes in a wave function calculation, let us ask the *same* question as was asked classically. That is, how small must the width of an initial wave packet be (in other words, how well must the initial position and momentum of the particle be known) in order that the final packet have some particular width? Because the packets are restricted to the linear regime, the quantal evolution will be practically classical (as defined in section 3.4.2). Thus the classical argument of the previous paragraph applies here, implying

that the quantal evolution is as incompressible as the classical evolution. We must only keep in mind that t_f must not be so large, or the final width so small, that the initial widths cannot obey the uncertainty principle. These concerns of course become irrelevant as $\hbar \to 0$.

Note in addition that we can estimate the largest value of t_f consistent with the uncertainty principle by an argument parallel to that leading to expression (3.69) for the Ehrenfest time. We must only replace t_{Ehr} with t_f, and L_V with the width of the final state here. This gives us the upper limit $t_f \sim -(\ln \hbar)/\lambda$. We can, in a purely formal sense, imagine reducing our scaled $\hbar$ to make t_f as large as we like. To do this, we would thus require $\hbar \sim \exp(-\lambda t_f)$. This point is akin to that made at the beginning of section 4.2, namely that the formal, mathematical structure of quantum mechanics is capable of providing the classical Lyapunov exponent to any required accuracy.

It is worth making a few last general remarks on the results discussed in this thesis. For classically chaotic systems, Ehrenfest's theorem was shown to be valid for only very short times (on the order of the inverse Lyapunov exponent), which severely restricts the usefulness (in the context of the first paragraph of this chapter) of attempting to construct a quantal analog of a classical trajectory. Nevertheless, we can still use classical distribution mechanics to accurately describe quantal evolution in the classical regime. That a quantum state evolves essentially as a classical Liouville distribution in the classical (or indeed linear) regime is a purely mathematical result and is independent of what physical interpretation one might attach to the state vector. Such a mathematical result can perhaps *suggest*, but cannot *imply*, a particular physical interpretation. We can only say with certainty that, even for pure states, sufficiently coarse-grained quantal probabilities behave essentially like classical distributions in the classical regime. That a classically chaotic quantum state can rapidly fill a macroscopic chaotic zone does, however, urge us to consider the physical meaning of such a state.

As a final note, recall from the Introduction the importance to classical mechanics of the revelation that chaos can be present in few-degree-of-freedom systems. This chaos is characterized by a rapid loss of "predictability" for trajectories, or equivalently by a rapid spreading of distributions. The main quantal consequence of this classical result would appear to be that the single-trajectory Ehrenfest view cannot be relied upon, and distributions become an essential component of the description of the classical world.

Appendix A

The Driven Harmonic Oscillator

Our goal is to determine the quantal time evolution of an initial Gaussian state in a driven harmonic oscillator. The Hamiltonian for this system is

$$H = \frac{1}{2m}P^2 + \frac{1}{2}kQ^2 + a\cos(\omega' t)Q \tag{A.1}$$

where m is the mass, k the spring constant, and Q and P the position and momentum operators. The system is driven at frequency ω' and amplitude a. A solution will be sought using an operator algebra approach. Throughout this Appendix, operators and classical quantities will be indicated by upper- and lower-case symbols, respectively.

We will consider a Gaussian initial state with position standard deviation σ_x equal to the field-free harmonic oscillator ground state value of $\left[\hbar/(4km)^{1/2}\right]^{1/2}$. Thus we will look for a solution in the form of a Gaussian displaced in position and momentum from the harmonic oscillator ground state, denoted $|0\rangle$, or in coordinate representation

$$\langle x|0\rangle = \left[(2\pi)^{1/2}\sigma_x\right]^{-1/2} e^{-x^2/4\sigma_x^2}. \tag{A.2}$$

The displacement of the ground state is accomplished with the *displacement operator*, $D(q(t), p(t))$, defined by

$$D(q(t), p(t)) = e^{i[p(t)Q - q(t)P]/\hbar}, \tag{A.3}$$

where the classical variables $q(t)$ and $p(t)$ are the time-dependent displacements in position and momentum, respectively. To see this, note that the identity

$$e^{A+B} = e^A e^B e^{-[A,B]/2}, \tag{A.4}$$

which holds when the operators A and B satisfy $[A,[A,B]] = [B,[A,B]] = 0$, allows us to write

$$D(q(t),p(t)) = e^{ip(t)Q/\hbar} e^{-iq(t)P/\hbar} e^{-ip(t)q(t)/2\hbar}. \tag{A.5}$$

From this last expression we can see that $D(q,p)$ does indeed perform the required displacements, aside from the coordinate- and momentum-independent phase factor $e^{-ip(t)q(t)/2\hbar}$, so that $D(q,p)|0\rangle$ represents a Gaussian state with mean position q and mean momentum p.

Thus we will look for a solution to the Schrödinger equation

$$\frac{d}{dt}|\Psi(t)\rangle = \frac{-i}{\hbar} H|\Psi(t)\rangle \tag{A.6}$$

in the form

$$|\Psi(t)\rangle = e^{i\phi(t)} D(q(t),p(t))|0\rangle, \tag{A.7}$$

where $\phi(t)$ is a coordinate- and momentum-independent phase. The solution will be subject to the initial condition

$$|\Psi(0)\rangle = e^{i\phi_0} D(q_0,p_0)|0\rangle. \tag{A.8}$$

First, we can evaluate the lhs of the Schrödinger equation (A.6) using (A.7) and expression (A.5) for D, giving

$$\frac{d}{dt}|\Psi(t)\rangle = \frac{-i}{\hbar} e^{i\phi(t)} \left[-\hbar\dot{\phi} D - \dot{p} Q D + \dot{q} D P + \frac{1}{2}(p\dot{q} + \dot{p}q) D \right] |0\rangle. \tag{A.9}$$

Note that here I take the state $|0\rangle$ to be time-independent, and absorb the usual ground state time dependence into the phase factor $e^{i\phi(t)}$.

To put the rhs of (A.6) into a form like (A.9), we need the commutation relations

$$[P,D] = pD, \tag{A.10}$$

$$[Q,D] = qD, \tag{A.11}$$

which are straightforward to derive from (A.3). Several applications of these commutation relations give

$$\frac{-i}{\hbar}H|\Psi(t)\rangle = \frac{-i}{\hbar}\left[\frac{1}{2m}P^2 + \frac{1}{2}kQ^2 + a\cos(\omega' t)Q\right]e^{i\phi(t)}D|0\rangle \tag{A.12}$$

$$= \frac{-i}{\hbar}e^{i\phi(t)}\left\{\left[\frac{1}{2}\hbar\omega + \frac{1}{2}a\cos(\omega' t)q\right]D + \left[kq + a\cos(\omega' t)\right]QD \right.$$
$$\left. + \frac{1}{m}pDP + \frac{1}{2}\left[\frac{1}{m}pp - (kq + a\cos(\omega' t))q\right]D\right\}|0\rangle. \tag{A.13}$$

Here the relation

$$\left(\frac{1}{2m}P^2 + \frac{1}{2}kQ^2\right)|0\rangle = \frac{1}{2}\hbar\omega|0\rangle, \tag{A.14}$$

where $\omega = (k/m)^{1/2}$, has also been used.

Now, comparing (A.9) and (A.13), the Schrödinger equation can be satisfied if we set

$$\dot{q}(t) = \frac{1}{m}p(t), \tag{A.15}$$

$$\dot{p}(t) = -kq(t) - a\cos(\omega' t), \tag{A.16}$$

$$\dot{\phi}(t) = \frac{-1}{\hbar}\left[\frac{1}{2}\hbar\omega + \frac{1}{2}a\cos(\omega' t)q(t)\right]. \tag{A.17}$$

Equations (A.15) and (A.16) are just Hamilton's equations for a classical particle with position $q(t)$ and momentum $p(t)$ subject to the classical Hamiltonian corresponding to (A.1). Thus the quantum state will propagate as a Gaussian with mean position and momentum following the well-known classical trajectory for the driven harmonic oscillator,

$$q(t) = b\cos(\omega t + \theta_0) + \frac{a}{m(\omega'^2 - \omega^2)}\cos(\omega' t), \tag{A.18}$$

where the constants b and θ_0 are determined by the initial values q_0 and p_0. To simplify expressions to follow, I'll only consider initial conditions with $p_0 = 0$. This gives

$$b = q_0 - \frac{a}{m(\omega'^2 - \omega^2)}, \tag{A.19}$$

$$\theta_0 = 0. \tag{A.20}$$

The last step is determination of the phase factor by straightforward integration of (A.17) using (A.18) for $q(t)$. The result is

$$\begin{aligned}\phi(t) &= \phi_0 - \frac{\omega t}{2} - \frac{ab}{4\hbar}\left[\frac{\sin(\omega'-\omega)t}{\omega'-\omega} + \frac{\sin(\omega'+\omega)t}{\omega'+\omega}\right] \\ &\quad - \frac{a^2}{4m\hbar\omega'(\omega'^2-\omega^2)}\left[\omega' t + \frac{1}{2}\sin(2\omega' t)\right]. \end{aligned} \tag{A.21}$$

Combining equations (A.2), (A.5), and (A.7), the solution in coordinate representation can finally be written

$$\langle x|\Psi(t)\rangle = \left[(2\pi)^{1/2}\sigma_x\right]^{-1/2} e^{i\phi(t)} e^{-ip(t)q(t)/2\hbar} e^{ip(t)x/\hbar} e^{-(x-q(t))^2/4\sigma_x^2}, \tag{A.22}$$

where $\phi(t)$, $q(t)$, and $p(t)$ are given by equations (A.21), (A.18), and (A.15).

Bibliography

[1] E. Ott, *Chaos in Dynamical Systems* (Cambridge University Press, Cambridge, 1993).

[2] E. J. Heller and S. Tomsovic, Physics Today **46**, 38 (1993).

[3] M. C. Gutzwiller, *Chaos in Classical and Quantum Mechanics* (Springer-Verlag, New York, 1990).

[4] M. C. Gutzwiller, in *Les Houches Session LII: Chaos and Quantum Physics*, edited by M.-J. Giannoni, A. Voros, and J. Zinn-Justin (North-Holland, Amsterdam, 1991), p. 201.

[5] G. Casati, B. V. Chirikov, F. M. Israelev, and J. Ford, in *Stochastic Behaviour in Classical and Quantum Hamiltonian Systems, Springer Lecture Notes in Physics No. 93*, edited by G. Casati and J. Ford (Springer-Verlag, Berlin, 1979), p. 334.

[6] D. R. Grempel, R. E. Prange, and S. Fishman, Physical Review A **29**, 1639 (1984).

[7] H. J. Korsch and M. V. Berry, Physica D **3**, 627 (1981).

[8] R. V. Jensen, Nature **355**, 311 (1992).

[9] K. M. Christoffel and P. Brumer, Physical Review A **33**, 1309 (1986).

[10] K. Takahashi, Progress of Theoretical Physics Supplement No. 98, 109 (1989).

[11] N. Ben-Tal, N. Moiseyev, and H. J. Korsch, Physical Review A **46**, 1669 (1992).

[12] N. Ben-Tal *et al.*, Physical Review E **47**, 1646 (1993).

[13] J. L. Lebowitz and P. J. Reynolds, Journal of Statistical Physics **68**, 1 (1992).

[14] T. Hogg and B. A. Huberman, Physical Review A **28**, 22 (1983).

[15] R. F. Fox, Physical Review A **41**, 2969 (1990).

[16] B. L. Lan and R. F. Fox, Physical Review A **43**, 646 (1991).

[17] D. L. Shepelyansky, Physica D **8**, 208 (1983).

[18] G. Casati, B. V. Chirikov, I. Guarneri, and D. L. Shepelyansky, Physical Review Letters **56**, 2437 (1986).

[19] J. Ford and M. Ilg, Physical Review A **45**, 6165 (1992).

[20] J. Ford, G. Mantica, and G. H. Ristow, Physica D **50**, 493 (1991).

[21] *The NAG Fortran Library Manual - Mark 13*, 1988.

[22] *Modern Numerical Methods for Ordinary Differential Equations*, edited by G. Hall and J. M. Watt (Clarendon Press, Oxford, 1976).

[23] R. P. Brent, Communications of the A.C.M. **17**, 704 (1974).

[24] A. Goldberg, H. M. Schey, and J. L. Schwartz, American Journal of Physics **35**, 177 (1967).

[25] *IMSL Library Reference Manual*, 9 ed., 1982.

[26] L. F. Shampine and M. K. Gordon, *Computer Solution of Ordinary Differential Equations* (W. H. Freeman and Company, San Fransisco, 1975).

[27] J. Guckenheimer and P. Holmes, *Nonlinear Oscillations, Dynamical Systems, and Bifurcations of Vector Fields* (Springer, New York, 1983).

[28] V. I. Oseledec, Transactions of the Moscow Mathematical Society **19**, 197 (1968).

[29] J. K. Hale, *Ordinary Differential Equations* (Wiley-Interscience, New York, 1969).

[30] L. E. Ballentine, Reviews of Modern Physics **42**, 358 (1970).

[31] E. Wigner, Physical Review **40**, 749 (1932).

[32] K. İmre, E. Özizmir, M. Rosenbaum, and P. F. Zweifel, Journal of Mathematical Physics **8**, 1097 (1967).

[33] Y. Yang, Master's thesis, Simon Fraser University, 1992.

[34] K. Husimi, Proceedings of the Physico-mathematical Society of Japan **22**, 264 (1940).

[35] A. Royer, Physical Review Letters **55**, 2745 (1985).

[36] L. E. Ballentine, *Quantum Mechanics* (Prentice-Hall, Englewood Cliffs, NJ, 1990).

[37] L. E. Ballentine, Y. Yang, and J. P. Zibin, Physical Review A **50**, 2854 (1994).

[38] E. J. Heller, The Journal of Chemical Physics **65**, 1289 (1976).

[39] R. F. O'Connell, L. Wang, and H. A. Williams, Physical Review A **30**, 2187 (1984).

[40] P. C. W. Davies, *The Physics of Time Asymmetry* (Surrey University Press, London, 1974).

[41] A. Peres, Physical Review A **30**, 1610 (1984).

[42] L. Benet, T. H. Seligman, and H. A. Weidenmüller, Physical Review Letters **71**, 529 (1993).

[43] R. Schack, G. M. D'Ariano, and C. M. Caves, Physical Review E **50**, 972 (1994).

[44] R. Blümel, Physical Review Letters **73**, 428 (1994).

[45] M. B. Haeri, Physical Review E **48**, 4215 (1993).

[46] F. Haake, H. Wiedemann, and K. Życzkowski, Annalen der Physik **1**, 531 (1992).

[47] M. Toda and K. Ikeda, Physics Letters A **124**, 165 (1987).

[48] H. Frahm and H. J. Mikeska, Zeitschrift für Physik B **60**, 117 (1985).